TriboForm®
virtual tribology

Master thesis
March 2021

Prediction and validation of galling behavior in hot sheet metal forming processes

Eelkje Kooistra

Examination committee:
TriboForm Engineering:
ir. L. Bruinekreeft

University of Twente:
prof. dr. ir. A.H. van den Boogaard
dr. J. Hazrati Marangalou
prof. dr. ir. M.B. de Rooij

Mechanical Engineering:
Mechanics of Solids, Surfaces & Systems (MS3)
Nonlinear Solid Mechanics (NSM)

Document-number:
ET.21/AM-5908

UNIVERSITY OF TWENTE.

Summary

Sheet metal forming is a widely used forming process. This process is applied to hot sheet material to improve product properties, like weight and strength. However, hot sheet metal forming also comes with some disadvantages in the form of wear. Due to the high temperatures during sheet deformation no lubrication can be applied, which allows for wear to occur more severely. Here, galling is the wear mechanism of interest, which is a form of adhesive wear. Material transfers from the sheet to the tool during relative contact displacement, which is called galling. This is a problem when the material build up on the tool becomes too large that it scratches the product. The tools have to be cleaned or even replaced, which is disadvantage to the flow and cost of the production.

A model is implemented to predict galling behavior and critical locations on the tools. This model is an extension of the existing friction model within the TriboForm software. The galling model evaluates every contact spot between the tool and sheet (asperity) to check if it is suitable for galling. Two different galling initiation models for the asperities have been proposed, one based on the shape of an asperity (wedge formation initiation model - WFI) and one based on the strength of the asperity with respect to the sheet coating (coating fracture initiation model - CFI). If an asperity is initiated it will grow during the relative contact during sliding. The asperity growth is based on the growth model proposed by van der Linde. The initiation and growth of a single asperity is applied for multiple asperities on a surface. The multi asperity growth is approached with two different models, one based on the update of the separation height (van der Linde) and one based on the update of the tool topography. The model which updates the separation height is used in the visualization and validation. The model which updates the tool topography is used to evaluate the influence of galling on the coefficient of friction.

This galling model is calibrated using experimental data from hot strip draw tests performed at Tata Steel. This data is valid for a calibration of adhered volume over temperature. Both the galling initiation models are calibrated using these experimental values. Results from the model are used to evaluate the model for CFI and WFI on a few points: 1) the amount of asperities initiated for galling 2) the relation for adhered volume over temperature, pressure and strain, 3) the interaction between asperities based on the overlap an asperity has in a multi asperity situation and 4) the coefficient of friction over sliding length.

Using AutoForm and TriboForm the galling behavior on the tooling for three different part are visualized: 1) the experimental B-pillar from Tata Steel, 2) the industrial A-pillar from Volvo Cars and 3) the industrial Side Member from Volvo Cars. The predicted galling depends on the temperature, pressure and strain of the sheet during deformation and on the relative sliding distance in contact between the tool and the sheet. The experimental evaluation of the B-pillar is used to compare radii locations of the same part, where the CFI model shows the most promising results. The industrial parts from Volvo Cars are used to verify if the model can predict the galling locations observed on the tooling. The galling locations are accurately found on the industrial production parts by both models. However, the severity of a predicted galling location should be verified with further research. The CFI model is more favorable when comparing the two industrial parts.

Contents

Nomenclature

Greek Symbols

α	Fractional real contact area
α_{meso}	Fraction of area in contact on a meso level
α_{micro}	Fraction of area in contact on a micro level
$\Delta\gamma$	Adhesion energy
γ	Surface energy
μ	Friction coefficient
μ_i	Friction coefficient of a single asperity
ν	Increase in fractional real contact area
ϕ	Height distribution of contact surface
σ_c	Critical stress for crack propagation
τ	Fail criterion
τ	Shear strength (at the crack tip)
τ_{xy}, τ_{xz}	Tangential stresses
θ	Attack angle

Other Variables

Δ_s	Height increase
a	Crack length
a, b	Radius of elliptical asperity
A_H	Hamaker constant
A_i	Area of a single elliptical asperity base
A_n	Nominal area of contact
A_r	Real area of contact
B	Hardness factor
c	Constant value based on FEM simulation (l_b/h)
c_s	Scaling factor
c_{fr}	Calibration factor
c_{scale}	Scaling factor for hexagon base
D	Separation between two bodies
d	Separation
D_0	Separation between two bodies at atomic scale
F_a	Adhesion force
f_c	Shear factor
F_N	Total load carried by contact patches
F_n	Normal force on the asperity
F_w	Total friction force
H	Hardness
h	Height of asperity
k	Junction growth factor
k	Shear strength of material
k_w	Wear rate
K_{Ic}	Plane strain fracture toughness
K_I	Stress intensity factor
l,l_b	Lengths of hexagon based asperity
m	Fraction of V_{wear} (calibration factor)
T_b	Bulk temperature
T_c	Contact temperature
T_f	Flash Temperature
T_{crit}	Critical temperature
U	Constant raise of non-contacting surface
V_{trans}	Transfer volume
V_{wear}	Wear volume
w_I,w_{II},w_{III}	Widths of hexagon based asperity
Y	Dimensionless geometry parameter

Abbreviations

BLS	Boundary layer shear strength
CFI	Coating fracture initiation
COF	Coefficient of friction
fltr	from left to right
PHS	Press Hardening Steel
PVD	Physical vapour deposited
RMS	Root Mean Square
SMF	Sheet metal forming
UHSS	Ultra high strength steel
WFI	Wedge formation initiation

1 Introduction

In this section an introduction to the mechanisms involved with this project will be given followed by the objective of this research.

1.1 Sheet metal forming

Sheet metal forming (SMF) is a forming process where a blank sheet material is deformed into a desired form. This is commonly used in the automotive industry, for example in the production of car door panels. This process is illustrated in figure 1.1, where the sheet is already shown in a deformed position. The tooling used to deform a blank sheet material are called the punch, the die and the blank holder, where the die is the stationary part on the bottom side of the sheet, the punch is the moving part, on the top, that pushes the sheet into its desired form and the blank holder is an additional part to ensure that the edges of the sheet material are kept in check.

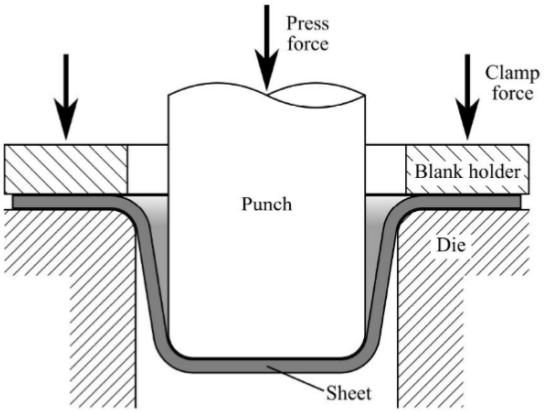

Figure 1.1: Overview of stamping setup.

This report concerns hot forming. Using elevated temperatures for the sheet material, which can go up to 750°C and even higher, during forming allows the production of a part with better material properties (linked to its crystal structure). These material properties arise during the cooling stage (quenching) of hot metal forming. The cooling rate of a steel material causes different structures (pearlite, bainite, martensite) within the material, which can provide a stronger material ($\approx$ 1500MPa). If these same strong material properties are achieved during cold forming, at which a metal is harder to deform, more force would need to be applied to deform the sheet material. The production process for cold forming could be insufficient and lead to fracture of the sheet material. In the figure below an overview of the steps taken in direct hot forming are shown. 1) The blank material (for example boron steel) is heated to austenitization temperature for 6 minutes in order to be formed more easily. 2) The blank is transported to the stamping machine, where it will be formed into the product and cooled while the tooling is closed. The cooling is done by quenching the product, which results in a strong material structure with strength values at 1500MPa. 3) The product will be transported again to perform post processing steps, like cutting of excess material.

1.2 Tribology system

During sheet metal forming the contact between the surfaces in contact is important for friction and wear, the tribology system. In figure 1.3 an overview of the parameters concerning the tribology

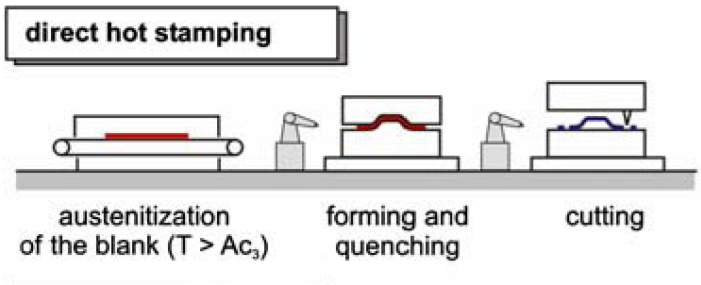

Figure 1.2: Schematic overview of a direct hot stamping process [1].

system is shown. The surface topography and material parameters influence the contact between the surfaces. In addition, the surface contact can be improved by adding an extra layer in between the surfaces, which provide the lubrication properties. Finally, the process conditions that dictate the forces, the velocity and the temperature of the tooling, but also the initial temperature of the blank sheet material influence the tribological behavior.

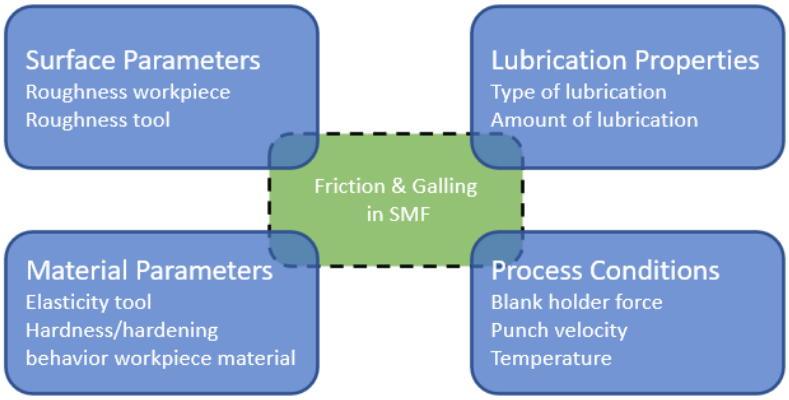

Figure 1.3: Elements of tribological system.

In the hot forming situation this tribological system excludes the lubrication properties, since no lubrication can be applied in hot forming processes. In direct hot forming ultra high strength steel (UHSS) with an aluminum silicon (Al-Si) coating is commonly used. In this report a boron UHSS (22MnB5) with an Al-Si coating will be used.

1.3 Galling

Galling is a type of adhesive wear, where material of the (relatively soft) sheet surface transfers to the (relatively hard) tool surface due to the relative motion. The material accumulates at the tool surface over multiple production cycles and eventually can damage the sheet surface, observed as scratches. The scratches on the product are unwanted and cause a disturbance in the production batch, because the tooling needs to cleaned or replaced. The amount of production cycles it takes for galling to be severe enough and cause these scratches depend on the parameters of the tribology system and the geometry of the production part. This wear phenomenon typically starts when there is direct contact between the tool and sheet. For cold forming this indicated that the lubrication would fail locally [2]. However, for hot forming this problem is more severe and more direct, because of the elevated temperatures in hot forming situations. At these high temperatures the system is subjected to extremer conditions and no lubrication can be applied. In figure 1.4 an

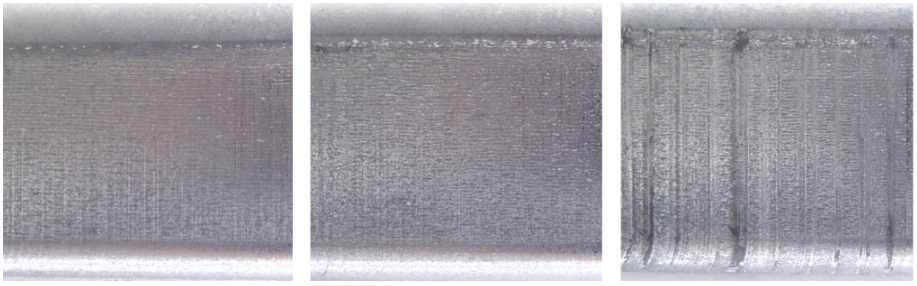

Figure 1.4: Scratches on product wall [3]. *Fltr: 1 product, 5 products, 50 products.*

example of the damage due to galling is shown. Also, galling influences the friction behavior, because the surface parameters of the tooling is changed due to the additional material on the tool surface.

1.4 Objective

Galling is an unwanted wear mechanism, which damages the sheet material. Therefore, it is desirable to predict the location an the severity of galling. The project is in collaboration with TriboForm Engineering and their software will be used and expanded upon to include a model for galling in hot forming. This model will then be calibrated using experimental data from Tata Steel. In addition, the galling model is visualized using software of TriboForm Engineering, which is in development and for internal use only, to validate with experiments and industrial production parts. The objectives of the current research are stated below:

Main objectives:

- Implement a model to predict galling in hot forming.
- Validate the galling behavior with experiments and experience on industrial parts

Sub objectives:

- Develop and evaluate a galling initiation criterion for asperities in contact.
- Identify the interaction between asperities within the galling model.
- Evaluate the effect of galling on friction behavior.
- Calibrate the galling model using experimental data (from Tata Steel).
- Visualize galling behavior on (industrial) production parts.

2 Literature review

The focus of this report will be on galling in hot forming, but to get there some other information is needed to understand the whole process of the model. In this section the background on the contact levels, friction mechanisms and wear mechanisms will be briefly touched upon. After that the experimental observations on the topic of friction and galling will be addressed for cold forming and hot forming. The last part of this section is used for a short introduction on existing models for galling in hot forming. The approach for galling can be seen in the diagram of figure 2.1.

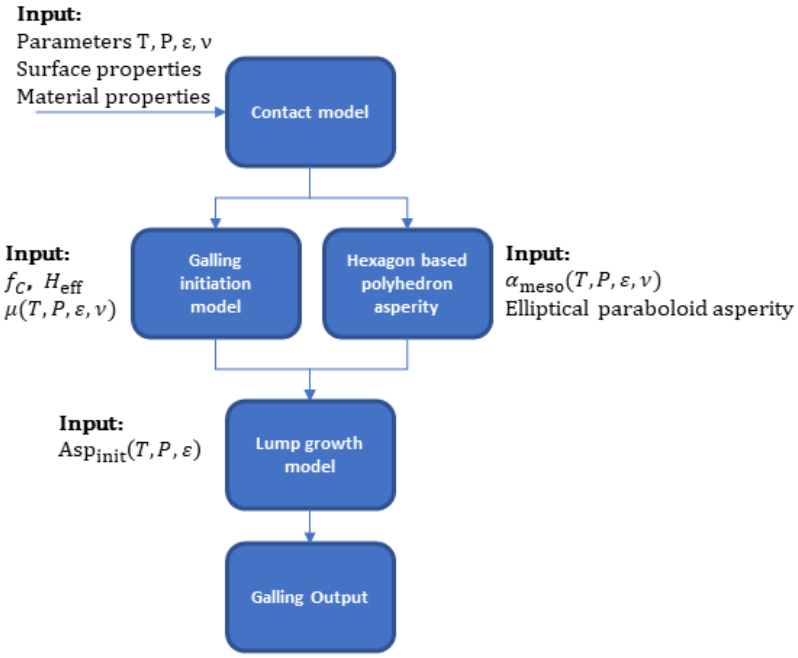

Figure 2.1: Diagram with the approach to solve galling in hot forming.

2.1 Contact

In general the tool has a hard and smooth surface while the sheet has a soft, rough and fresh surface. The contact between these two surfaces are divided into three length scales [4, 5]: Macro level, meso level and micro level. The contact levels are depicted in figure 2.2. Each level has a different contribution to the metal forming model, which will be elaborated on per level [5].

Macro level

The macro contact is the level of contact that is visible to the eye. On this level the physical quantities (contact pressure, stresses and strains) of the forming process are determined by ignoring the surface roughness of the tool and the sheet. So, this level is used to get physical bulk quantities, which are determined using a penalty method in FEM simulations. These quantities are applied as an input for the smaller scales [4].

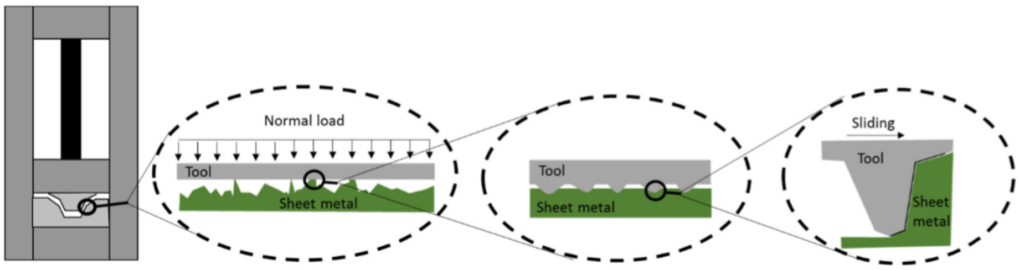

Figure 2.2: Contact levels [3]. *Fltr: macro level, meso level, micro level and single asperity at micro level.*

Meso level

At this level of contact the roughness of the sheet comes into play. This level of contact is mainly used to get the flattening of the sheet surface. At this point the sheet roughness is observed while the tool surface is still considered to be smooth, compared to the sheet surface. The smooth and hard tool flattens the rough peaks of the softer sheet material when contact pressure is applied. The size of the contact is calculated using energy and volume conservation of the real contact. For this it is assumed that the tool is rigid and ideally flat and that the sheet material deforms plastically. Also, the contact pressure (p_r) is assumed to be equal to the hardness (H), because ideal plastic behavior is assumed.

$$p_a = \alpha H \tag{2.1}$$

$$\alpha = \frac{A_r}{A_n} = \int_{h_z}^{\infty} \phi(z) dz \tag{2.2}$$

with p_a the apparent contact pressure, α the fraction of area in contact, A_r the real area of contact, A_n the nominal area of contact, h_z the separation of the surfaces and ϕ the height distribution function of the sheet surface. This flattening due to contact pressure also gives rise to strain of the bulk material due to the deformation of the surface roughness [4].

Micro level

The micro contact level takes a look at the plateaus formed due to the flattening at the meso level. At this stage the roughness of the tool can be observed. The peaks (asperities) of the harder tool surface scratches into the flattened plateaus of the sheet metal when the surfaces are in relative motion. This level of zoom on the contact between these two surfaces is interesting for galling, because material from the sheet material plateaus can transfer to the tool peaks under certain conditions. Galling is a wear mechanism which will be elaborated on later in section 2.4.3. Also, this level of contact is used to calculate the friction coefficient for certain conditions, which will be shown in section 3.3.3.

2.2 Material

In hot sheet metal forming the workpiece material needs to withstand more extreme conditions. This limits the number of materials suited for hot sheet metal forming. A commonly used workpiece material in hot forming is the ultra high boron strength steel (USHH) 22MnB5 with an Al-Si coating. This material combination will be used in this report and will be explained in more detail

in this section. Other material for the workpiece or coating is available and these will also be briefly mentioned here. Next to the workpiece material also a choice in the tool material with a suitable coating or surface finish needs to be made. In this research it is assumed to be an uncoated tool steel with a milled finish, but other options will be mentioned.

Substrate

The commonly used 22MnB5 is used in hot forming because the addition of boron increases the hardenability [1, 3, 6]. Also, the boron delays the transformation from austenite to ferrite and pearlite while the transformation to bainite and martensite is not influenced, see figure 2.3. This is a desirable trait because the martensite and bainite structures provide a harder and stronger material.

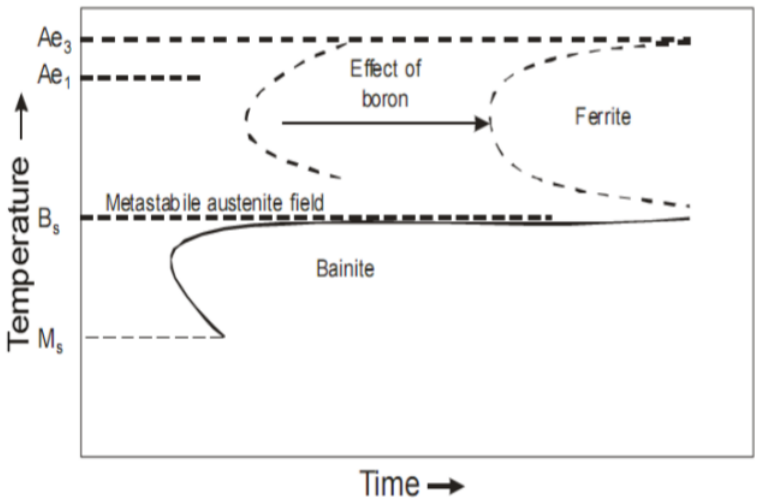

Figure 2.3: Schematic time-temperature-transformation (TTT) diagram on the influence of boron in steel [6].

Austenitization with Al-Si coating

In the heating step of the forming process the material and its coating are heated in a furnace to a temperature higher than the forming temperature and are kept at this higher temperature for a certain amount of time. This is done to ensure austenitization of the substrate material. This elevated temperature causes the composition of the coating, in this case Al-Si, to change due to the interface interaction between the coating and substrate [7, 8, 9, 10, 11]. Depending on the austenitization temperature, the amount of time in the furnace and the coating thickness, different layers in the coating (intermetallic phases) and different behavior [12, 11] is identified. Shortening austenitization time (range of 120s - 600s) leads to an increase in adhesive wear on hot stamping tool and an increase in COF, which shows for an austenitization temperature of both 880°C and 930°C , where the increase for the COF is less significant [12]. In figure 2.4 the composition and the cross section of intermetallic layers is shown based on a different heating temperature and on a different holding time.

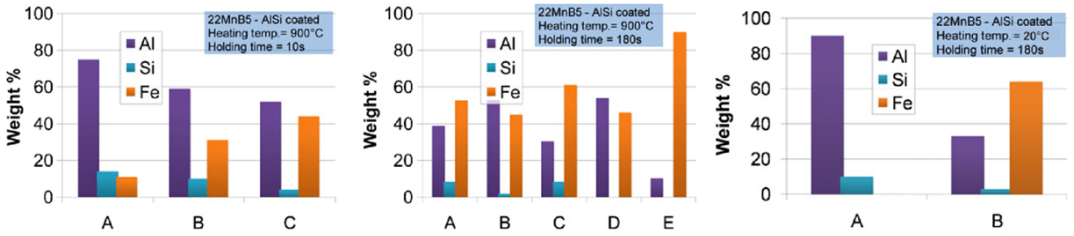

(a) Chemical composition.

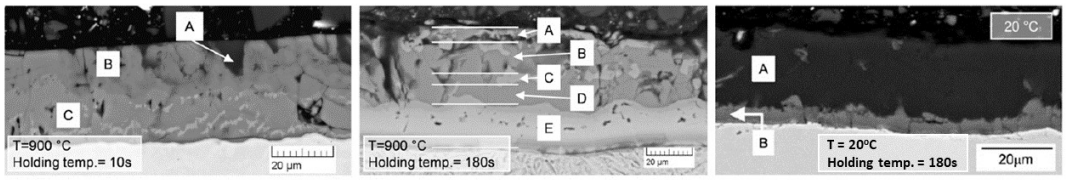

(b) Cross sections using Scanning Electron Microscopy (SEM).

Figure 2.4: Al-Si coating with different heating temperature and holding time. Adapted from [7].

Workpiece Al-Si coating

A coating can be added to the workpiece to influence the metal forming process on friction and wear behavior. The addition of a coating improves the corrosion resistance of the workpiece. The high temperatures in the forming process can cause the formation of oxide layers which reduce friction and can protects the underlying material from wear [13, 14]. Also, generated wear debris in the forming process can act as an intermediate and reduce friction and wear, because it prevents interlocking and prevents direct contact between the materials [13, 14].

An Al-Si coating shows a lower friction coefficient than an uncoated sheet material and an Al-Si coating with graphite shows a lower friction coefficient compared to a sheet with the Al-Si coating [15]. The improvement in the Al-Si with graphite coating is attributed to the lubricating action of the added graphite. On the other hand it also has been observed that the uncoated 22MnB5 steel shows a lower COF compared to the Al-Si coated sheet material [16]. However, the wear behavior for the uncoated sheet material is more severe than for the Al-Si coated sheet material.

The intermetallic phases that can arise when a Al-Si coating is applied in hot forming conditions, $Al_{13}Fe_4$, Al_5Fe_2, Al_2Fe and AlFe, are identified and studied by Windmann et al.[8, 9]. The AlFe phase has a much lower hardness compared to the other three phases, which possess a similar hardness. Also, the fracture toughness of the AlFe phase is higher compared to the $Al_{13}Fe_4$, Al_5Fe_2 and Al_2Fe phases. These three phases lead to abrasive wear and adhesive wear on the tool steel surface while the AlFe phase leads to only adhesive wear [9]. In the study by Pelcastre et al. [11] the $Fe_2Al_{7-8}Si$, Fe_2Al_2Si and $FeAl_2/Fe_2Al_5$ intermetallic phases are identified. Here, the $Fe_2Al_{7-8}Si$ shows severe galling because of its lower hardness compared to the other phases mentioned. This composition remains in the layer composition for an austenitization temperature of 700°C but completely dissolves for a longer austenitization time when the austenitization temperature is 900°C . The Fe_2Al_2Si layer is not present at the surface of the coating layer. The $FeAl_2/Fe_2Al_5$ layer shows mild adhesive wear (galling), because of its hardness and the formed oxide layer. On the other hand does layer also show abrasive wear on the tools due to its hardness. In this report an austenitization temperature of 930°C and holding time of 6 minutes is considered, which is in the stable range of the austenitization time [12] and leaves the Al_5Fe_2 and AlFe phases [17, 3].

Tool finish/coating

The tool surface can be prepared to improve wear behavior during contact by applying a different finish [1, 18] or by using a coating [16, 19, 20, 15]. Also, research has been done on the use of different steel grades for the tooling [21, 22].

The roughness and hardness of the tool have been analyzed with respect to wear behavior [18]. The roughness of the tool is controlled by the surface finish: ground, milled or polished. It has been found that the roughness has a significant influence on galling for low contact pressures, because more material transfer is possible when the surface has endured less flattening. In this case the hardness of a material does not show a significant influence. At a higher contact pressure (20MPa) more flattening of the surface occurs and the roughness of the surface becomes less significant. The hardness of the tool material provides a reduction in material transfer, but the formation of wear debris and adhesion is enhanced for higher contact pressures [18].

A coating can be applied to the tool steel to improve wear and friction behavior during contact: Physical Vapour Deposited (PVD) coating [20, 15, 16, 19] and Plasma nitriding [15, 20]. In literature different relations have been found concerning the COF and wear behavior for a PVD coating and plasma nitriding: According to Hardell [15] the coated tool steels show a reduction in wear compared to untreated tool steel, where plasma nitriding shows a small reduction and the TiAlN coating a significant reduction. Also, applying either of these coatings results in a lower COF compared to the untreated tool steel. In the paper of Pelcastre [20] the PVD coated tool steel shows more significant material transfer than uncoated tool steel, while the nitrided tool steel shows a reduction compared to the uncoated tools steel. The significant wear of the PVD coatings (AlCrN and TiAlN) is attributed to the chemical affinity and similar constituency between the Al-Si coated boron steel and the coating materials. The reduction of wear in plasma nitrided tool steel is due to the formation of an oxide layer which reduces the adhesive tendencies of the Al-Si coated sheet. Also, the effect of the severe wear for PVD caused unstable and high values for the COF. The COF for the nitrided tool steel provided are more stable, but also show high values for the COF. Then, according to Mozgovoy [16] the uncoated tool sliding against uncoated boron steel provides the lowers COF compared to coated tool steel sliding against the uncoated sheet steel (22MnB5) at high temperature. However, the friction behavior becomes similar for the uncoated and coated tool steel when the Al-Si coating is applied on the sheet material, indicating that friction behavior is governed by the Al-Si coating [16, 15]. Applying a PVD coating shows a reduction in the specific wear rate, although the PVD coated tools containing aluminium have more material build up than those without aluminium.

The use of different tool steel grades are compared to each other but also to nitrided tool steel grades. A low temperature (40°C) the COF is high, but it decreases as the temperature increases, which is attributed to the formation of oxide layers and intermetallic compounds [22]. The tool wear increases over temperature, where the nitrided tool steel grades are more favourable compared to the untreated tool steel grades. The wear of the Al-Si coated sheet material shows less adhesive wear due to the oxide layers and intermetallic compounds, especially with the nitrided tools [21, 22]. Also, the composition of the tool steel hardly influences the wear when they are all nitrided [22]. At high temperatures small hard precipitates in the material matrix of untreated tool steel seem more prone to material transfer and have less abrasive wear compared to large precipitates [21].

2.3 Friction

In this chapter a closer look will be taken at friction. Friction it is closely related to wear and is therefore addressed. First, the mechanism of friction and the components that make up the

coefficient of friction are addressed. As stated in the introduction in figure 1.3 the COF depends on the tribological system during a forming process, which is elaborated on in section 2.3.2. The final section will discuss the findings in literature under varying experimental conditions.

2.3.1 Mechanism

Friction is the resistance of two surfaces sliding in relative motion to each other. This resistance is expressed in the coefficient of friction, which is a property indicating the relation between the normal force and the friction force. In the relation in equation 2.3 the friction force, also called the Coulomb friction when it is a constant, can be seen as a threshold for when movement is about to start. This maximum force is also called traction.

$$F_w = \mu F_N \tag{2.3}$$

Friction within hot stamping is caused by energy dissipation. The contributing factors to the friction in this case is the energy needed to overcome the adhesive forces between the workpiece and tool surface, the ploughing of asperities through the workpiece surface as well as the tool surface and the flattening of asperities on the workpiece surface [23, 15]. The total coefficient of friction is mainly caused by the ploughing and adhesion between the interacting surfaces, the relation is shown in equation 2.4.

$$\mu_{total} = \mu_{ploughing} + \mu_{adhesion} \tag{2.4}$$

The ploughing component is caused due to the ploughing action of the harder asperities through the softer contacting material. The adhesion component depends on the interfacial shear strength and the hardness of the material, shown below.

$$\mu_{adhesion} = \frac{\tau_s}{H} \tag{2.5}$$

$$\text{with} \quad \tau_s = \frac{F_{adh}}{A_r} \tag{2.6}$$

where τ_s is the interfacial shear strength, H the hardness, F_{adh} the friction force due to adhesion and A_r the real area of contact [15].

2.3.2 Tribological system

The coefficient of friction is a property of the system. In figure 1.3 the material parameters, the surface properties, the process parameters and the lubrication properties are shown to have an influence on the friction coefficient. Here, the relation between each of these factors will be elaborated on further.

The friction is different when using different lubrication conditions, which influences the contact between the two surfaces. The amount of lubrication used in the process is classified in different regions according to the Stribeck curve presented in figure 2.5. The specific film thickness (λ) in this figure is defined as the ratio between the fluid film thickness (h) and the composite Root Mean Square (RMS) of the surface roughness (S_q), which provides three different regions when combined with the COF [24]. The regions are explained below.

- **Boundary lubrication:** The amount of lubrication fills the valleys of the surface roughness. During loading and/or sliding the stresses are fully carried by the surface asperities.

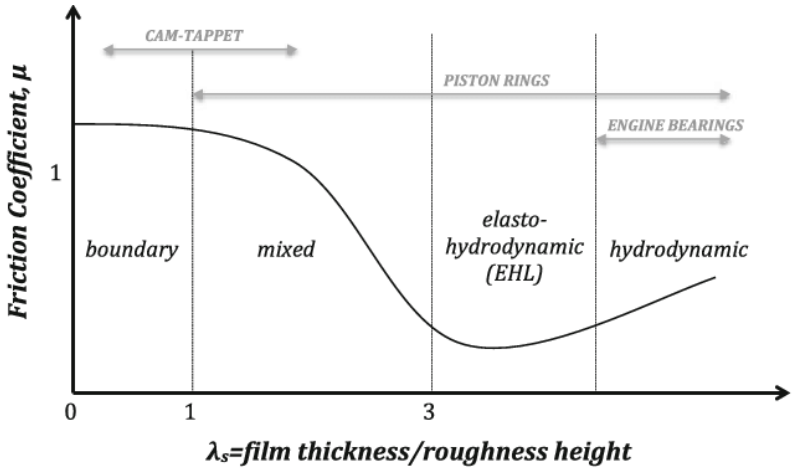

Figure 2.5: Stribeck curve [25].

- **Hydrodynamic lubrication:** This lubrication regime overflows the surface with lubricant. The load is then completely carried by the lubricant.
- **Mixed lubrication:** A combination of the previous two case is present in this regime. In the sense that the surface asperities as well as the lubrication both carry a part of the load applied.

The amount of lubrication used in a forming process does not imply the same region, because the roughness height in combination with the film thickness dictates which lubrication regime should be used. The real area of contact, at micro level, is between the asperities of the tool and the softer flattened asperities (plateaus) of the sheet. When the real contact is bigger the friction coefficient becomes lower, because the normal force is distributed over a larger area. The normal force also influences the real area of contact, because a larger normal force will provide more surface deformation, which creates bigger contact patches (contacting asperities). The deformation of the surface asperities depends on the material parameters. Therefore, the surface parameters, lubrication parameters, material parameters and process conditions are important for identifying the situation of the tribological system as in figure 1.3.

In hot forming the main difference to cold forming is the elevated temperature and, therefore, the material of the sheet material during forming. This causes the sheet material properties to change, which influences the interaction between the two surfaces. Also, due to the elevated temperatures it is difficult to apply lubricant, because at this time no lubricant is available which is stable at the high temperatures used in hot forming. In the TriboForm model concerning friction the boundary lubrication regime is used.

2.3.3 Process parameters

In literature it is found that the friction coefficient depends on multiple parameters and changes during the metal forming process. Here, the influence of temperature, pressure and velocity found in literature are summed up. The effect of the surface coating on the coefficient of friction has already been treated in the previous section on the material, section 2.2. In figure 2.6 an overview of the most common influences on the COF is shown with accompanying reasons to the behavior according to Schwingenschlögl et al. [13]. The relations described for the conditions below are focused on the UHSS with an Al-Si coating.

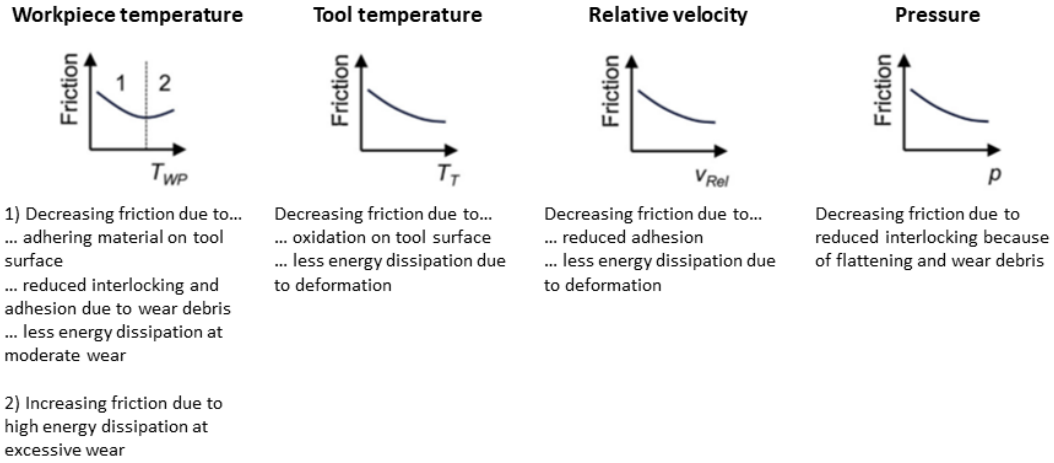

Figure 2.6: Overview of temperature, velocity and pressure effect on the friction coefficient for 22MnB5 with an Al-Si coating. Adapted from [13].

Temperature

In literature it is found that the friction decreases when the workpiece temperature increases [13, 26, 15, 27, 28, 29]. Also, for an increasing tool temperature the friction decreases (75°C - 375°C)[13], (25°C - 300°C)[29]. An exception for the relation of the workpiece temperature is found when higher pressures are applied, the decreasing trend of the coefficient of friction is interrupted for temperatures between 600°C and 700°C at which point the COF slightly increases [13]. The reason for the decreasing friction can be attributed to multiple things 1) the formation of an oxide layer on the workpiece surface, which reduces adhesive forces and in turn also the COF [14], 2) the reduction of shear strength of the coating, which leads to an easier deformation of asperities at elevated temperatures and therefore a lower COF [7, 27].

In contradiction, it is found that the coefficient of friction increases over temperature and greatly increases at 600°C [30]. This increase in COF is attributed to the occurrence of severe adhesive wear. Also, a combination of a decreasing and increasing COF has been observed. In this case the COF stops its decreasing trend when excessive grooving due to high temperature and high contact pressure occurs [13]. The trend of an initial decreasing COF and later on increasing COF for elevated temperatures has also been observed by Venema [3].

Pressure

The influence of pressure on the friction in hot metal forming is more difficult to check, because a pressure range is more difficult to simulate in an experimental set up. It is found that the coefficient of friction decreases for increasing pressure 2.5MPa - 7.5MPa [13], 6.5MPa - 15MPa [26], 5MPa - 25MPa [7], 10MPa - 20MPa [31]. The decrease in COF for high temperatures (500°C - 600°C) is explained as a result of the increased flattening of the roughness peaks due to a higher contact pressure [13, 7]. More flattening leads to less mechanical interlocking and therefore a lower friction. According to Ghiotti et al. [26] the influence of pressure is the least significant when compared to temperature or velocity.

Velocity

It is found that for an increasing relative velocity the COF decreases, 10mm/s - 120mm/s [13], 10mm/s - 60mm/s [26], 25mm/s - 75mm/s [30]. This is reduction in COF is shown for a Al-Si coated [26, 13] as well as a Zn-base [26] coated workpiece material. The effect is explained by the temperature rise due to frictional heat [3, 32]. Another explanation is the reduced adhesion, because for a higher velocity there is less time to create adhesive junctions [13, 31]. Also, no significant influence on the COF due to sliding velocity has been observed, 1mm/s - 10mm/s [7], 10mm/s - 100mm/s [31]. In the thesis of Mozgovoy [31] the influence of sliding velocity was only marginal, regardless of the contact pressure, for uncoated boron-steel as well as Al-Si coated boron steel, which is different from the other observations in literature. This is attributed to differing contact conditions when comparing the results.

2.4 Wear

Here, wear in hot forming will be discussed. Again, the mechanism will be discussed first. The wear mechanisms will be stated and the ones of interest will be explained in more detail. Then the wear modes will be elaborated on, which are also of importance for calculating the friction later in section 3.3.3. Of the wear mechanisms mentioned before some extra attention will be given to galling, because it is the goal of this research to predict the galling behavior with a model. Finally, this chapter will conclude with the finding in literature on wear under varying experimental conditions.

2.4.1 Mechanism

Wear is the loss of material from a surface due to relative motion with another solid, liquid or gaseous surface. The loss of material in SMF is experienced as a negative effect on the product, but also on the tooling. According to the German standard DIN 50320 [33] four wear mechanisms are classified [34]:

- **Tribochemical wear:** One or both the surfaces chemically react with components of the lubricant and/or the environment resulting in material loss.
- **Surface fatigue:** Due to cyclic stress variations in the contact crack form and start to grow resulting in material loss. The wear only occurs after a certain amount of time.
- **Abrasive wear:** The relative harder surface (or hard particles) scratches material from relative softer surface in relative motion.
- **Adhesive wear:** Material transfers from one surface to the other surface in contact in relative motion, because the bond of the material to its own surface is weaker than the bond to the other surface.

The wear mechanisms observed in the industry (and literature) for hot SMF are adhesive wear and abrasive wear. These two mechanisms contribute to the galling wear mechanism and are therefore elaborated on in more detail.

Abrasive wear

The abrasive wear is divided in two sub-mechanisms: two body abrasive wear, third body abrasive wear. In the two body abrasive wear the surface of one of the contacting surfaces is relative hard and relative rough compared to the other surface and causes scratches in this softer surface. Also, when relative hard particles are embedded in one of the contacting surfaces it can cause scratches

to the contacting surface. The third body abrasive wear mechanism occurs when hard particles are trapped between the two surfaces and can freely move around when the surfaces are in relative motion.

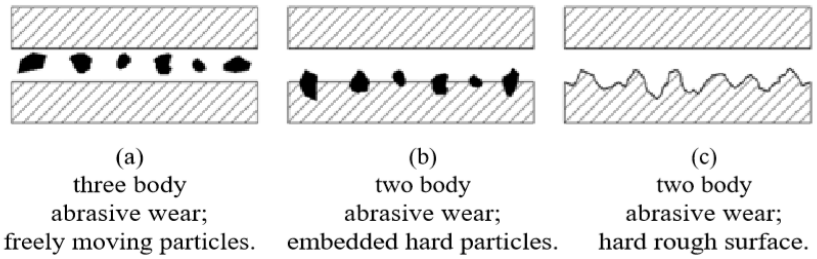

Figure 2.7: Abrasive wear mechanisms [34].

Adhesive wear

For adhesion to occur the interaction or adhesive force between the sheet and the tool needs to be sufficiently high. Adhesion is the attraction between two different atoms or molecules, where as cohesion is the attraction between two similar atoms or molecules. Different mechanisms can cause two materials to stick together:

- Mechanical interlocking: The contacting (rough) surface material hooks into valleys of the (rough) counter material, which sticks them together.
- Diffusion: Atoms diffuse across the interface of the two contacting surfaces, which cause particles from one surface to stick to the other like sintering.
- Electrostatic: Conducting material pass electrons at the interface, which creates electrostatic forces between the materials.
- Chemisorption: Chemical bonds are formed on the interface. These chemical bonds can be ionic, covalent or hydrogen bonds.
- Physisorption: The attraction between two molecules where each has a slight positive and negative charge. These are intermolecular forces, which are also known as 'Van der Waals' forces.

Here, the focus will be on chemisorption, mainly metallic bonding, and physisorption, which is the Van der Waals interaction between molecules (or atoms). Of these two adhesion mechanisms the metallic bonds are dominant when there is a short distance between the molecules (lower than 0.5nm) and the Van de Waals forces are dominating when there is a larger separation. In the adhesion theory the interaction energy is separated into a geometry dependent contribution and a material independent contribution. In the case of galling the material aspect of adhesion is more important, because distance between the particles and the tool approximate the atomic distance (when wear particle are assumed to be $\approx$ 10nm) [4].

The bond between material in contact is important for material transfer. The physical bond between material is determined by the interfacial and surface energies. Equation 2.7 shows the work of adhesion ($\Delta\gamma$), which is the work per unit area that needs to be done in order to separate two surfaces, one of material a and one surface of material b. The surface energies of material a and b are represented by γ_a and γ_b respectively and γ_{ab} is the interfacial energy between these two materials. The adhesive force of the interaction between two metals depends on their mutual solubility. A high mutual solubility between two metals indicates that the adhesion forces (γ_a and

γ_b) between the metals is strong. Also, this means that the interfacial energy (γ_{ab}) should be small and the work of adhesion ($\Delta\gamma$) is high. The compatibility of metal pairs, which are of interest for the material used in this report, are shown in figure 2.8.

$$\Delta\gamma_{ab} = \gamma_a + \gamma_b - \gamma_{ab} \tag{2.7}$$

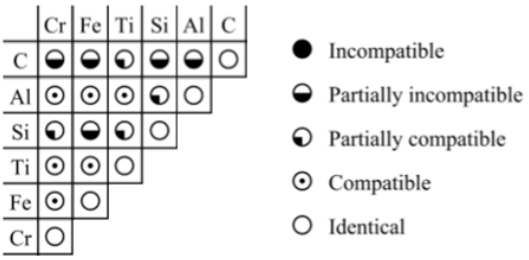

Figure 2.8: Compatibility pairs. Adapted from [35].

It is very difficult to determine the interfacial energy of two dissimilar materials and therefore the mutual solubility is used to determine the work of adhesion. This changes equation 2.7 to the relation below:

$$\Delta\gamma_{ab} = c_m(\gamma_a + \gamma_b) \tag{2.8}$$

where c_m is the compatibility parameter, which depends on the solubility category as presented in figure 2.8. In table 2.1 the values that belong to each solubility category are given. Note that the values give an indication and that the solubility categories are ranges. The surface energies are derived from clean metals, which is not valid for material used in forming processes due to contamination and/or oxide layers. However, the contact will be modelled as contact between two bare metals due to continuous shear that will take place in the wedge formation regime, which is linked to the initiation of galling (see section 3.4).

	Liquid	**Solid (RT)**	c_m
Identical			1.00
Comp.	yes	>1%	0.50
Part. comp.	yes	0.1 - 1%	0.32
Part. incomp.	yes	<0.1%	0.20
Incomp.	no		0.12

Table 2.1: Properties of mutual solubility categories [4, 35].

2.4.2 Wear modes

In literature three wear modes for cold forming have been identified [36, 37]: ploughing, wedging and cutting. These wear modes are mainly linked to abrasive wear, but also can relate to adhesive wear. From these wear modes a relation for the coefficient of friction is described, which will be explained in more detail in section 3.3.3. A single asperity is classified as one of the wear modes based on its attack angle (θ) and shear factor (f_C), see figure 3.7. The shear factor is the ratio between the shear strength of the boundary layer and the shear strength of the plastic deformed material (equation 3.6). The visual interpretation of the wear modes can be seen in figure 2.9.

In the cutting regime material is removed from the softer surface in the form of long ribbon-like chips or flakes. The wedging wear mode causes material flow in front of the asperity. Also, material is removed in this case, but the material is smaller and not shaped like chips or flakes. Then, material of the soft surface is displaced to the sides of the wear track according to the ploughing regime of the wear modes. In this case no material is removed from the surface. Ploughing also occurs in the cutting and wedging regime, but in a much smaller capacity [37, 2].

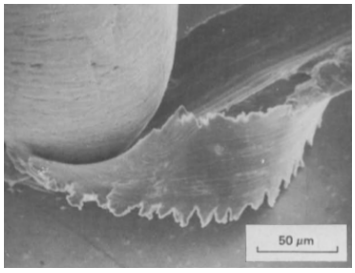

(a) Cutting of unlubricated brass by steel pin.

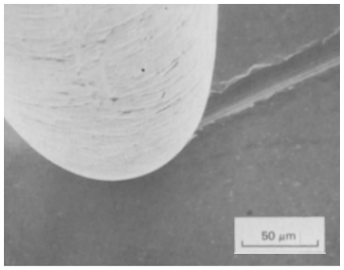

(b) Ploughing and ridge formation by a steel pin against unlubricated brass.

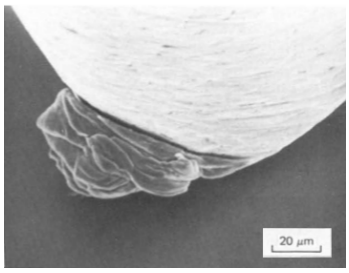

(c) Wedge formation by steel pin against unlubricated stainless steel.

Figure 2.9: Scanning electron micrographs of wear modes [37].

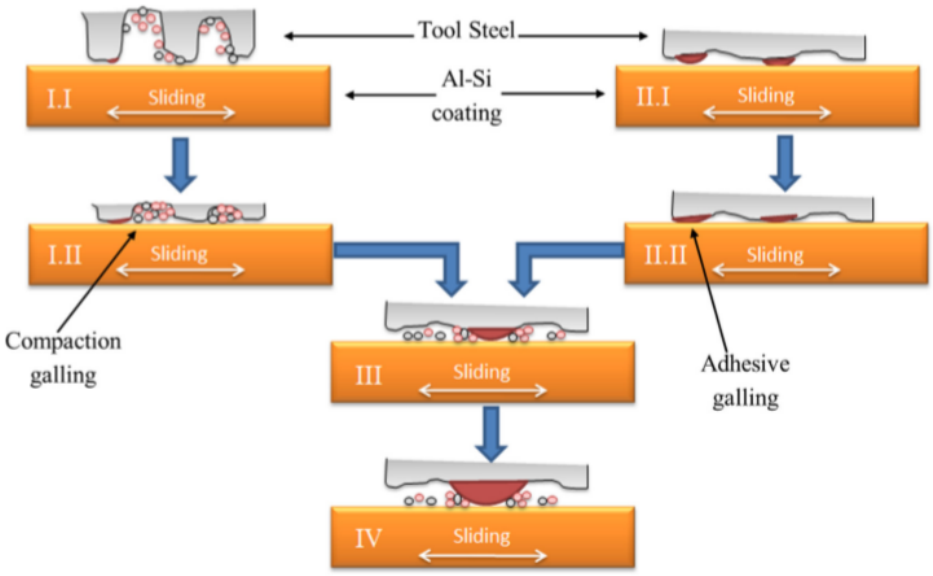

Figure 2.10: Schematic representation of galling mechanisms [20].

2.4.3 Galling

The wear mechanism of interest is galling, which is classified as a sub-mechanism of adhesive wear. The main process of operations of galling is divided into three phases [38, 39]: Initiation, Lump growth and Scratching. The initiation of galling is controlled by the adhesion of material from the sheet to the tool at the contacting areas, which is most likely to occur at defects and/or irregularities at the tool surface [40]. Once material is locally adhered to the tool it is most likely to accumulate more material in that location in subsequent forming cycles, because the initial adhered

material has made it a more clear irregularity. This is called lump growth. The locally formed tool lump grows with every formed product until it reaches a significant size, which causes damage to the surface of the product. This damage is in the form of scratches in the direction of the relative motion during forming. Also, the accumulation of material can cause a different cooling rate for the workpiece, which damages the workpiece as unwanted deformations during cooling.

Two initiation mechanisms for galling have been identified for uncoated tool steel and Al-Si coated UHSS. Galling on the tool surface occurs by direct adhesion (adhesive galling) and by accumulation and subsequent compaction of wear debris (compaction galling) [20]. Of these two galling types the compaction galling has been identified as the main contributed to galling [18, 20]. A schematic overview of the galling initiation mechanisms is shown in figure 2.10. In I.I and I.II the accumulation of wear debris for compaction galling is shown, where I.II also shows adhesive galling when the accumulation of wear debris is not possible anymore. In II.I and II.II only adhesive galling is observed, because no suitable sites are available for wear debris to get trapped and accumulate. The growth of the adhesive galling and compaction galling in these situation can, on its own, also act as an obstacle and contribute to enhanced galling, which is shown in III and IV.

2.4.4 Process parameters

Also, the effect of wear for hot forming has been studied in literature. Here, the influence of (high) temperature, pressure and velocity on the wear mechanism are discussed. The material has been discussed in section 2.2, which includes the influence of the surface treatment of the workpiece as well as the tool on wear behavior. An overview of the most common influences on the adhesive wear behavior is shown in figure 2.11 with accompanying reasoning according to Schwingenschlögl et al. [13]. The relations described for the conditions below are focused on the UHSS with an Al-Si coating.

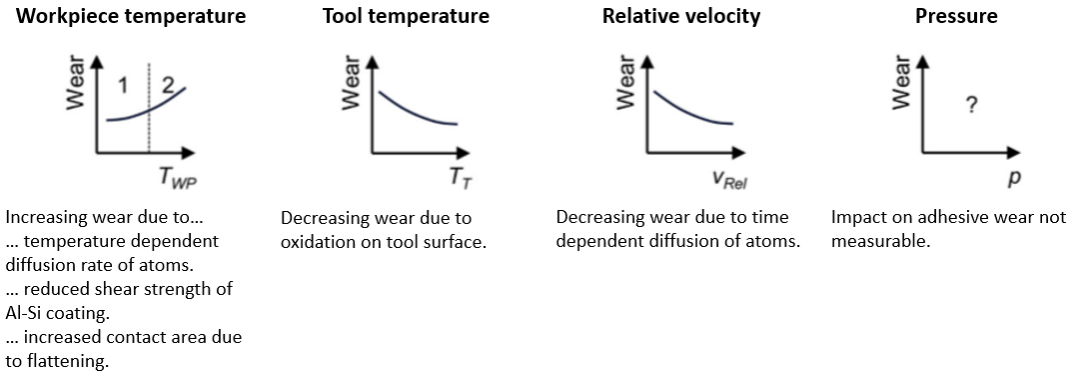

Figure 2.11: Overview of temperature, velocity and pressure effect on adhesive wear for 22MnB5 with an Al-Si coating.Adapted from [13].[1]

Temperature

At high temperatures abrasive and adhesive wear are present during relative motion in a forming process. The effect of temperature observed in experiments, mimicking the conditions of a forming

[1]The used pressure range (2.5MPa - 7.5MPa) does not show a clear relation for adhesive wear over pressure [13]. However, the general consensus is that an increase in pressure causes an increase in adhesive wear (galling).

process, is that the wear increases over temperature. However, the impact of abrasive and adhesive wear can deviate in the experiments.

It has been found that the adhesive wear increases over temperature and that it is the dominant wear mechanism at high temperatures; 530°C - 700°C [13, 41], 500°C - 800°C [9], 600°C - 800°C [42] and 500°C - 700°C [30]. This increase has been attributed to an increased diffusion rate for high temperatures [41] and to the brittleness and hardness of the coating and its intermetallic-phases (Al-Si coating), which is more brittle and harder at relative low temperature (500°C) [9, 30]. Also, it is noticed that the increase in adhesive wear is less significant from 600°C to 700°C compared to from 530°C to 600°C [13]. This is presumably caused by the formation of oxide layers, which prevent direct metal-metal contact and therefore reduce adhesion. Also, the oxide particles are a form of wear debris, which have an abrasive character [43].

On the other hand it has been found that abrasion is the dominant wear mechanism for the high temperatures (>600°C), while the adhesive wear shows more presents at lower temperatures [3, 27]. According to Medea et al. [27] the transformation from adhesion to abrasion is attributed to the decrease in hardness of the tool steel, which has a high thermal conductivity in this research, over temperature. The main cause for the dominant abrasive wear, according to Venema [3], is the loose debris from the coating and embedded debris in the coating at higher temperatures, because the coating hardness is lower for high temperatures.

Also, the effect of the tool temperature on wear has been analyzed. Here, the adhesive wear is reduced when using elevated temperatures (75°C - 375°C) [13]. This is caused by the formation of oxide layers, which prevent direct metal-metal contact. However, the effect of abrasive wear due to increased tool temperatures is not mentioned.

Pressure

An increase in material transfer over pressure has been observed in literature; 10MPa - 20MPa [1, 18, 31]. A possible explanation, by Pelcastre [1], for this behavior is that higher pressure allowed easier adhesion of the coating and compaction of wear debris onto the tool surface even though more flattening occurs, which reduces the sites for debris entrapment. Similarly, it is explained by Mozgovoy [31] that more adhesive junctions are building up for a higher contact pressure, while the plastic deformation of the material surfaces results in a better adaptation to each other.

Also, no significant impact has been seen in the experiments of Schwingenslögl et al. [13, 41], which use a pressure range from 2.5MPa to 7.5MPa. At first [41] the opposite relation for adhered material was concluded, more transfer material at lower pressures, but this conclusion has been changed to no significant impact over pressure [13].

Velocity

The wear behavior regarding the impact on velocity has been observed in literature. The general finding states that more adhesive wear is seen for slower relative velocities; 30mm/s - 120mm/s [41], 10mm/s - 120mm/s [13], 25mm/s - 75mm/s [30] and 10mm/s - 100mm/s [31]. The increased adhesion for slower velocities is attributed to the longer time in contact. This provides more time to form adhesive junctions [31] and also provides more time for diffusion of atoms [13, 30].

2.5 Models

The models used for this project will be discussed in the next section, *Galling model*. Here, findings in literature concerning applied relations in the lump growth model will be elaborated on, to preserve continuity in the section regarding the lump growth model.

The growth model is applied to the asperities initiated for galling. This model considers material to adhere to the tool asperities, which connects the growth of an asperity to adhesive wear. The model for asperity growth, as a main reference, is developed by van der Linde [4], which is developed for cold forming purposes. The volume used for the growth (V_{trans}) of an asperity is a fraction of amount of material that will is worn of (V_{wear}) by an asperity, which is shown in equation 2.9. In this equation the worn volume defined by Archard [44] is used, see equation 2.10. Also, the transfer volume according to equation 2.9 is not the final amount of volume, because the final volume depends on the stability of the asperity the material adheres to. This procedure will be explained in more detail in section 3.5.

$$V_{trans} = c_{fr}\Delta\gamma l_{slide} k_w F_n \tag{2.9}$$

$$k_w = \frac{V_{wear}}{l_{slide} F_n} \tag{2.10}$$

Addition information concerns the equations above will be elaborated on. First, the lump growth model is developed for cold forming and therefore might not hold for hot forming. Now, this model still will be applied to see how well it performs when used in hot forming conditions. However, the wear rate k_w and the adhesion energy $\Delta\gamma$ from the equations above are different over temperature.

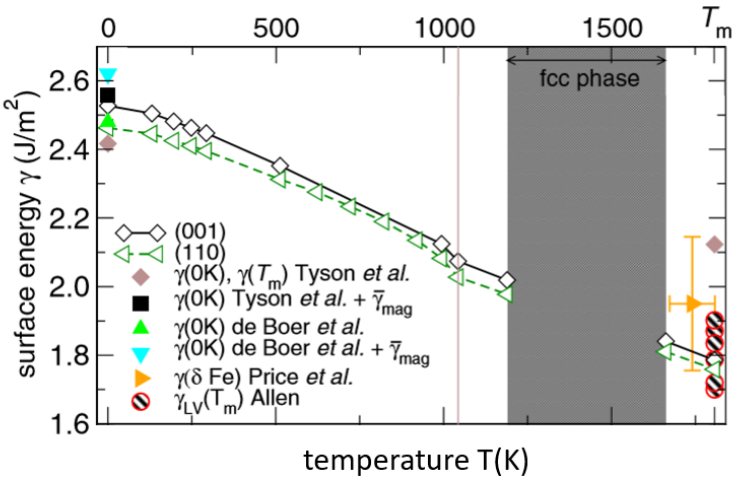

Figure 2.12: The temperature effect on the surface energy of the (110) and (001) facets of body centered cubic (bcc) Fe. Adapted from [45].

The wear rate (k_w) used in the thesis of van der Linde [4] is copied in this report, which is based on the wear modes proposed by Challen and Oxley [36]. In literature different values for k_w are found. In the study of Lee and Jou [46] on a warm forging process the temperature of the die varies from 100°C to 400°C and therefore the hardness and wear rate are not constant. Here, the wear rate is determined as a function of temperature using Archard's wear theory. Also, Deng et al. [47, 48] use a temperature dependent wear rate in a modified Archard wear model for their wear and galling predictions. The Archard equation used in this case, equation 2.11, where g is the galling growth rate, V the volume gain, F the normal force and s the sliding distance. Later, Deng et al. [49] present a model with quantitative galling results dependent on pressure and temperature. Again, the modified Archard's wear model is used where the wear rate (or galling growth rate)

is calibrated on the experiments with varying pressure (5MPa - 15MPa) and varying temperature (600°C - 800°C).

$$g = \frac{V}{Fs} \tag{2.11}$$

The adhesion energy ($\Delta\gamma$) from equation 2.9 in the thesis of van der Linde is assumed to be a fixed value for a certain material at room temperature, for iron $\Delta\gamma \approx 2.4 Jm^{-2}$ [50]. The value used at room temperature is not the same for hot forming temperatures. In fact, the adhesion energy changes over temperature. Figure 2.12 shows the iron-iron surface energy decrease while temperature increases for Fe with two different sliding planes [45].

2.6 Limitations

The general outline for the approach has been described above in the models section, but there are still some limitations present which will be summarized here.

- The models used in this research are based and verified on cold forming, but are applied for hot forming conditions. Assumptions valid for cold forming do not necessarily have to be the same for hot forming (for example the COF based on the wear modes from Challen and Oxley, the use of Archards wear equation and the adhesion energy for metal at elevated temperature).
- The assumptions made in the equations used in the worn volume and the transfer volume do not include temperature dependency for the wear rate and the adhesion energy. Temperature is the main influence, which will be calibrated for in section 5.
- The lump growth model only considers growth of a single asperity, but does not include interaction between the multiple growing asperities. Examples of the interaction are 1) the merging of asperities due to material transfer and 2) the direction dependent asperity contact, which causes less available material for asperities that will come into contact later. In section 6 an investigation on the overlap of galling initiated asperities during growth will be done.
- The lump growth model is based on the addition of material due to adhered material while compaction galling is also a significant contributing factor to galling. Here, the model will be calibrated without making a distinction between the way volume is added to the tools.
- A lump does not keep growing infinitely. At a certain point the growing asperity cannot withstand the forces acting on it anymore and will break of causing wear debris. This debris interacts with the surfaces and is therefore not included.

3 Galling model

In this chapter the models connected to galling are described. A schematic overview of the galling model is already given in figure 3.11. First, the topography of the workpiece material and tool material are shown to get a feeling of the material dealt with later in the experiments and validation. Followed by the material model fro hot forming. Then the schematic overview will be followed. Starting with the contact model already in use in the TriboForm Solver will be addressed. The contact area, friction and asperity shape from the contact model will be used in the galling models, which are the galling initiation model and the lump growth model. The galling initiation model shows the criteria for which an asperity will be a contributing factor to galling. Two different galling initiation model will be proposed. This is followed by the lump growth model, which shows how adhered material will be deposited on the galling initiated asperities. In addition, the multi asperity lump growth shows how the single asperity lump growth is used for an area in contact, which will be shown for two different cases.

3.1 Topography

The material used in this report is 22MnB5 with an Al-Si coating for the sheet and a mill finished tool steel for the tooling. The topography and surface height distribution of these two surfaces are shown in figure 3.1 and figure 3.2 for the tools and sheet respectively.

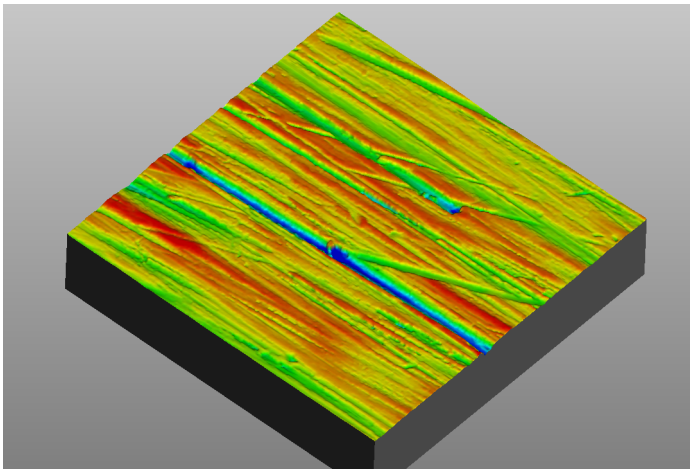

(a) Topography.

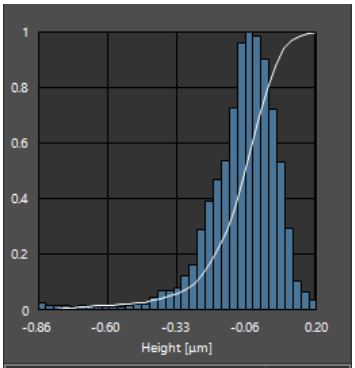

Pixel size X [µm]	2.57
Pixel size Y [µm]	2.59
Dimension X-direction [mm]	1.00
Dimension Y-direction [mm]	1.00
Roughness Sa [µm]	0.60
Roughness Sq [µm]	0.86
Roughness Sz [µm]	5.92
Skewness Ssk [-]	-1.93
Kurtosis Sku [-]	8.85
Texture ratio [-]	0.05
Texture direction [°]	-2.48

(b) Surface height distribution.

Figure 3.1: Tool surface.

3.2 Material model

In this section the material specific values that are used in the contact and galling model will be elaborated on. The material model for hot forming will be discussed. Then, the high temperatures lead to changes in the shear factor, which is of importance in determining the coefficient of friction in the contact model. The use of the shear factor will be explained in section 3.3.3.

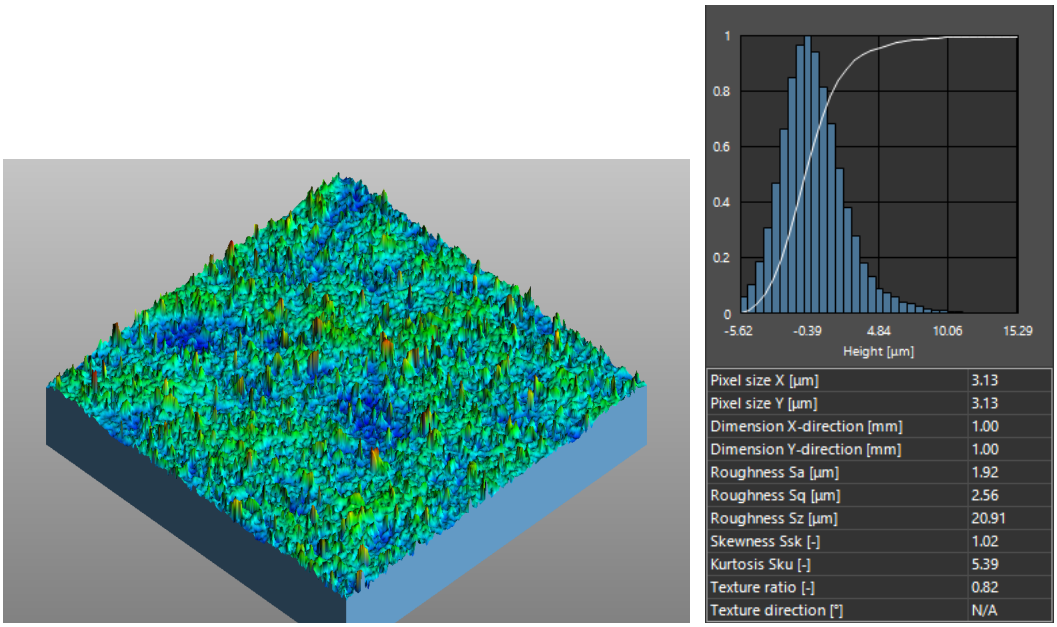

(a) Topography. (b) Surface height distribution.

Figure 3.2: sheet surface.

Abspoel van Liempt hardening

In TriboForm the material model according to hardening law proposed by Abspoel and van Liempt [51] for hot forming is used. This model has been tested in the temperature range of 500°C to 900°C and the boundaries for the strain rate are 0.1/s till 10/s. The flow stress (σ_f) is described as a summation of the athermal limit of the yield stress (σ_0), a stress due to thermal activated dislocation glide (σ^*) and a strain dependant work hardening component (σ_w).

$$\sigma_{\mathrm{f}} = \sigma_0 + \sigma^*(\dot{\varepsilon}, T) + \sigma_{\mathrm{w}}(\varepsilon, \dot{\varepsilon}, T) \tag{3.1}$$

with $\dot{\varepsilon}$ the strain rate, T the absolute temperature and ε the plastic strain.

The contribution of the thermally activated stress component can be isolated by taking a look at the stress at the moment of yielding. At that point no contribution due to work hardening is present. Therefore, the yield stress (σ_y) can be described by a static and a dynamic part.

$$\sigma_y = \sigma_0 + \sigma_0^* \cdot \left[1 + \frac{k_b \cdot T}{\Delta G_0} \cdot \ln\left(\frac{\dot{\varepsilon}}{\dot{\varepsilon}_0}\right)\right]^{m'} \tag{3.2}$$

with σ_0^* the dynamic stress at zero thermal activation, k_b the Boltzmann constant, ΔG_0 the maximum activation energy (material specific constant), $\dot{\varepsilon}_0$ the strain rate for thermal activated movement (material specific constant) and m' a strain rate exponent.

Then, to describe the work hardening component a physical model using dislocation theory is used. The flow stress is written as yield stress and a stress component as a function of the shear modulus (G) and dislocation density (ρ).

$$\sigma_{\mathrm{f}} = \sigma_{\mathrm{y}} + \alpha \cdot G \cdot b \cdot \sqrt{\rho} \tag{3.3}$$

with α the Schmidt factor and b the Burgers vector. Utilising the relation between the dislocation

density and work hardening the equation can be rewritten.

$$\sigma_{\mathrm{f}} = \sigma_{\mathrm{y}} + \left(\frac{U'}{\Omega}\right) \cdot \left[1 - \mathrm{e}^{-(\Omega(\dot{\varepsilon},T)/2)\cdot\varepsilon}\right] \tag{3.4}$$

with U' the normalized hardening parameter and Ω the parameter describing the annihilation an remobilization of dislocations. Combining equation 3.2 and 3.4 the flow stress as a function of temperature, strain rate and strain looks like:

$$\sigma = \sigma_0 + \sigma_0^* \cdot \left[1 + \frac{k_b \cdot T}{\Delta G_0} \cdot \ln\left(\frac{\dot{\varepsilon}}{\dot{\varepsilon}_0}\right)\right]^{m'} + \left(\frac{U'}{\Omega}\right) \cdot \left[1 - \mathrm{e}^{-(\Omega/2)\cdot\varepsilon}\right] \tag{3.5}$$

Here, σ_0,σ_0^*,$\dot{\varepsilon}_0$, U' and Ω are unknown parameters, which is determined using strain-stress data [51, 52]. The values based on Tata Steel material data, which are also used in the TriboForm Solver, are shown in table 3.1.

Parameter	Unit	22MnB5 - Tata Steel (Abspoel)
σ_0	[MPa]	44
σ_0^*	[MPa]	188
$\dot{\varepsilon}_0$	[1/s]	10^6
k_b	[eV/K]	8.617×10^{-5}
ΔG_0	[eV]	1.8
U'	[MPa]	$-10T + 13500$
Ω	[-]	$-1.7372\ln(\dot{\varepsilon}) + 18$

Table 3.1: Fitted parameters of the Abspoel van Liempt hardening model.

Shear factor

The shear factor is used in determining the friction contribution of an asperity as will be seen in section 3.3.3. The relation for the shear factor is shown in the equation below.

$$f_C = \frac{\tau}{k} \tag{3.6}$$

with τ the shear strength of the interfacial boundary layer and k the bulk shear strength of the plastically deforming material. The boundary layer shear strength for cold forming is described in equation 3.7

$$\tau = C\left(\frac{p}{p_0}\right)^n \tag{3.7}$$

with C a constant in [Pa], p the applied contact pressure, p_0 the reference pressure and n a fitting parameter. Here, p is equal to the hardness (H) of the softer material, because full plastic deformation is assumed. The shear strength of the workpiece material (k) is derived from the Von Mises criterion for pure shear and is shown in the equation below.

$$k = \frac{H}{B\sqrt{3}} \tag{3.8}$$

with H the hardness of the material and B the hardness factor. This hardness factor for steel materials in cold forming is experimentally obtained using Brinell hardness tests [53]. The relation for

the shear strength holds for approximately ideal-plastic behavior, which is present during a Brinell hardness test. Changes in the stress state, geometry of indenter or bulk strain will change the value of this hardness factor [24]. The value of the hardness factor for the material, used in this report (22MnB5), in hot forming is calibrated, $B = 1.25$. The hardness factor is obtained via calibrated using the real area of contact during normal loading only.

The shear factor for hot forming used in the TriboForm Solver in shown in equation 3.9 and visualized in figure 3.3. This does not use the relation of equation 3.6, because it does not hold for hot forming situations. Therefore, the shear factor is calibrated using experimental data [32].

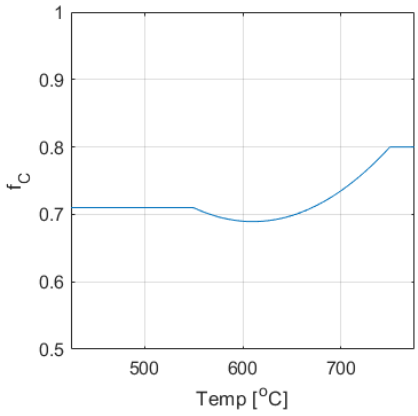

Figure 3.3: Shear factor for hot stamping as a function of temperature.

$$\begin{aligned} &\text{for} \quad T < 550^oC && f_C = 0.71 \\ &\text{for} \quad T > 750^oC && f_C = 0.80 \\ &\text{for} \quad 550^oC < T < 750^oC && f_C = 5.667e^{-6}T^2 - 6.917e^{-3}T + 2.8 \end{aligned} \tag{3.9}$$

3.3 Contact model

A contact model for the boundary lubrication regime is used to get the real contact area on the micro scale. The real contact area contains the surfaces of each patch of the tool in contact with sheet after normal loading, bulk deformation and sliding deformation (section 3.3.1). The approach, applied within the TriboForm Solver, to determine the contact area is adopted from the thesis of Hol [24] and will only be addressed briefly. These asperity contact patches are used to determine an elliptical asperity shape, which is more convenient in further calculations (section 3.3.2). This elliptical asperity is used to calculate the friction coefficient of each single asperity and of the total amount of asperities of the contact area (section 3.3.3). The determination of friction will be shown, because the wear mode diagram is used in a galling initiation model, section 3.4 *Initiation based on wedging regime*, and because the evolution of friction over sliding length due to galling will be assessed, section 3.6.2.

3.3.1 Contact area

The deformation of a rough surface due to normal loading, sliding deformation and bulk deformation is used to determine the contact area [24], in figure 3.4 the flattening is visualized. The roughness of the workpiece is modeled with bars as shown in figure 3.5.

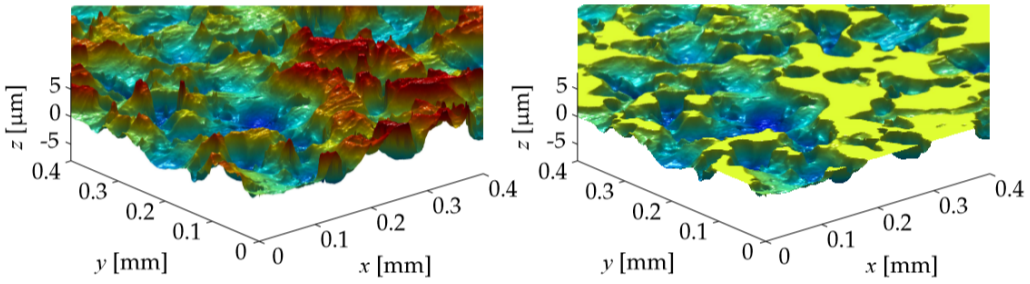

Figure 3.4: 3D surface texture of the undeformed workpiece *(left)* and deformed workpiece *(right)* [24].

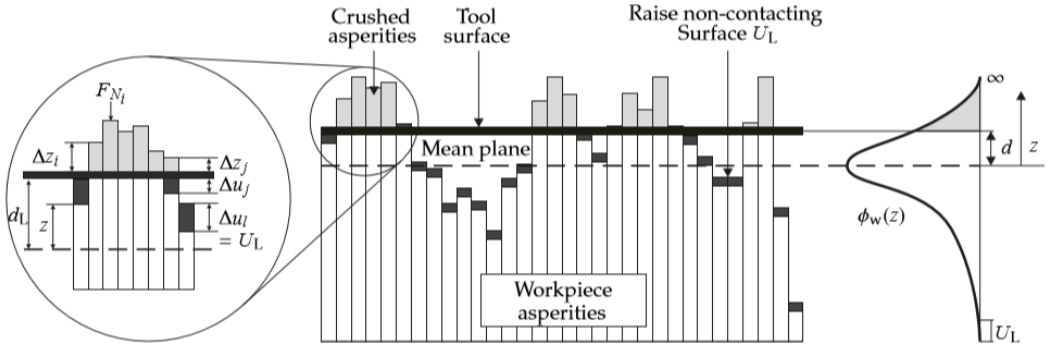

Figure 3.5: A relative soft surface (workpiece) crushed by a rigid and perfectly flat surface (tool) [24].

The flattening of the rough surface due to normal loading uses energy conservation and volume conservation to find the real contact area [24, 54]. The internal energy needs to be equal to the external energy when energy conservation is applied. Here, the external energy is the energy required by the tool to crush the contacting bars of the asperities. The internal energy is described by the energy absorbed by the crushed bars ($W_{int,ab}$), the energy needed to lift non-contacting bars ($W_{int,ri}$) and the energy to shear bars in relative motion ($W_{int,sh}$), see equation 3.10. The volume conservation requires that the volume of the crushed bars (N) is equal to the volume of the raised bars (N^* and N^{**}, bars coming into contact and bars not coming into contact respectively), see equation 3.11.

$$\begin{aligned} W_{ext} &= W_{int} \\ W_{ext} &= W_{int,ab} + W_{int,ri} + W_{int,sh} \end{aligned} \tag{3.10}$$

$$\sum_{i=1}^{N} \Delta z_i \Delta A = \sum_{l=1}^{N^{**}} \Delta u_l \Delta A + \sum_{j=1}^{N^*} \Delta u_j \Delta A \tag{3.11}$$

with Δz the crushing height of the bars and Δu the raise of the bars (figure 3.5).

Then, the sliding deformation, which is combined with the normal loading case, is applied [24, 53]. This includes an increase in area due to the sliding contact between surfaces. The real fractional contact area (α) needs to grow to satisfy equilibrium when micro level contact is considered, because the tool is no longer assumed to be perfectly flat at this level. Also, the real contact area grows due to additional tangential load caused by sliding, called junction growth. Equation 3.12 shows the increase in fractional real contact area (ν), which depends on the junction growth

factor k and the friction coefficient μ. The junction growth factor used in this research is $k = 135$, which is calibrated to match the shear factor for hot forming in section 3.2.

$$\nu = \sqrt{1 + k\mu^2} \tag{3.12}$$

Finally, the bulk deformation is applied [24, 54], which is also combined with the normal loading case. The bulk deformation includes further plastic deformation of asperities due to stresses, perpendicular to the normal loading direction, applied by the normal loading. This causes more flattening of the contacting asperities and, therefore, causes an increase in real contact area (A_r). This is also known as a decrease in the effective hardness (H_{eff}) due to bulk straining of underlying material, see equation 3.13.

$$H_{\text{eff}} = \frac{p_{nom}}{\alpha} \tag{3.13}$$

3.3.2 Elliptical paraboloid asperities

The contact area used in the previous section is based on elliptical paraboloid asperities. These asperities are obtained using the following steps. First, the contact area is determined using force equilibrium. The contact area dictates how much the tool needs to indent the sheet to get the same contact area. From this, the contact patches can be defined using '*connected components labelling*'. This image processing technique uses a group of pixels that is connected with an edge or a corner to define a elliptical asperity base, figure 3.6 *(left)*. These pixels (or bars) each have a certain height and therefore a certain volume, figure 3.6 *(middle)*. The volume is used to determine, using volume equilibrium, the paraboloid on top of the elliptical base. This provides an elliptical based paraboloid asperity from which geometrical properties are used in later calculations, figure 3.6 *(right)* [24].

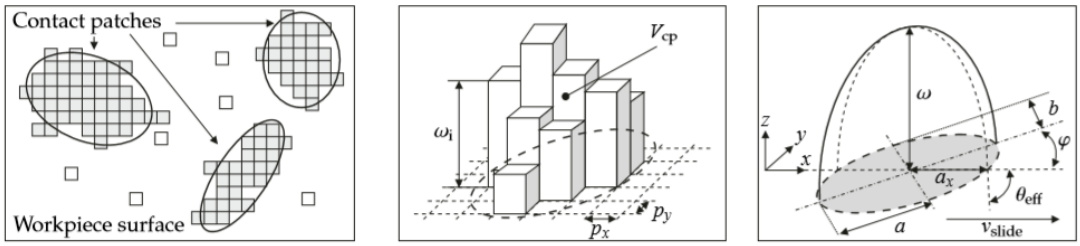

Figure 3.6: Schematic overview from contact patch to elliptical paraboloid [24, 55].

The base of the elliptical paraboloid is approximated by an ellipse that has the same normalized second central moment as the pixel patch identified by the image processing technique. The volume of the elliptical paraboloid (V_{ell}) is shown in the equation below:

$$V_{\text{ell}} = \int_0^{\omega} \pi a'(z) b'(z) \mathrm{d}z = \int_0^{\infty} \frac{\pi ab}{\omega} z \, \mathrm{d}z = \frac{\pi ab\omega}{2} = \frac{A_{\text{ell}}\omega}{2} \tag{3.14}$$

$$\text{with} \quad a'(z) = a\sqrt{\frac{\omega - z}{\omega}} \quad \text{and} \quad b'(z) = b\sqrt{\frac{\omega - z}{\omega}} \tag{3.15}$$

where a is the major axis and b is the minor axis of an ellipse, ω is the indented distance into the softer surface and therefore also the height of the elliptical paraboloid asperity. This height is

determined by assuming that the contact area and the volume of the elliptical paraboloid is equal to that of the identified contact patch, conform to the volume equilibrium mentioned before.

$$\omega = \frac{2V_{\text{ell}}}{A_{\text{ell}}} = \frac{2V_{\text{cp}}}{A_{\text{cp}}} = \frac{2p_x p_y \sum_{i=1}^{n} \omega_i}{n p_x p_y} = \frac{2}{n} \sum_{i=1}^{n} \omega_i \tag{3.16}$$

with n the number of pixels, p_x the pixel size in x-direction, p_y the pixel size in y-direction and ω_i the height of each pixel. Also, the subscript 'ell' refers to the elliptical paraboloid and 'cp' refers to the discrete contact patch.

From the definition of the elliptical paraboloid the effective attack angle (θ_{eff}) between the tool asperity and the sheet surface can be defined as in the equation below.

$$\theta_{\text{eff}} = \arctan\left(\frac{2\omega\sqrt{(b\cos\varphi)^2 + (a\sin\varphi)^2}}{ab}\right) \tag{3.17}$$

where ϕ is the orientation angle between the horizontal axis (sliding direction) and the major axis (a) of the ellipse.

However, this effective attack angle is based on a 3D plane strain expression, which is not valid when applied to the 3D nature of the contact patch and consequently the elliptical paraboloid. To compensate for this transition the shape factor χ, introduced by Hokkirigawa and Kato [37], has been added to modify the effective attack angle as seen in equation 3.18. The shape factor is unique for every tool-sheet combination and therefore sliding experiments should be performed to get a more reliable value for the shape factor.

$$\theta = \arctan\left(\frac{2\omega\sqrt{(b\cos\varphi)^2 + (a\sin\varphi)^2}}{\chi ab}\right) \tag{3.18}$$

3.3.3 Friction coefficient

First, a single asperity friction case will be discussed, which is at the micro level of contact. Then, the single asperity case is applied for each asperity in the multi asperity case. Each of these single asperities has its own contribution to the total friction of the contact area, where the interaction between asperities is not accounted for.

Single asperity contact

The contact model of Challen & Oxley [36, 37] is used to get the friction coefficient for a single asperity. The model is developed on a 2D slip-line field assuming plane strain deformation and ideal plastic behavior. The model describes three wear modes: cutting, ploughing and wedge formation (figure 2.9). The active mode for a certain asperity is determined by the wear mode diagram, see figure 3.7. The mode depends on the attack angle (θ) and the shear factor (f_c). The definition of the attack angle is shown in equation 3.18. The shear factor for hot forming conditions is found using equation 3.9, where it is a function of temperature. The mathematical approach of determining the coefficient of friction for cutting, ploughing and wedging can be found in appendix A.1.

Multi asperity contacts

The multi asperity friction model uses all the tool asperities in contact with the softer work piece material to determine the COF for a surface area [24, 55]. Each identified contact patch needs to go through the single asperity case described above: identify contact patch, transform contact patch to

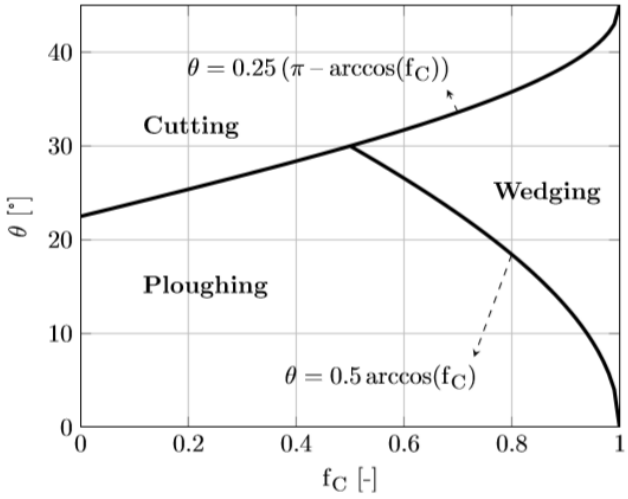

Figure 3.7: Wear mode diagram [17].

elliptical paraboloid and use this shape to determine the individual friction coefficient according to the wear modes. After that, the friction coefficient of the surface area is obtained by dividing the total friction force F_w by the total load carried by the contact patches F_N, which can be seen in the equation below:

$$\mu = \frac{F_\mathrm{w}}{F_\mathrm{N}} = \frac{\sum_{i=1}^{m} \mu_i(\theta_i) A_i H}{\sum_{i=1}^{m} A_i H} \tag{3.19}$$

with m the number of contact patches, μ_i the friction coefficient of a single asperity, A_i the area of the elliptical base of the asperity and H the hardness.

3.4 Galling initiation model

Before an asperity grows in size according to the lump growth model (section 3.5) it needs to be determined if the asperity is initiated for galling, and therefore lump growth. A criterion needs to be set to check whether the composition of the asperity in combination with the input parameters of the process is suited to be initiated. First, the galling initiation model developed for cold forming will be briefly treated. Then, the galling initiation for hot forming situations will be discussed. Here, two possibilities will be proposed with an initial comparison. From these two initiation models for hot forming, one will be chosen based on empirical validation, see section 7.

3.4.1 Cold forming

In cold forming the galling initiation has been described by van der Heide [2, 56]. It is proposed that galling will be initiated when direct contact between the tool and the workpiece material occurs. This direct contact is caused by local lack of lubricant, lubricant failure. This is formulated as the flash temperature initiation model, which is shown in the equation below.

$$T_c = T_b + T_f \geq T_{crit} \tag{3.20}$$

where T_c the contact temperature, T_b the bulk temperature, T_f the flash temperature, which is the local temperature rise, and T_{crit} is the critical temperature of the lubricant at which it will fail. The local rise in temperature depends on the heat generated by friction and on the thermal conductivity of the material. It is assumed that material transfer only occurs when an asperity is in the wedge regime. This is because ploughing does not show material loss and can therefore not accommodate material transfer. Also, no material transfer can occur in the cutting regime according to its definition, because the removed material is in the shape of long chips, which are not likely to adhere due to its size [2].

3.4.2 Hot forming

The cold forming model for galling initiation can not be copied exactly for hot forming, because the temperature condition, concerning the lubricant, is removed in hot forming. Currently, no lubrication is available that is stable for these elevated temperatures. As stated before, two models for the initiation of galling for a single asperity will be proposed. First, an existing approach based on the fracture of the coating proposed by Nesselaar [17], which has been developed using TriMM (stand-alone software package used at the University of Twente). This software provided low values for the shear factor (f_C), which prohibited adopting the wedge regime assumption. Therefore, this model completely deviates from the cold forming model and uses the fracture of the coating as a mechanical initiation mechanism (Coating fracture initiation - CFI). Second, a proposition based on the wedge regime of the wear mode diagram is introduced, because the TriboForm Solver does provide suitable values for the shear factor, which allows for the adoption of the wedge regime assumption. This model is similar to the cold forming initiation for galling, because it uses the assumption that only asperities within the wedge regime contribute to galling (Wedge formation initiation - WFI).

Initiation based on coating fracture

Cracks in the coating is observed using optical microscopy [17, 57]. Such a crack can indicate the location at which particles start to wear of from the coating. Therefore, fracture toughness is proposed as a mechanical initiation mechanism for galling in hot forming processes [17]. The plane strain condition is used because the cracks are relative small compared to the thickness of the workpiece. From the three modes of crack surface displacement, seen in figure 3.8, only the first mode is used, which is described by the plane strain fracture toughness (K_{Ic}) in equation 3.21. Only mode I is used because the stresses are perpendicular to the length and width of the crack [17]. Note, that this condition only holds for a brittle fracture.

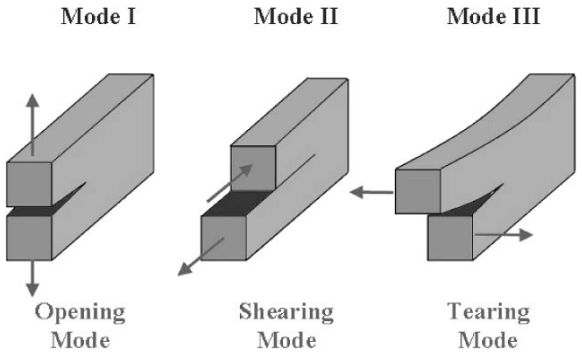

Figure 3.8: Three different modes of crack loading.

$$K_{Ic} = Y\sigma_c\sqrt{\pi a} \tag{3.21}$$

Where σ_c the critical stress for crack propagation, Y the dimensionless geometry parameter, which depends on both crack and specimen sizes and geometries as well as the manner of load application, and a the crack length [58]. The value for the plane strain fracture toughness for Fe-Al intermetallic compound layers has been examined by Kyokuta [10], see table 3.2. The value proposed by Nesselaar based on the values found by Kyokuta will be adopted in this model, $K_{IC} = 0.25$ MPa/$\sqrt{m}$. A sensitivity study on the fracture toughness will be performed, see section 6.1.3.

Compound layer	K_{IC} [MPa/$\sqrt{m}$]
FeAl	1.1
Fe_2Al_5 fine grained	0.51
Fe_2Al_5 coarse grained	0.26

Table 3.2: Plane strain fracture toughness [10].

To check whether a single asperity is able to initiate lump growth for galling the equation below is used. The equation states that if the stress intensity factor (K_I) of the single asperity in question exceeds the plane strain fracture toughness of the coating layer that the asperity will initiate fracture.

$$K_I \geq K_{IC} \tag{3.22}$$

$$K_I = Y\tau\sqrt{\pi a} \tag{3.23}$$

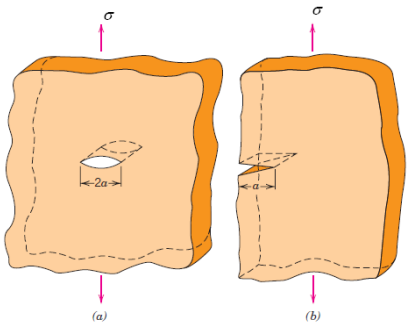

Figure 3.9: Schematic representation of a) an interior crack in a plate of infinite width and b) an edge crack in a plate with a semi-infinite width [58].

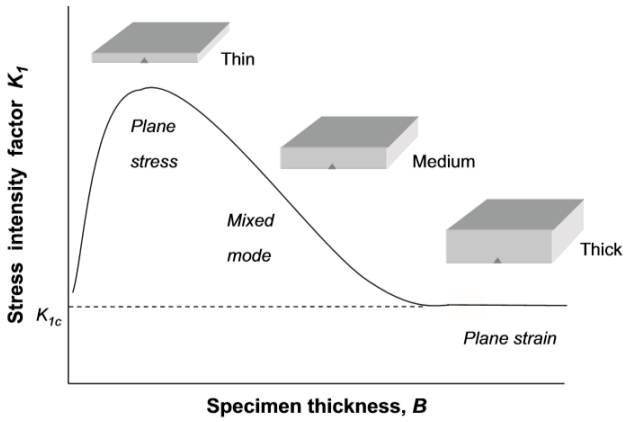

Figure 3.10: Schematic diagram showing the variation of the measured stress intensity factor K_I as a function of specimen thickness B [59].

Where τ is the shear strength at the crack tip, see equation 3.24, and a the crack length, which is assumed to be equal to the coating thickness, $a = 40\mu m$ [17]. The dimensionless geometry parameter (Y) is assumed to be $Y = 1.12$ [17]. This assumption is in line with the general values for planar specimens with cracks much shorter than the width of a specimen; where a through-thickness crack is $Y = 1.0$ and an edge crack is $Y \cong 1.1$ [58], see figure 3.9 for a schematic representation.

$$\tau_{crack} = \mu_{asp} H_{\text{eff}} \tag{3.24}$$

In figure 3.10 the relation between K_{IC} and the thickness of the specimen is shown. One of the assumptions for the described initiation model for hot forming states that the plane strain fracture toughness condition will be used. A crack, which is assumed the length of the coating thickness is relative small compared to the strip thickness (1.5mm) and therefore this can be used.

Initiation based on wedging regime

The values for the shear factor are different in TriMM compared to TriboForm, which are $f_C = 0.17-0.37$ and $f_C = 0.71-0.80$ respectively. The higher values of the shear factor make it possible to adopt the wedge regime assumption from the cold forming model. A single asperity will be initiated when it is within the wedging regime according to the wear mode diagram [36, 37] shown in figure 2.9. The wear modes are developed for cold forming and are now assumed for hot forming conditions. Also, as mentioned before, these modes are develop on a 2D slip-line field assuming plane strain deformation and ideal plastic behavior. The condition for an asperity to initiate for galling, based on the wedge regime, is given in equation 3.25.

$$\text{Wedging if} \begin{cases} \theta_{asp} > 0.5 \arccos f_C \\ \theta_{asp} < 0.25(\pi - \arccos f_C) \end{cases} \tag{3.25}$$

3.5 Lump growth model

Using the previous described models the lump growth model can be addressed [4]. This model has been developed for cold forming and will be applied for hot forming. In figure 3.11 an overview of the steps within lump growth are shown. But first, the elliptical paraboloid asperity is converted into a hexagon polyhedron. This is an input for the lump growth and can be seen in the diagram of figure 2.1. First, the separation height is needed to know which tool asperities are in contact and what their penetration is into the softer counter surface. Using the polyhedron geometry, the material transfer from the sheet to the tool will be determined. This is done in two steps: 1) Determine transferred volume and 2) Determine deposit layer. Then the stability is evaluated, because the material that is able to transfer only adheres when the asperity can hold the forces during sliding: 1) Determine stresses within the asperity and 2) evaluate stability cases. Finally, the adhered layer, according to one of the stability cases in the step before, is included in the new dimensions of the asperity. This cycle is repeated, which leads to multiple extra layers on the initial asperity, called growth of the asperity. The next section will discuss the multi asperity growth scenarios.

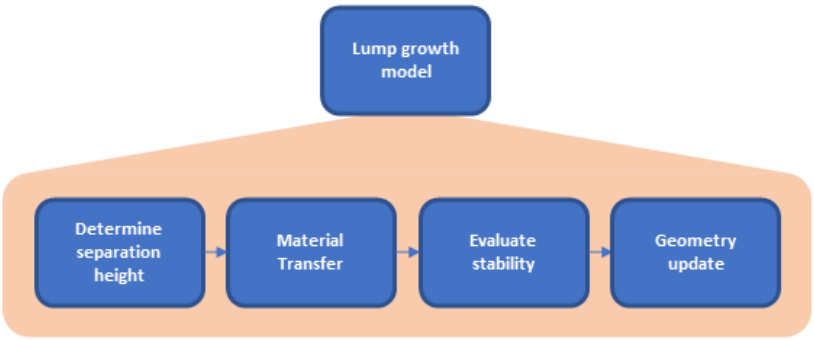

Figure 3.11: Diagram breaking down the steps for lump growth.

3.5.1 Hexagon based polyhedron asperity

The geometry of the asperity needs to be changed from an elliptical paraboloid to a hexagon based polyhedron [4, 60]. This change is to use a simpler shape for the lump growth and to determine the mechanical stability of the growing asperity due to the ploughing forces acting on it in an easier way. Figure 3.12 shows the hexagon base within the elliptical base. The hexagon has the following properties, 1) BF and CE are equal in length and parallel to each other and also parallel to the sliding direction (positive x-direction), 2) BC and EF are equal in length and parallel, 3) point A and D are on the y-extremes and 4) point C and F (or B and E) are on the x-extremes. The conversion from the elliptical paraboloid asperity to the hexagon based polyhedron can be found in appendix A.2.

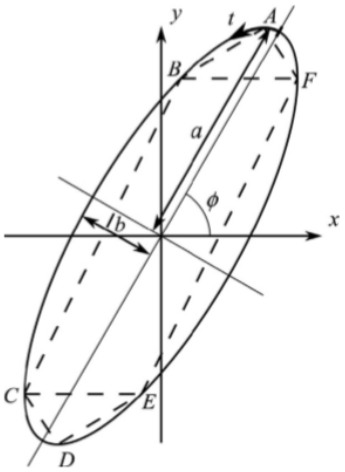

Figure 3.12: Hexagon base within the elliptic base of the asperity. [60].

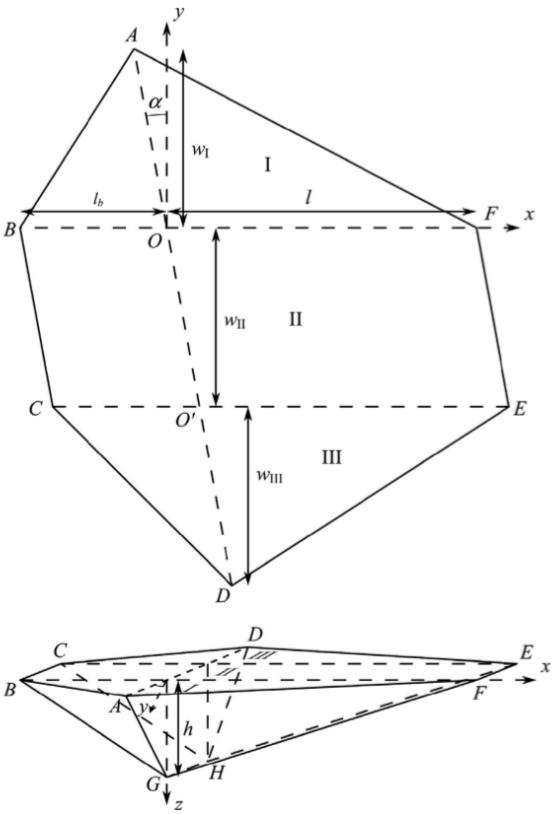

Figure 3.13: Dimensions of the hexagon base of the lump [60]. *Dimensions are different from asperity ($l_b \neq l$).*

The hexagon base describe above is smaller than the ellipse it is based on and therefore the hexagon should be scaled up. This is done by scaling the triangles (ABF and CDE) proportionally and the parallelogram (BFEC) only in the x-direction, see equation A.11 and equation A.12 for the scaling factor and the scaled height respectively.

It is possible for the hexagon base to reduce to a quadrilateral base when the minor and major radius of the ellipse are equal, when the orientation $\phi = 0$ or when the orientation $\phi = 0.5\pi$. The hexagon can have multiple different shapes based on the same ellipse due to the orientation, which is shown in figure 3.14.

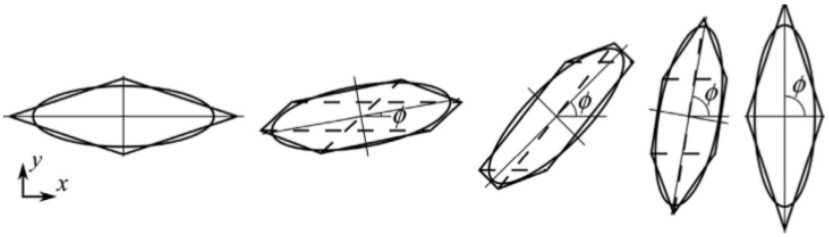

Figure 3.14: An ellipse with a hexagon fit for different orientations (ϕ) [4].

3.5.2 Determine separation height

The initial separation height, the distance between the tool surface and the mean plane of the rough workpiece (d_L), is determined in the contact model [24], see figure 3.5 for the visual representation of the separation height. In the contact model the fractional real contact area (α) and the separation height are solved for simultaneously, which makes the fractional real contact area an important factor in the determination of the separation height. Depending on the normal pressure the shape, size and amount of asperities can be different, which is schematically shown in figure 3.15. The separation height needs to be recalculated each time a sliding step occurs, which will be elaborated on in the next section on multi asperity lump growth (section 3.6).

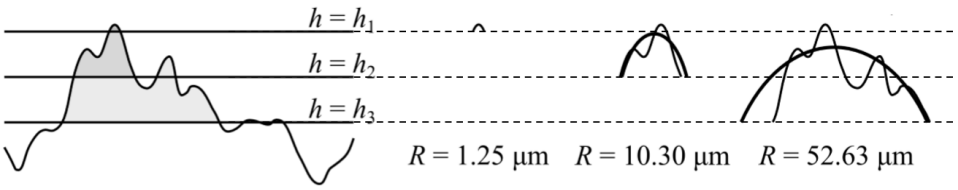

Figure 3.15: Different asperity definitions with their separation height for different loading cases. *R is the radius for each asperity definition.* Adapted from [4].

3.5.3 Material transfer

Determine transferred volume

Using the established hexagon based polyhedron geometry of the asperity, the volume that will adhere to the tool, transfer volume, can be determined [4]. It is assumed that material transfer only takes place for asperities within the wedge formation regime according to the wear mode diagram in figure 3.7, which is valid for cold forming conditions. During a sliding contact material from the relative softer sheet material will be worn of, but just a part of this worn volume will be transferred to the relative hard tool asperities. This introduces the factor m as show in the equation below.

$$V_{\text{trans}} = mV_{\text{wear}} \tag{3.26}$$

In which V_{wear} is the worn of material and V_{trans} is the part of the worn material that will actually be transferred tot the tool surface. This worn volume (V_{wear}) is calculated using the general expression of the Archard wear model. The theory of Archard shows that the wear rate (k_w) is independent of the apparent contact area and that it is directly proportional to the applied load (F_n),

which leads to the following relation [44, 49].

$$k_w = \frac{V_{\text{wear}}}{l_{\text{slide}} F_n} \tag{3.27}$$

with k_w the wear rate in the wedge regime [36] shown in equation 3.28, l_{slide} the sliding length and F_n the normal force over half the area of the hexagon based asperity.

$$k_w = \frac{1}{2k} \frac{\sin^2\theta + \frac{1}{2}\sin 2\theta}{1 + \sin(2\theta)} \tag{3.28}$$

$$k = 0.18H \tag{3.29}$$

with k the shear strength of the material and θ the attack angle of the asperity, which can be calculated by taking the arc-tangent of the asperity length (l) over the asperity height (h) for the hexagon based polyhedron shape. As stated before not all the volume that will be worn of is actually transferred to the tool. In the thesis of de Rooij this is expressed [5]:

$$\frac{\Delta s}{l_{slide}} = m\frac{F_n k_w}{A} \quad \rightarrow \quad \Delta s = m l_{slide} \frac{F_n k_w}{A} \tag{3.30}$$

Where Δs is the height increase, A the area of a circle since a spherical asperity is assumed and a certain fraction m. It is assumed that this fraction is proportional to the adhesion force [5, 61]. This is done by substituting $m \cdot l_{slide}$ in the way indicated by the equation below.

$$m l_{slide} = m_1 = m_2 F_a$$

Where m_1 and m_2 still function as the fraction and F_a is the adhesion force. In the thesis of de Rooij the adhered volume only causes the (spherical) asperity to grow in height, but the distribution of adhered volume will be described differently, see section 3.5.4. Also, the adhesion force is calculated using relations for a sphere in contact with a flat plane. That is not valid for this case (polyhedron) and therefore another relation needs to be found [4]. It is assumed that the contact between the asperity and the plastic material can be approached as a summation of multiple flat-on-flat contacts. The van der Waals interaction energy relation (work of adhesion per unit area) of the flat-on-flat contact is shown in equation 3.31 and the surface energy can be approximated using equation 3.32 [62].

$$W_{body-body} = -\frac{A_H}{12\pi D^2} \tag{3.31}$$

$$\gamma = \frac{A_H}{24\pi D_0^2} \tag{3.32}$$

with A_H the Hamaker constant, D the separation between the two bodies, D_0 the separation between two bodies in contact at the atomic scale and γ the surface energy. This shows that the surface energy equals half the energy needed to separate two flat surfaces. Relating this van der Waals interaction energy to the adhesion force (F_a) is done by taking the derivative of W.

$$\frac{F_a}{A} = \frac{dW}{dD} = \frac{A_H}{6\pi D^3} = \frac{-2}{D} W \tag{3.33}$$

Then relating this equation to the surface energy is done by substituting A_H from equation 3.32 into equation 3.33 which becomes the equation below.

$$\frac{F_a}{A} = 4\gamma \frac{D_0^2}{D^3} \tag{3.34}$$

From this equation it follows that the adhesion force (F_a) is proportional to the surface energy (γ). This relation is based on the Van der Waals interaction whilst, based on the separation, the metallic bonding will be dominant in the model. In both cases the F_a is proportional to γ and decreases very fast as a function of separation. Therefore, it is assumed that the volume of the deposited material is proportional to the adhesion energy multiplied by the size of the contact area. This gives the following relation according to van der Linde [4].

$$V_{trans} = mV_{wear} = c_{fr}\Delta\gamma l_{slide} k_w F_n \tag{3.35}$$

where c_{fr} is a constant calibration parameter and $\Delta\gamma$ the adhesion energy. In the thesis of van der Linde [4] the fixed value for the adhesion energy ($\Delta\gamma \approx 2.4 J/m^2$ for iron [50]) is used in cold forming conditions. However, as stated before, the value for adhesion energy changes over temperature [45], see figure 2.12. The model in this report will not use $\Delta\gamma$ directly, but its temperature dependant behavior will be included by making the calibration factor m a function of temperature, see section 5.

Determine deposit layer

The transfer volume determined in the step above will be distributed over the frontal part of the asperity [4]. Here, the sliding length is assumed to be the same over the whole asperity, the attack angle (θ) is assumed to be the same on every y-coordinate within the asperity for a cross-section parallel to the xz-plane and the contact pressure is assumed to be constant in ideal plastic contact behavior. Due to these assumptions, the thickness of the transfer layer is considered constant in the z-direction. However, this causes only growth in height while the edges are neglected. In figure 3.16 the deposit layer is shown in gray and the neglected edges are indicated with the dotted areas.

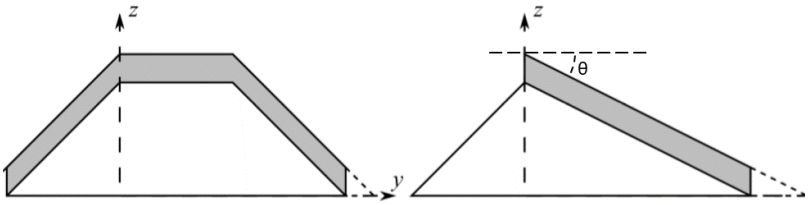

Figure 3.16: Schematic overview of asperity with deposit layer on the contact face. *left* cross section front view, *right* cross section side view [4].

The material needs to be redistributed to include the edges, where a constant thickness in the z-direction will be applied. The redistribution of the material is calculated by using the volume of the frontal part of the asperity and the transfer volume. The transfer volume is the difference between the initial with the new shape of the frontal part of the asperity, which is shown in the equation 3.36. The volume of the frontal part of an asperity is calculated using equation 3.37.

$$\Delta V = V_{new} - V_{old} \tag{3.36}$$

$$V = \frac{hl}{6}(w_I + 3w_{II} + w_{III}) \tag{3.37}$$

The new volume of the frontal part of the asperity uses the same relation shown in equation 3.37, but needs to be scaled to comply to the relation in equation 3.36. Again, the triangles are scaled proportionally and the parallelogram only in the x-direction, but only for the frontal part of the asperity.

3.5.4 Evaluate stability

Determine stresses within asperity

The deposit layer described in the previous section is not the final adhered layer of material, because it is probably mechanically not a stable situation [4]. The asperity with its transfer layer need to be checked whether it can sustain the mechanical forces during contact. Only, when this is satisfied material is able to permanently adhere to the asperity. So first, the forces in x- and y-direction on the hexagon base are determined based on force equilibrium. Both directions need to be calculated because the asperity shape does not show symmetry. These forces are used to get the tangential stresses, which are used as a fail criterion. In this case the fail criterion is the norm of the sum of the shear stresses. In appendix A.3 the forces in x- and y-direction are derived [4].

Using the forces in x- and y-direction the tangential stresses are determined, see equations 3.38.

$$\tau_{xy} = \frac{F_x}{A}, \qquad \tau_{xz} = \frac{F_y}{A} \tag{3.38}$$

with

$$A = (l + l_b)\left(\frac{1}{2}w_I + w_{II} + \frac{1}{2}w_{III}\right) \tag{3.39}$$

where A is the area of $ABCDEF$, according to figure 3.13. However, using the complete base area of the asperity can lead to an underestimation of the tangential stresses, because the plastic forces are not supported by the full connection area to the bulk material. Therefore, the value l_b in the asperity geometry will be replaced by the ch for the lump dimensions, where c is a constant value of 2 based on FEM simulations [4]. Using a hexagon based asperity causes that no symmetry can be used in the fail criterion. Therefore, the fail criterion will be the norm of the sum of both stress vectors, see equation 3.40.

$$\tau = \sqrt{\tau_x^2 + \tau_y^2} \tag{3.40}$$

Evaluate stability cases

An asperity can only grow in size when it is strong enough to withstand the plastic forces acting on it. The growth of the asperity is also called lump growth. This lump uses the same starting dimensions as the asperity except for the value of l_b, which will be shortened to ch. Other assumptions for stable lump growth are:

- The material strength is taken to be equal to the strength of the deposited layer.
- If the stability criteria is not met, because an asperity is too steep, it is still assumed that the asperity is strong enough, because, in general, the tool material is harder than the sheet material. This causes unlimited growth of an asperity.
- The dimensions of the asperity (and lump layer) can not be smaller than the dimension before material deposition.
- The rear side of the deposit layer is not exactly vertical. It crumbles of to a slope equal to $\Delta z/\Delta x \approx 0.5$.

Using the assumptions mentioned above the amount of material that will actually be deposited is determined [4]. It is possible that the added layer, new lump dimensions, are not able to withstand the plastic stresses. Therefore, two extremes are distinguished. The most stable one (Case A) where h, w_I, and w_{III} remain equal to their previous value and where only l grows in size and the least stable one (Case B) where a layer of equal thickness will be put onto the existing lump. In this latter

case the slope will be equal to the previous iteration. When neither of these two options applies the new layer will get a slope between these two extreme cases (Case C). The dimensions of each case is summarised in table A.1 and the next section will provide a visual representation of the lump growth using the stability cases. The sequence in which the cases are assessed is stated below and also shown in a flowchart in figure 3.17.

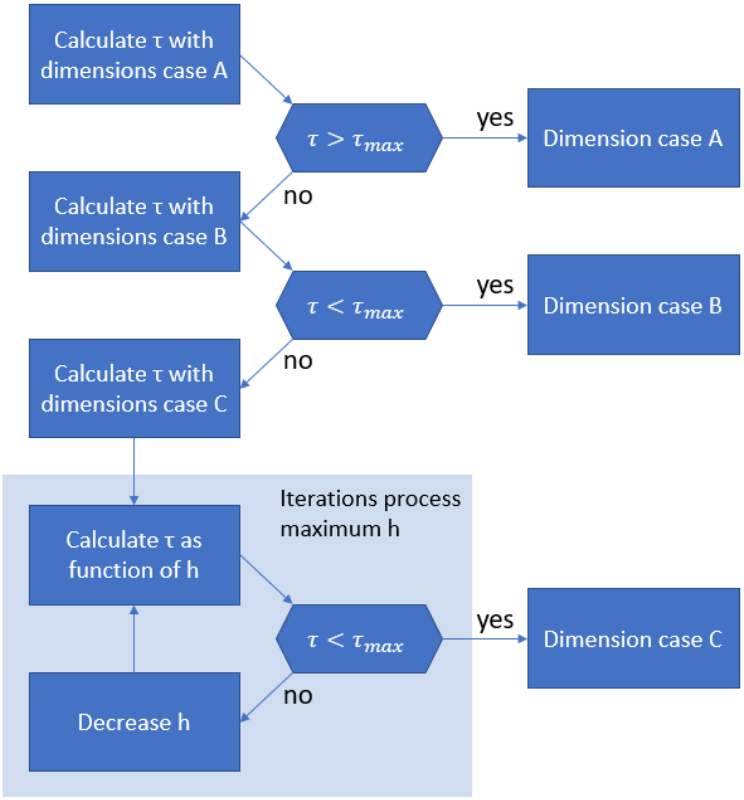

Figure 3.17: Flowchart to determine dimensions of next deposit layer. Adapted from [39].

- **Case A** This is the most stable growth situation, cause the asperity only increases in length. Only the base area of the lump increases and therefore it increases the stresses the asperity can handle. The asperity grows in length if the stresses at the interface of the lump are above the strength of the deposit layer.
- **Case B** This is the least stable growth case. The rear side of the deposit layer crumbles of causing l_b to grow by a small amount and h, l, w_I and w_{III} to decrease by a small amount. If the shear stresses are below the maximum shear stress at the interface, the asperity is capable of resisting the mechanical forces due to ploughing.
- **Case C** When the two cases above do not apply, an iterative process based on h is used to determine the final dimensions of the new lump. This is done by assessing the maximum h and gradually decreasing the height until the shear stresses at the interface are below the maximum shear stress.

3.5.5 Update geometry

In figure 3.18 the growth of an asperity with two different orientations is shown using the parameters from table A.2, taken from [4]. In figure 3.18a the difference between the asperity geometry

and lump geometry can be clearly seen. The value for l_b has been changed, because the stresses are not supported by the full interfacial area of the asperity. The growth cases explained in the previous section are visualized. In both sub-figures the first growth layer is according to case A, which indicates that the interfacial area could not hold the stresses for an asperity when growing in height. The next growth layer in both asperity orientations is according to case C. The layer in figure 3.18a looks like case A, but is in fact case C. The growth of the other layers is for both figures all according to case C. The layers look like stability case B, because the slope seems to match that of the previous layer. However, a small difference is present, which can not be clearly seen with the eye.

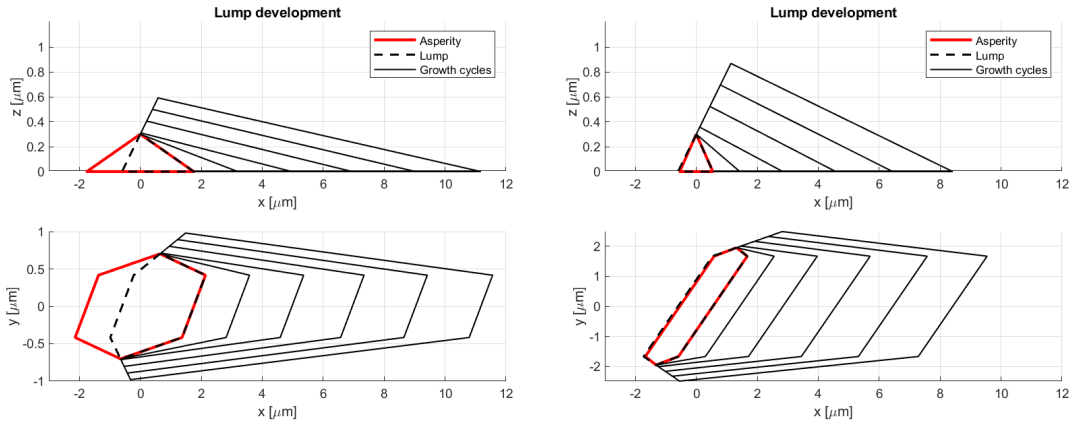

(a) $\phi = 10°$. (b) $\phi = 45°$.

Figure 3.18: Single asperity lump growth with different orientations using the dimensions of table A.2.

3.6 Multi asperity lump growth

In the previous section the growth of a single asperity is treated. Here, the effect of multiple asperities on a surface area is discussed, because the roughness of the surface causes there to be multiple asperities in contact. This will be elaborated on for two situations, which serve a different purpose in analyzing the lump growth. In both these cases there is no interaction between the single asperities.

The first situation of multi asperity lump growth updates the surface for a new sliding step, by changing the separation height (d), using force equilibrium [4]. The second situation changes the tool topography for each sliding step. The tool topography update allows the cycle to recalculate the COF and, therefore, evaluate the change of COF over sliding length. The first situation, of these two, will be applied in the TriboForm Analyzer for the verification case later in section 7. The situation based on updating the tool topography cannot be applied in the TriboForm Analyzer, because the AutoForm simulation, which serves as input, does not support sliding length over multiple cycles. The workflow for the validation of galling in the TriboForm Analyzer will be addressed in section 7.1.

What holds for both approaches is the relation in equation 3.41. This relation accounts for the fact that a tool asperity is not in contact with the sheet the whole time during sliding, because it only is in contact with the flattened plateaus. Since the fraction of contact area is described by

α_{meso} this value is used to scale the sliding length to an average sliding length for each asperity.

$$l_{slide} = \alpha_{meso} l_{slide} \tag{3.41}$$

3.6.1 Update based on the separation height

In this multi asperity lump growth model the model will be updated after each sliding step (cycle) using force equilibrium on micro level. This update cycle is visualized in figure 3.19 with the dotted arrow and the text ***# sliding steps***. Here, the approach will be explained in more detail. In section 6 *Results* the evolution of the amount of asperities over sliding length will be shown to visualize how the model deals with this multi asperity lump growth approach.

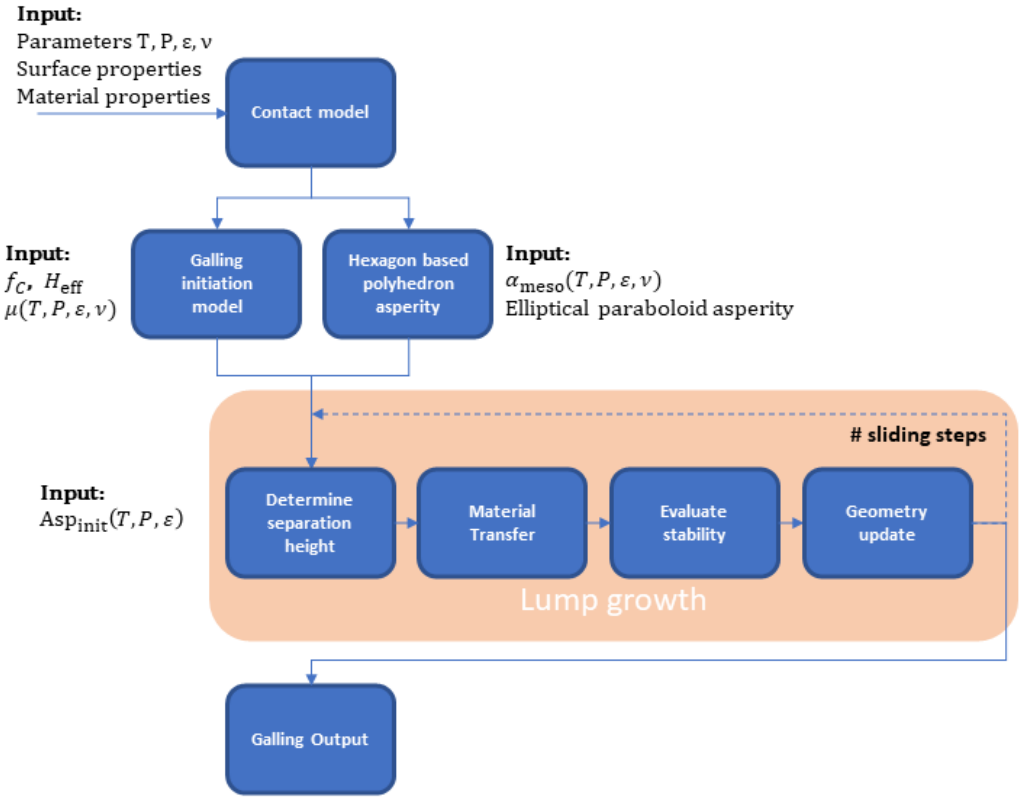

Figure 3.19: Diagram with the approach to galling in hot forming. Featured with lump growth for multi asperity growth using separation height.

The contact at micro level is between the tool asperities and the sheet plateaus. In order to calculate the new separation height, the force equilibrium condition needs to be met [4]. This is done by evaluating the normal pressure, since the hardness and real fractional contact area from equation 2.2, remain constant for a parameter set. The normal pressure (F_n) over the surface should be equal to sum om the normal force of the asperities (F_{ni}) in contact, see equation 3.42.

$$F_n = \sum_i F_{ni} \tag{3.42}$$

The size of the asperities grows during the lump growth, which changes its area compared to the contact area of the initial separation height. The separation height is the only unknown and is recalculated using an implicit relation to maintain force equilibrium. The new separation

height is found when the summation of the contact area of only the frontal part of the asperities matches the original real contact area. This can cause an asperity to fall out of contact, which means that the area is carried by less asperities than the step before. This can, eventually, also lead to one asperity carrying the total contact, because only growth is considered. A diagram with a schematic overview of this multi asperity situation is given in figure 3.19. This diagram shows a more extensive representation of the lump growth model compared to figure 3.11. It shows with the use of a dashed arrow that the lump growth steps, which are also shown in figure 3.11, repeats after each sliding sliding step until the total number of steps has been reached.

3.6.2 Update based on changing the tool topography

Here, the lump growth for multi asperity situation by changing the tool topography for each sliding step will be explained. This means that the COF will be updated for each sliding step, while the previous multi asperity growth only uses the the COF calculated in the contact model before lump growth takes place. The update cycle is visualized in figure 3.20 with the red dotted arrow and the text ***# sliding steps***. This section will explain the approach in which the tool topography will be updated to get an updated COF. In section 6.4 the effect of updating the tool surface with respect to the coefficient of friction will be shown.

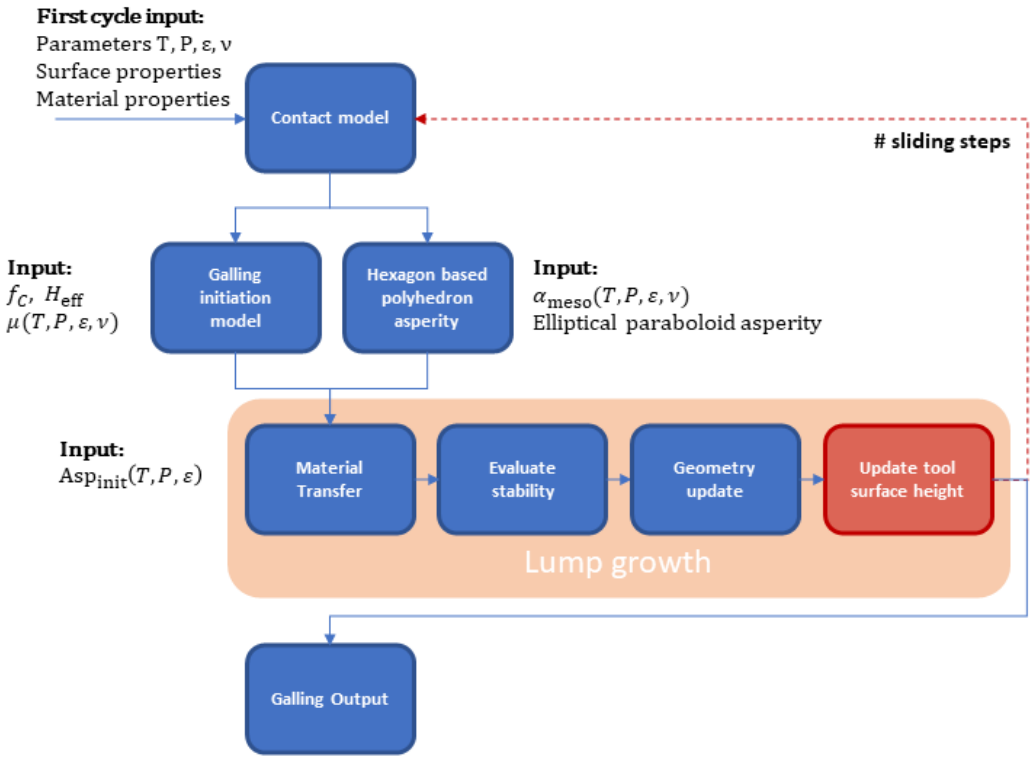

Figure 3.20: Diagram with the approach to galling in hot forming. Featured with lump growth for multi asperity growth using the updated tool surface height.

Each sliding step will go through the contact model and the lump growth model, but in this case the tool will be updated by applying the adhered volume over the asperity pixels. The second sliding step starts with sending the updated tool topography through the contact model, which recalculates the contact patches and the COF. Then the updated values are used to determine the adhered volume of the second sliding step, which will be applied to the tool topography again.

This process is schematically shown in figure 3.20, where the changes relative to the previous multi asperity approach are colored red. Due to the inclusion of the contact model, which recalculates the contact and the friction, in the evaluation of the sliding steps the process time is increased. The box with '*Update tool surface height*' has been added, because an extra step is introduced after the geometry update. The new asperity dimensions are used to update the matrix for the tool topography, which serves as the new input for the tool topography in the contact model. The red dashed arrow indicates the next sliding step, which goes from the lump growth to the contact model after each sliding step. Therefore, the contact area, elliptical paraboloid asperities and COF are recalculated, which also means that the galling initiation model determines a new set of galling initiated asperities. Also, note that the box '*Determine separation height*' is omitted, because the separation height will be calculated along with the contact area for each sliding step.

The tool topography is updated by evenly distributing the adhered volume of an asperity over the pixels of the front part of the asperity. This will be explained by using a single asperity as an example. In figure 3.21a the pixels that make up an asperity are marked grey. Only half of the pixels, which make up the front of an asperity, are used when material is added to the tool surface, see figure 3.21b. The front part of the asperity is used because that is in line with the way volume is deposited in the lump growth model (section 3.5.3). In the situation presented in figure 3.21b the asperity will only grow in height, but an asperity also grows in length. The growth in length is included by shifting the volume deposit on the pixels with the rounded amount of pixel-length (P_{shift}) that fits in the new calculated length of the asperity, see equation 3.43. A visual example with a pixel-shift of one is given in figure 3.21c.

$$P_{\text{shift}} = \text{round}\left(\frac{l_{\text{new}}}{l_{\text{pixel}}}\right) \tag{3.43}$$

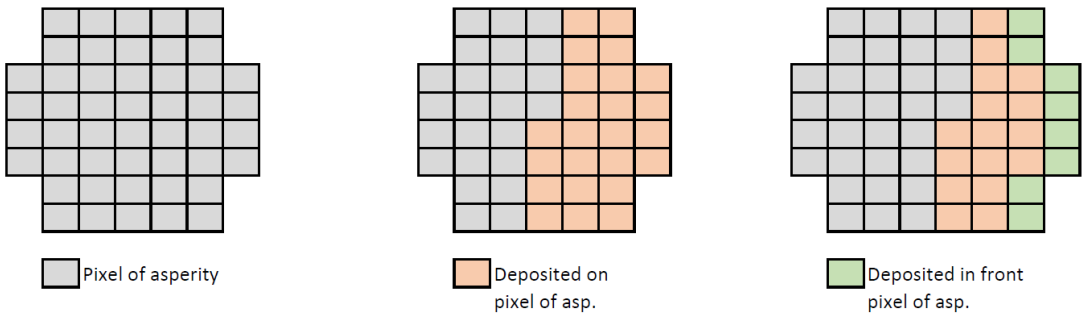

(a) Pixels of asperity.

(b) Volume deposited on asperity growing in height.

(c) Volume deposited on asperity growing in height and length.

Figure 3.21: Topography update for a single asperity.

4 Hot strip draw experiments

4.1 Experimental setup

A hot strip draw test is performed at Tata Steel [3] to simulate the conditions of a hot stamping process [17, 3]. The experiment is used to gather information on the adhered material from the workpiece (substrate) to the tool. The furnace used at Tata Steel can be seen in figure 4.1 and an overview of the strip draw test is given in figure 4.2. In a strip draw test the sheet (test material) is drawn between two tools while applying a defined normal load on the tools.

Figure 4.1: Experimental setup.

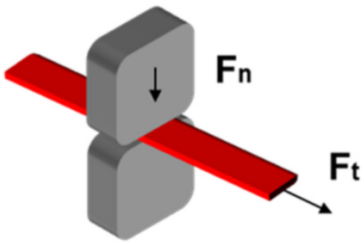

Figure 4.2: Schematic overview strip draw test.

The workpiece material, or in this case the strip, will be an Al-Si coated Press Hardening Steel (PHS). Further information on the strip is given in table 4.1. The tools are rectangular and are given a milled finish. The drawing direction will be perpendicular to the milling direction on the tool surface. Other properties of the tools can be found in table 4.1.

The strip will be heated to 930°C and stay there for 6 minutes to ensure full austenization of the material, the austenization temperature is at 850°C . Keeping the strip at elevated temperatures changes the morphology and topology of the coating due to diffusion. After the preparation of the material it is transferred to the strip draw setup. The strip will cool to the desired test temperature, which is monitored by a pyrometer. When the desired temperature is reached the strip will be clamped in position and the strip draw will start. Multiple draws on the same part are performed with an interval of 8 minutes between the experiments. Details on the test conditions are found in table 4.2.

Furnace		**Strip**		**Tool**	
Furnace	Roller hearth	Substrate	PHS	Material	DIN 1.2344
Temp	930°C	Coating	Al-Si (7-11% Si)	Finish	Milled
Time	6 min	$R_{a\parallel}$	0.15 μm	Hardness	48 $\pm$2 HRC
		$R_{a\perp}$	0.04 μm	S_a	0.20 $\pm$0.05 μm
		Dimensions	800 x 50 x 1.5 mm	Dimensions	90 x 11 mm
		S_a*	1.9 μm		

Table 4.1: Test parameters friction draw test. **after heat treatment.*

The topography of the strip draw tests have been measured using two different techniques. A line profile roughness measurement and a 3D optical confocal measurement using a Mahr PKG120 (cut-off 0.8mm), and the nanofocus μsurf mobile respectively.

Test conditions	
Contact Area	50mm (strip) x 11mm (tool)
Interval between exp.	8 minutes
Nominal pressure	2.5 and 5.0 MPa
Nr of draws	10 (1-5-10)
Sliding length	200 mm
Sliding velocity	100 mm/s
Temperature	450°C - 750°C (intervals of 50°C)

Table 4.2: Test conditions friction draw test.

A schematic overview of the measurement techniques with respect to the tool surface is given in figure 4.3. The 2D line measurement is performed on the upper tool at two lines. The two different lines are denoted with 'a' and 'b'. These line measurements contain worn as well as unworn parts of the tool surface. The confocal images provide a 3D height distribution of the tool surface. The images are limited to a small area (6 x 3.5mm). The confocal images are taken of the spots on the surface which show the greatest amount of wear and therefore the exact location can vary.

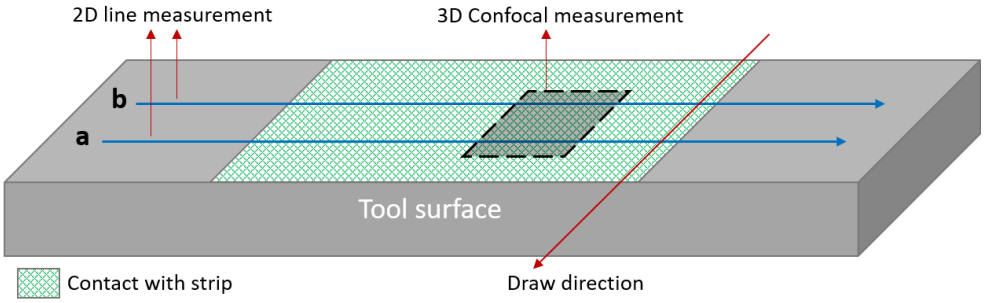

Figure 4.3: Schematic overview of both measurement techniques and its intersection.

4.2 Data processing

The goal of these experiments is to acquire information on the adhered area and volume of the line measurement and confocal measurement respectively. The 2D and 3D measurements are both on the upper tool and have an overlap at a certain point, see figure 4.3 for a schematic overview. Note, the pressure during experiments on *line b* was greater than on *line a* due to an alignment error [17].

The two measurement types are used in combination to get an adhered volume. The line measurements are used to find a reference height, because these measurements contain the worn and unworn part of a tool, figure 4.4a. Above the reference is the adhered area and below the reference is the abraded area. The confocal measurements are confined to a small area on the tool, figure 4.4b, which is not able to get such a reference on its own. The confocal image is shown in figure 4.5 with the matched line measurements. The height profile of the confocal image is matched to the line measurements, figure 4.4c, to use the 2D reference on the 3D surface to get an adhered volume per area.

First, the 2D line profiles are processed. A moving average filter with a window size of 20 is applied to reduce the noise in the measurement. The line measurement shows a worn and an unworn part. In figure 4.4 the line measurement is given of the situation that will serve as an example for the process (750°C , 5MPa and 10 draws). Using the unworn part a reference for the

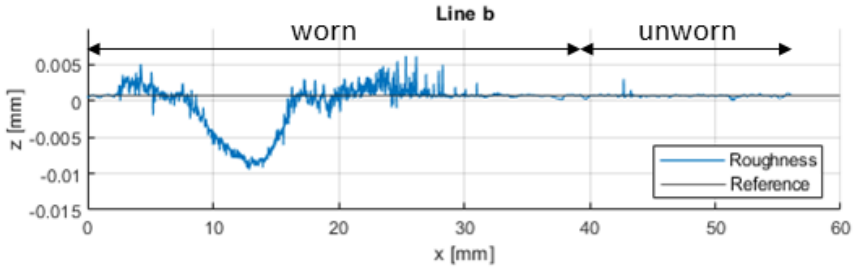

(a) Line measurement showing the assumed worn and unworn part of a measurement.

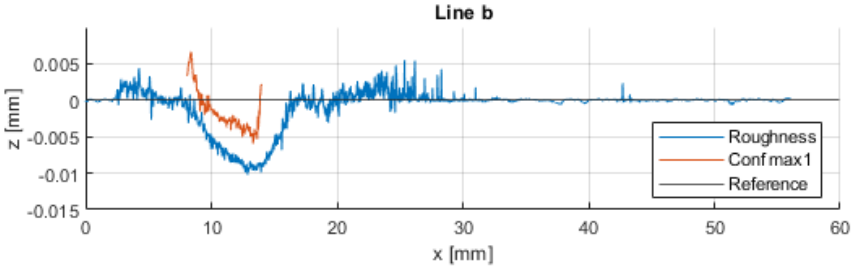

(b) Normalized line measurement with matching confocal measurement for x and y.

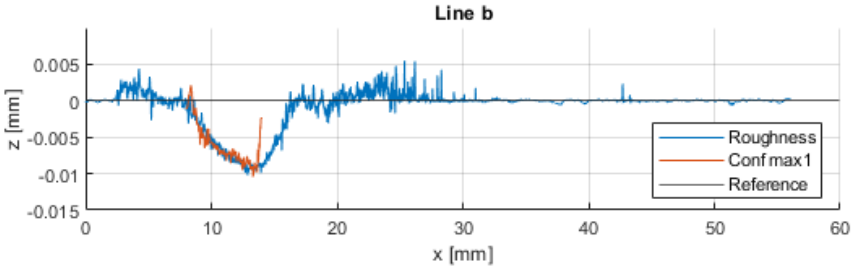

(c) Line measurement with matching confocal measurement for x,y and z.

Figure 4.4: Experiment at 750°C with 5MPa and 10 draws. *Position:* y_{row} = 2.0922mm, z_{shift} = -4.5μm.

whole line measurement is set. The reference is calculated by taking the average of the last 30% of the line measurement. For convenience the line measurement and reference are normalized. Now, all the area above the reference is taken as adhered material and the area below the reference as abraded material.

Then, the confocal images are processed. Again, a moving average filter with a window size of 20 has been applied to reduce the noise in the measurement. The reference from the 2D measurement will be used as a reference for the 3D images. This is done by finding the highest correlation between the two measurements using the *xcorr* function of MATLAB. This provides a location for the intersection of the measurements, with y-coordinate (y_{row}) the row at which the line measurement crosses the confocal image and the x-coordinate the location of the confocal measurement on the line measurement. A correlation plot, shown in figure 4.6, is used to visualize the best match and check if it is a clear match. Also, the correlation plot is used to check if another x-position might compete for the best match. These checks will be supported by a visual inspection for each measurement and can lead to excluding data for further analyses, which will be discussed later in the results section. The z-coordinate (z_{shift}) of the confocal measurement will be adjusted by hand to fit the 2D line measurement. The reference of the line measurement can now also be used

as a reference for the confocal images to get the adhered and abraded volume. All the matched measurements can be found in appendix B.2.

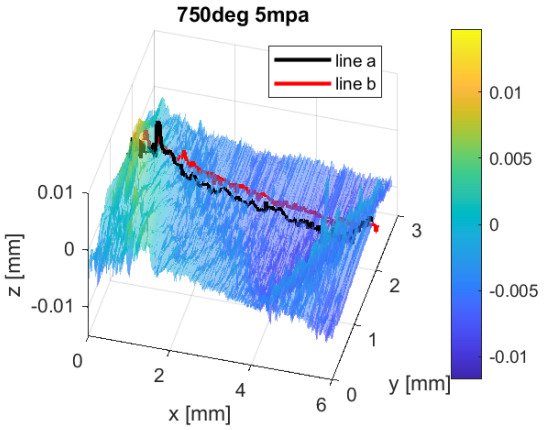

Figure 4.5: Confocal image with matched line measurements (750°C , 5MPa and 10 draws).

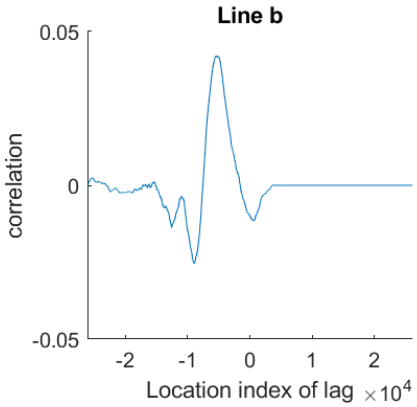

Figure 4.6: Correlation for x-position (750°C , 5MPa and 10 draws).

4.3 Results

The results for different pressures, temperatures and sliding lengths will be discussed and compared. In the appendix the area from the line measurement will be compared to the volume of the confocal measurement to see whether a trend can be established (section B.1). Again, note that the pressure on *line b* was greater than on *line a* due to an alignment error [17]. This leaves room to question the reliability of the results, but this is the available data at this point in time.

Pressure

The provided data has measurements on 2.5MPa and 5MPa to compare results based on pressure. However, the confocal image does not have a clear correlation with the line measurement for the 2.5MPa pressure situations, see appendix section B.2.1 for the corresponding figures. The 2.5MPa measurements are omitted from further use.

Temperature

Here only the 5MPa measurements, which are performed at 450°C , 500°C , 600°C , 700°C and 750°C after 10 draws of 200 mm, are analyzed. In this test series the measurements for 450°C are completely omitted, because no clear correlation is found for line a or line b (figure B.5). Only both line measurements at 750°C (figure B.9) provide a good correlation and for the other temperatures either line a or line b is sufficient. At 700°C an extra data point is available from the sliding length series (figure B.8 and B.12). The figures corresponding to the temperature series can be found in appendix section B.2.2.

The measurements which provide a good correlation are shown in figure 4.7, which shows the adhered volume per unit area. Also, for completeness a figure concerning abraded volume per unit area is shown in figure 4.8. In both these figures bars have been added, indicating the sensitivity of the shift in z-direction. The sensitivity is shown by checking the volume for the situation that the z_{shift} might be $\pm 0.5\ \mu m$.

It can be confidently stated that the Adhered volume increases over temperature until 600°C . At 700°C the adhered volume starts at its dip and at 750°C the adhered volume is likely to be less than that at 500°C . This is explained by including the information on the abraded volume of the tool, because the abraded volume increases over temperature. It should be noted that the figure on the abraded volume of these measurements shows a different order on its vertical axis. The abraded volume is significantly more compared to the adhered volume at higher temperatures. Therefore, the data on adhered volume is influenced by the abraded volume and shows itself as the dip in adhered volume at higher temperatures. The excessive abrasion could be attributed to the alignment error mentioned before.

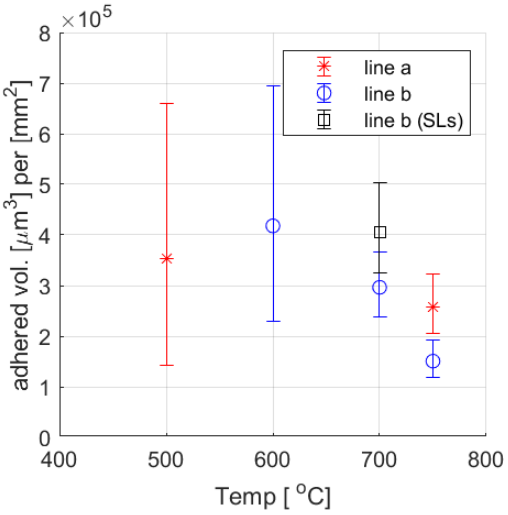

Figure 4.7: Adhered volume over temperature for 10 draws (2m in total).
SLs: Sliding Length series.

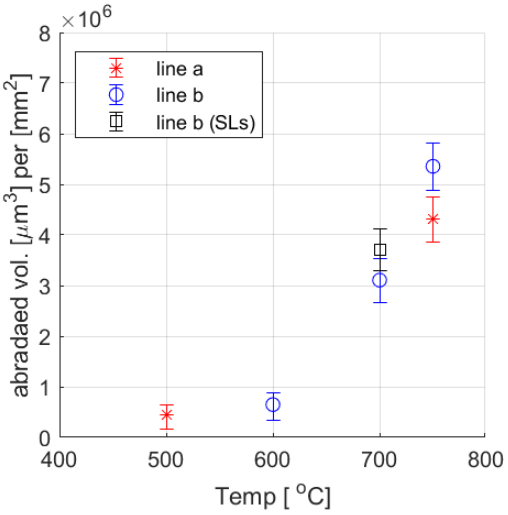

Figure 4.8: Abraded volume over temperature for 10 draws (2m in total).
SLs: Sliding Length series.

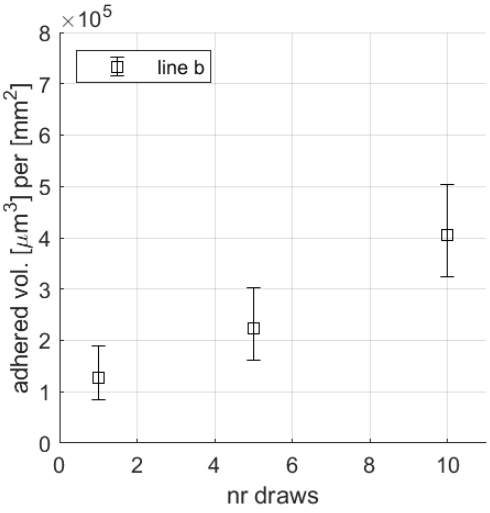

Figure 4.9: Adhered volume over number of draws for 700°C (200 mm per draw).

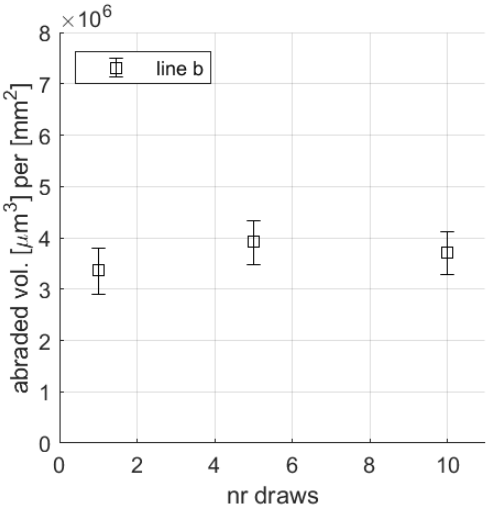

Figure 4.10: Abraded volume over number of draws for 700°C (200 mm per draw).

Sliding Length

The sliding length series has been performed at 700°C for 1, 5 and 10 draws, with each draw having a sliding length of 200mm. Only the line b measurements of each draw situation provide a useful correlation, see figures in appendix section B.2.3. The adhered volume and abraded volume over sliding length is shown in figure 4.9 and figure 4.10 respectively. Again, the bars show the sensitivity of the z-position by checking the volume $\pm 0.5\ \mu m$ its chosen z-position.

When a longer sliding length (more draws) is applied more adhered volume can be observed. Again, an order difference between the adhered volume and abraded volume is present. The abraded volume does not seem to influence the adhered volume in the same way as for the temperature series, because the increase of adhered volume over sliding length is expected. The abraded volume seems to be constant over the number of draws, while an increase might be expected. This could indicate that the adhered/compacted volume compensated the abraded volume to get this constant relation over sliding length. However, the exact impact of the abraded volume and the adhered volume on each other is not known. Also, the sensitivity to the z-position become larger for more draws. This indicates that the match procedure becomes more sensitive and that a larger sliding length is accompanied with more uncertainties.

5 Calibration

The experimental data from the previous section is used for calibration of the lump growth model. The model will be calibrated using the relation between worn volume and transferred volume, which is described in equation 3.35 (section 3.5.3). In this previous section, it is shown that the adhesion force is proportional to the surface energy γ, which leads to the assumption that the transfer volume is proportional to the adhesion energy and contact area. However, a calibration value is still needed to result in the correct transfer volume [4].

Here, the calibration for the volume relation will be done using m instead of c_{fr} using a tool roughness of Sa = 0.6μm. This change is applied, because a constant calibration factor (c_{fr}) multiplied by a fixed adhesion energy ($\Delta\gamma$) is not valid in hot forming. The surface energy is shown to be temperature dependent, figure 2.12, and this effect is included by calibrating m as a function of temperature, see equation 5.1. The experiment in the previous section also varies over pressure and sliding length, which will not be included. Both these parameters are part of the relation to determine the worn volume, see equation 3.27, which is not verified in the experiments. The experiments with a pressure of 2.5MPa do not provide clear results, which leaves the experiments using 5MPa.

$$V_{\text{trans}} = m(T)V_{\text{wear}} \tag{5.1}$$

5.1 Approach

The calibration is done in the following steps. 1a) The worn volume (V_{wear}) at 5MPa for 0 strain is taken from the current lump growth model following the general expression of the Archard wear model, see equation 3.27. 1b) The worn volume needs to be fitted to provide a relation for V_{wear} over the temperature range that matches the range of the calibrated m. 2a) Using the worn volume from the model and the adhered volume from experiments, the value for m can be calculated for the different temperatures using the relation in equation 5.1. 2b) As stated before the value of m will be fitted as a function of temperature. 3) Applying both fitted parameters the relation for V_{trans} is calculated, which is used as a visual check.

1) Worn volume

The worn volume at 5MPa for 0 strain is taken from the lump growth model following equation 3.27. The values from the solver are indicated with the blue circles in figure 5.1a and figure 5.1b for CFI and WFI respectively. The V_{wear} of these two galling initiation models shows a different trend and are therefore fitted differently. The V_{wear} of the CFI is approximated using a second order exponential fit as stated in equation 5.2 and that of the WFI with a second order polynomial fit as in equation 5.3. The fit for CFI and WFI is different because the fit values are purely used to visualize the relation transfer volume over temperature in step 3). Note, the worn volume is not verified with experimental data.

The worn volume for both initiation models shows a different relation, which is due to their initiation criterion. The CFI model shows more worn volume than the WFI model over the temperature range except at 750°C (5MPa and 0 strain). This relation is similar to the amount of initiated asperities from both models at this parameters set, see figure 6.2b and figure 6.2c for CFI and WFI respectively. The CFI model shows more galling initiated asperities for lower temperatures, which leads to more worn volume at the lower temperatures, see figure 6.2b. Also, a larger difference in amount of asperities from 450°C to 550°C can be observed compared to from 650°C to 750°C , which explains that the worn volume shows a smaller slope for the higher temperatures. The

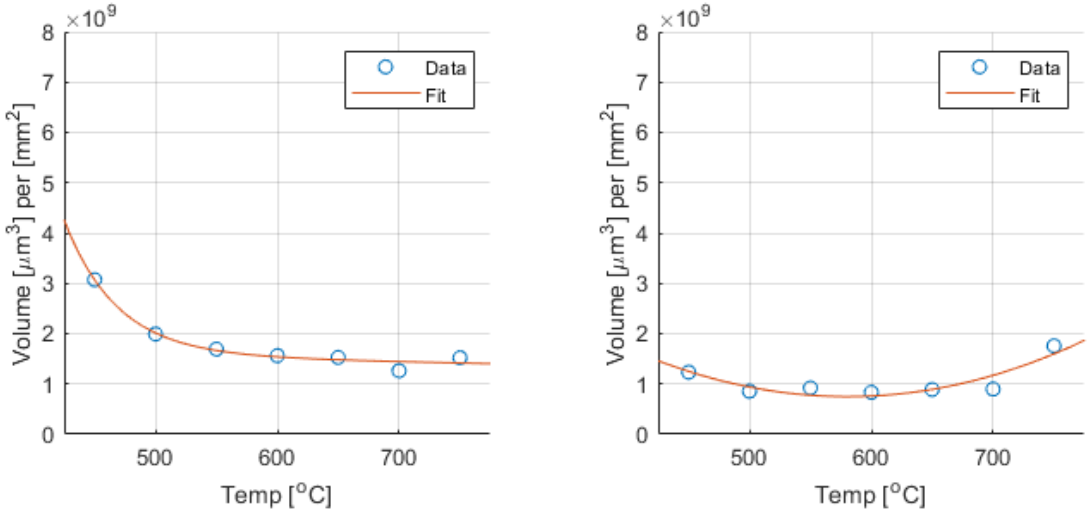

(a) Coating fracture initiation model.

(b) Wedge formation initiation model.

Figure 5.1: Worn volume (V_{wear}) fit with data points from the solver.

worn volume using WFI from 500°C to 700°C show a similar worn volume as does the amount of initiated asperities for galling show a similar amount for these temperatures and 0 strain, see figure 6.2c. Also, compared to the data at from 500°C to 700°C , the V_{wear} at 450°C shows a slight increase and the V_{wear} at 750°C shows a bigger increase (at 0 strain), which is similar to the amount of initiated asperities using WFI for 0 strain in figure 6.2c. Therefore, the relation shown in 5.1b is caused by a combination of the shear factor (f_C) and the definition of the attack angle in the contact model.

$$\begin{aligned} V_{wear\_CF} &= a\exp(bT) + c\exp(dT) \\ a &= 5.239 \cdot 10^{13} \\ b &= -2.326 \cdot 10^{-2} \\ c &= 1.852 \cdot 10^{9} \\ d &= -3.578 \cdot 10^{-4} \end{aligned} \tag{5.2}$$

$$\begin{aligned} V_{wear\_WF} &= p_1 T^2 + p_2 T + p_3 \\ p_1 &= 2.951 \cdot 10^{4} \\ p_2 &= -3.425 \cdot 10^{7} \\ p_3 &= 1.069 \cdot 10^{10} \end{aligned} \tag{5.3}$$

2) Calibration factor

Then, the value for m can be calculated using V_{wear} from the current lump growth model and using V_{trans} from the experimental data. The calculated values are shown as blue circles in figure 5.2a and figure 5.2b for CFI and WFI respectively. In this figure bars are included which represent sensitivity of the $\pm 0.5\mu m$ z-shift from the confocal experiments translated to m. Through these data points a relation has been fitted, which is a second order polynomial for both initiation cases, see equation 5.4 and 5.5 for CFI and WFI respectively. A second order polynomial has been chosen, because the visual check for a first order polynomial does not agree with the relation expected from literature.

The adhered volume should increase over temperature, but applying a first order fit creates a higher value for adhered volume at the lower temperatures, which contradicts findings in literature.

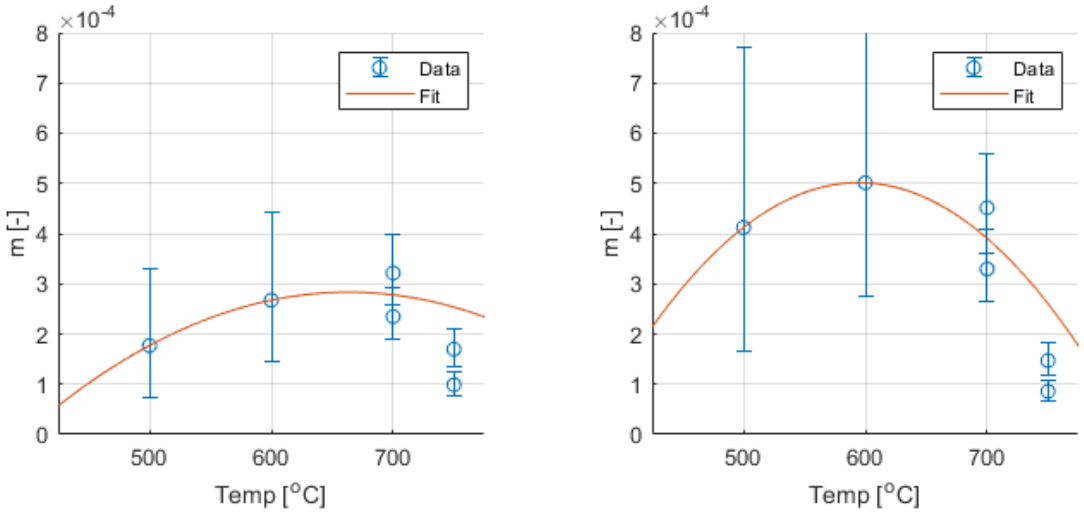

(a) Coating fracture initiation model.

(b) Wedge formation initiation model.

Figure 5.2: Factor m fit with data points, calculated using the worn volume from the solver and adhered volume from experiments.

The experimental data points, used for the fit of the calibration factor m, have been assigned different weights, which are shown in table 5.1. This weights have been applied, because of expected relations from literature and the reliability of the results. First, the measurements at 750°C have been excluded, because they show a contradiction to the expectations of literature, which state an increase of adhered material over temperature. Then, the data points at 700°C are from two different surface measurements, that provide a similar result with a similar sensitivity to the z-shift. This makes the points at 700°C more reliable compared to the measurements at 500°C and 600°C . Also, the measurements at these lower temperatures show a larger sensitivity to the $\pm 0.5 \mu m$ z-shift. This results in the assigned weight shown in table 5.1. The galling model will be valid from 500°C to 700°C since the experimental data at 450°C and 750°C have been excluded.

Weight	=	[1	1	2	2	0	0]
Temperature	=	[500	600	700	700	750	750]

Table 5.1: Weights for the m fit corresponding to the temperatures.

$$
\begin{aligned}
m_{CF}(T) &= p_1 T^2 + p_2 T + p_3 \\
p_1 &= -3.979 \cdot 10^{-9} \\
p_2 &= 5.28 \cdot 10^{-6} \\
p_3 &= -1.468 \cdot 10^{-3}
\end{aligned}
\tag{5.4}
$$

$$
\begin{aligned}
m_{WF}(T) &= p_1 T^2 + p_2 T + p_3 \\
p_1 &= -9.986 \cdot 10^{-9} \\
p_2 &= 1.188 \cdot 10^{-5} \\
p_3 &= -3.029 \cdot 10^{-3}
\end{aligned}
\tag{5.5}
$$

3) Transfer volume

Finally, the fit for the worn volume and the fit factor are combined to visualize the transfer volume. The relation for V_{trans} over temperature for 5MPa and 0 strain can be seen in figure 5.3a and figure 5.3b for CFI and WFI respectively. The CFI shows an increase of adhered volume over temperature till approximately 625°C after which a decrease starts. This decrease in the relation for adhered volume is translated from the fitted calibration factor m, which shows a slight decrease from approximately 650°C . The relation for adhered volume using WFI shows an increase from 600°C to 700°C . However, from 500°C to 600°C the adhered volume shows a slight decrease, which is attributed to the decreasing trend till approximately 600°C in the worn volume when WFI is applied.

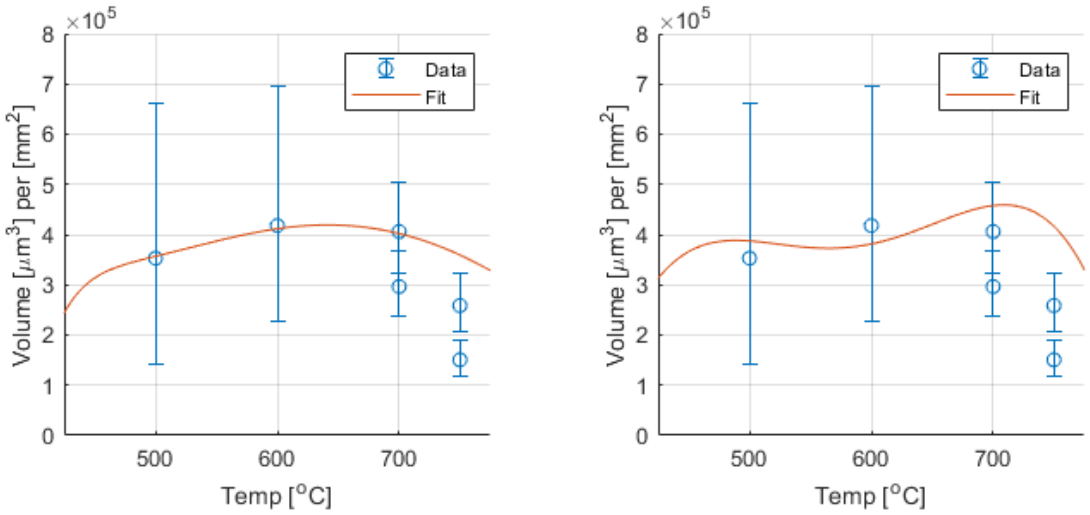

(a) Coating fracture initiation model.

(b) Wedge formation initiation model.

Figure 5.3: Relation for transfer volume V_{trans} using the fitted V_{wear} and m. The data points are from the experiments in section 4.

5.2 Discussion

The calibrated model presented in this chapter is valid for 500°C till 700°C , because not every measurement could be included. This leaves a limited set of data points for which the model is calibrated. The experimental data used suffers from an alignment error of which the impact is not known and therefore the reliability of the data is questionable.

The lump growth model uses worn volume and transferred volume of which only experimental data for verification is present for the latter. The worn volume in this case is highly dependent on the galling initiation model, which raises questions concerning its reliability. In literature the wear rate in the Archard wear model, used to calculate the worn volume, has been adapted to be a function of temperature (section 2.5 *Growth model*).

A linear fit for the calibration factor m would have been more logical, because it has been made a function of temperature based on the relation of the surface energy (adhesion energy) over temperature. However, the fit of m also needed to compensate for the relation of worn volume, which is not verified. A second order polynomial has been applied to provide a better fitted result based on visual conformation for the experimental transfer volume data.

During sliding contact adhesive and abrasive wear are present. Therefore, the experimental data for the transfer volume shows adhered volume affected by abraded volume to an unknown extend. Third body particles or hard embedded particles can affect the tool surface in the form of abrasion. Also, an asperity does not grow infinitely, which is assumed in the lump growth model, but fractures when stresses become too high. These effects are not directly included in the model, but are present during the experiments and only in that way included in the model.

The growth model is based on the adhesive galling, while compaction galling is also a significant influence. The adhered volume from the experiments cannot distinguish between these two ways of material addition. Therefore, the calibration includes both ways of material addition to the tool.

6 Results

In this chapter results from the calibrated model are shown using the parameters from table 6.1. Note that, the input parameters show a wider range for pressure and strain than the values used in the calibration (5MPa and 0 strain). The calibrated relation has been applied for these other pressures and strains as well, to see how well the relation holds up outside its calibrated parameter-set.

First, some model results before the calibration is included will be discussed. This contains the total amount of identified asperities, the amount of asperities initiated for each galling initiation model and the sensitivity of the fracture toughness for the coating fracture initiation (CFI) model. Then the adhered volume calculated by the model, using the calibration factor, for both galling initiation models will be addressed. The adhered volume in this section is calculated using the multi asperity growth where the separation height is updated over sliding steps. More results using the separation height are discussed in the next section. Here, the growth will be visualized to get an idea of how the model deals with multiple growing asperities. In addition to that an investigation is done to see how much overlap between the growing asperities will occur. Finally, the results concerning the multi asperity growth using the update of the tool topography. This is not suitable for the visualization workflow, but can be used to investigate the effect of galling on the coefficient of friction.

	Parameter	**Value**
Input parameters	Pressure	1 MPa - 30 MPa
	Strain	0.0 - 0.2
	Temperature	450°C - 750°C
	Velocity	[-]
	Tool roughness	0.6 μm
Material parameters	B	1.25
	T	0.4619
Galling initiation parameters *Coating fracture*	a	40 μm
	K_{IC}	0.25 MPa/$\sqrt{m}$
	Y	1.12
Lump growth parameters	c_s	2
	l_{slide}	0.2 m
	μ_{max}	0.4619

Table 6.1: Parameters for galling model.

6.1 Amount of asperities

Both galling initiation models are applied within the TriboForm Solver and are compared based on the amount initiated asperities for galling. Here, a visual representation of the asperity patches will be shown in figure 6.1. The total amount of asperities of the tool in contact with the sheet can be seen in figure 6.2a will be discussed. The next section will compare the amount of asperities initiated for CFI and WFI, shown in figure 6.2b and figure 6.2c respectively. Finally, the sensitivity of the fracture toughness used in the CFI model will be discussed.

In figure 6.1 the total amount of asperities in contact, with the amount of asperities initiated for galling based on both the galling initiation models, are shown. In addition, the figure provides insight into the size of the initiated asperities, where mostly the large asperities will not be initiated

in either one of the galling initiation models. In both cases this is due to the large attack angle of these asperities, which causes an asperity to be outside of the wedge formation range for WFI and which causes the stress intensity factor for CFI to be insufficient to break the coating due to the lower coefficient of friction for a single asperity. More asperities according to the CFI model can be observed, indicating that more asperities are initiated using the CFI model for these conditions. The asperities initiated based on WFI are mostly also initiated based on the CFI model. In appendix C.1 more similar figures can be found. These figures are used to visually support the reasoning for the amount of contact patches.

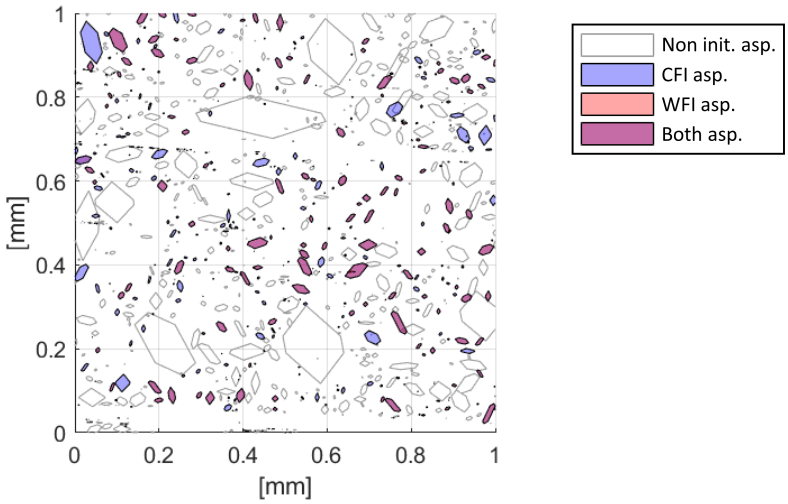

Figure 6.1: Top view of all the identified asperity patches at 650°C , 5MPa and 0.0 strain.

6.1.1 Identified amount of asperities

The first difference that can be observed is in the total amount of asperities in contact per surface area, figure 6.2a. A decrease of asperities in contact over strain is observed which is due to the merging of stretched asperities. This effect is most extreme for a temperature of 450°C where the amount of small asperities are merged more easily (figure C.3a versus figure C.4a). The relation for the amount of asperities in contact over pressure increases at first, which is due to the increase in contacting spikes of the sheet surface (figure 3.2a). This increase in amount stabilizes and then starts a decrease in amount, which is due to the merging of flattened asperities (figure 6.1 versus figure C.2). The decrease over temperature has to do with the ease of flattening, and therefore merging, of the contacting asperities, which is easier at higher temperature (figure 6.1 versus figure C.3). However, an exception can be seen for 750°C at low pressures. This behavior is due to the ease of flattening at high temperature, which causes more (very) small asperities to be identified in the contact model. The merging of asperities at higher pressures is still valid, but the identification of small asperities is more dominant (figure C.5). Also, the amount at 750°C for 5MPa is higher than at 750°C for 1MPa, which is due to the identification of more (very) small asperities (figure C.6). This relation at low pressure for 750°C stands out in the figures showing the amount of asperities initiated for galling.

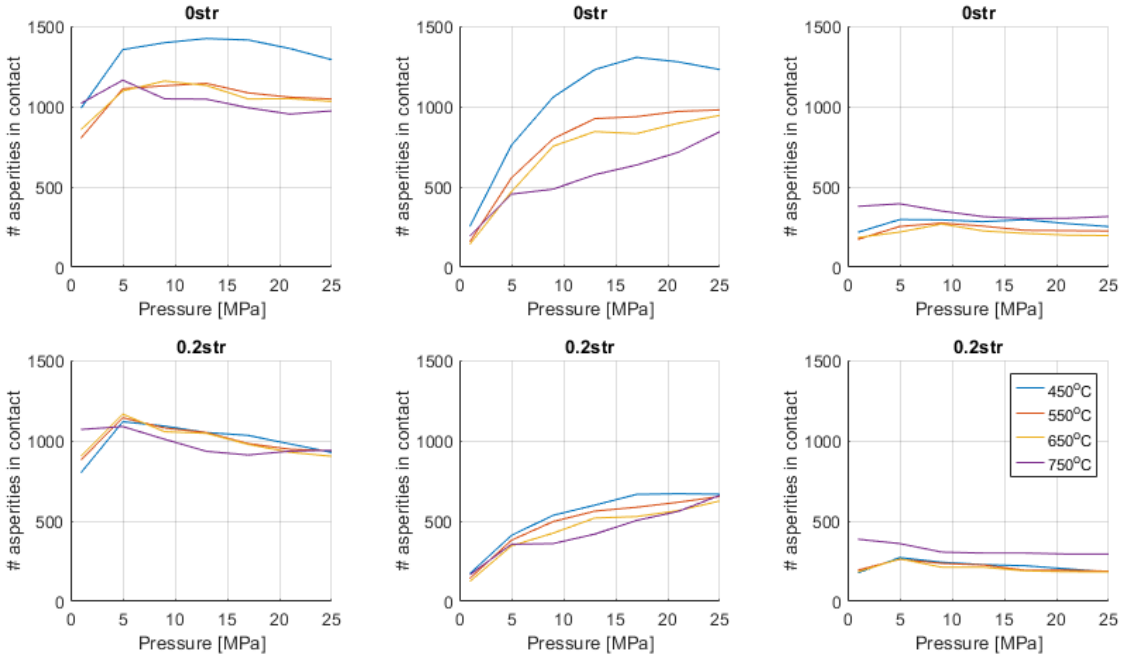

(a) Total amount in contact. (b) Asperities initiated using CFI. (c) Asperities initiated using WFI.

Figure 6.2: Amount of asperities.

6.1.2 Galling initiated asperities

The WFI model does not show a big variation in the amount of asperities initiated over pressure, while the CFI model shows an increase in the amount over pressure. The initiation according to the WFI model uses the attack angle of an asperity and the shear factor (f_C), which is only a function of temperature, to determine whether an asperity is initiated for galling. The relation for WFI is therefore not directly linked to pressure, while the CFI model uses the nominal pressure to calculate the stress intensity factor (K_I) for its fracture criterion, see equation 3.22. The effect of strain on the amount of initiated asperities can be clearly seen in the CFI model, this time as a decrease of initiated asperities, while the amount for WFI model remains similar. The WFI model relies on the shape of the asperity, which is not directly affected by the strain. However, the initiation for CFI is affected, because the real fractional contact area (α) increases for a higher strain. This causes a decrease in the effective hardness and, therefore, a decrease in stress intensity factor. The CFI model shows a decrease of initiated asperities when temperature increases. This decrease in initiated asperities over temperature is related to the amount of asperities in contact over temperature, since the criterion for CFI does not include temperature directly. However, the WFI model shows similar results over temperatures except for 450°C at 0 strain, 750°C at 0 strain and 750°C at 0.2 strain, which show an increase in the amount of asperities. This is attributed the shear factor (f_C), because a higher shear factor, see figure 2.9, allows for a wider range in attack angle to be initiated using WFI. The shear factor at 750°C is the highest and provides more initiated asperities. The higher shear factor at 450°C compared to that of 550°C and 650°C , see figure 3.3, is only apparent in the 0 strain situation. Therefore, the difference in initiated asperities at different temperatures is also attributed to the definition of attack angle, from patch to elliptical paraboloid, in the contact model.

6.1.3 Sensitivity fracture toughness

In the CFI model the fracture toughness (K_{IC}) of the coating dictates when an asperity will be initiated. An estimated value, based on data from literature, is used for this and therefore could very well vary. The impact of a slight variation in fracture toughness will therefore be addressed as a sensitivity check. The slight variation for the used fracture toughness of 0.25 MPa$\sqrt{m}$ will be $\pm$0.05 MPa$\sqrt{m}$. In addition to that the fracture toughness will also be checked for 0.50 MPa$\sqrt{m}$, which is based on the fracture toughness for fine grained Fe_2Al_5 in table 3.2.

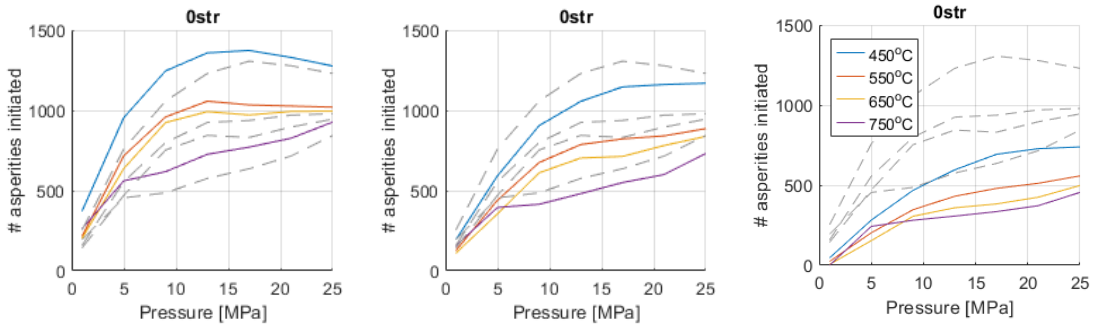

(a) K_{IC} = 0.20 MPa$\sqrt{m}$. (b) K_{IC} = 0.30 MPa$\sqrt{m}$. (c) K_{IC} = 0.50 MPa$\sqrt{m}$.

Figure 6.3: Amount of asperities initiated using CFI with a varying fracture toughness. *Grey dashed lines show results using* $K_{IC} = 0.25$ *MPa*$\sqrt{m}$.

The amount of asperities initiated due to the three different fracture toughness can be seen in figure 6.3. It is observed that more asperities will be initiated for a lower fracture toughness and vice versa, which is as expected. The difference between the original fracture toughness (0.25MPa$\sqrt{m}$) and the variations is expressed in a deviation percentage with the total amount of asperities (figure 6.2a) as the reference amount. This provides an average deviation over the pressure range of approximately 10% higher, 9.5% lower and 34.5% lower for a fracture toughness of 0.20 MPa$\sqrt{m}$, 0.30 MPa$\sqrt{m}$ and 0.50 MPa$\sqrt{m}$ respectively. A small change in the fracture toughness already leads to a small difference in the initiated amount of asperities. However, when the fracture toughness is significantly higher, which can be caused by a finer grained layer, the amount of initiated asperities for galling change more drastically. The temperature of the austenitization process before forming dictates which intermetallic phases are present during the deformation. This should be verified for the conditions in hot forming.

It should be noted that the fracture toughness criterion is valid for brittle fractures. The material becomes more ductile for the higher temperatures, which makes the application of the fracture toughness more questionable for the higher temperatures.

6.2 Adhered volume

In this section the effect of the calibration on the adhered volume is shown for both galling initiation models. The figures 6.4 and 6.5 show the adhered volume over sliding length for different temperatures and pressures. As stated before, the galling model is valid for 500°C - 700°C . First, when comparing the adhered volume after 2m for 5MPa from the result figures here to the adhered volume used in the calibration a difference can be seen. The volume shown in the result figures is bigger compared to the calibration figures. This is due to the use of the calibration factor m. In the calibration section, the fraction (m) is calibrated for the total volume after 2 meters of sliding for

different temperatures, while this fraction is applied to each individual asperity for every sliding step. This has resulted in an overestimation of adhered volume compared to the experimentally determined adhered volume.

Using the CFI model to initiate asperities for galling an increase of adhered volume is observed over pressure. This increase is linked to the increasing amount of asperities over pressure (figure 6.2b) since the calibrated factor m is applied for every single galling initiated asperity. An increase in adhered volume from 500°C to 600°C is shown. However, for the higher pressures (17MPa - 25MPa) a decrease in volume is observed. This decrease is attributed to the calibration for CFI, which shows a slight dip from about 650°C to 700°C (figure 5.3a). The WFI model shows a different relation over pressure compared to the CFI model. An increase over pressure is observed from 1MPa to 10MPa and a more or less constant relation is observed for the higher pressures. Again, the relation for adhered volume is linked to the amount of initiated asperities (figure 6.2c), where the amount of asperities using WFI is not influenced by pressure. The relation of adhered volume over temperature when WFI is applied, shows an increase in the valid range for the galling model (500°C - 700°C). The increase over this temperature range is also observed in figure on the transfer volume in the calibration section (figure 5.3b).

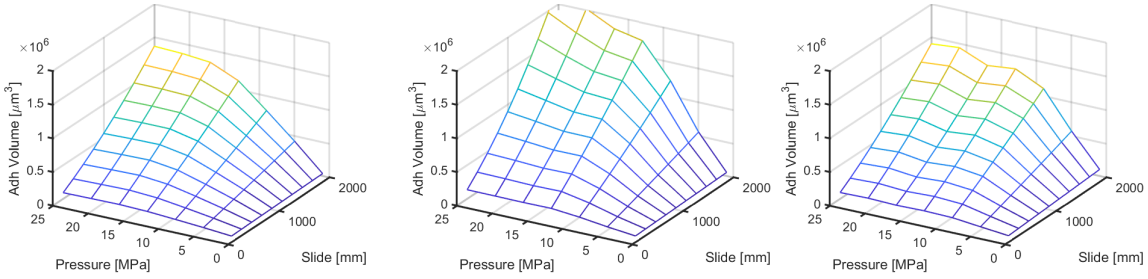

(a) 500°C . (b) 600°C . (c) 700°C .

Figure 6.4: Adhered volume using CFI for 0 strain with the calibrated value for m.

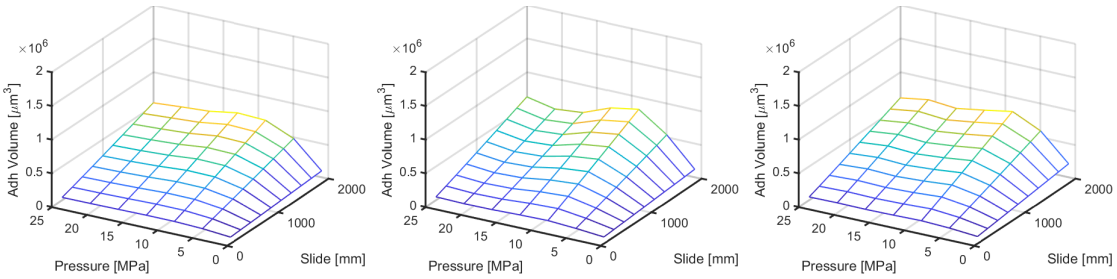

(a) 500°C . (b) 600°C . (c) 700°C .

Figure 6.5: Adhered volume using WFI for 0 strain with the calibrated value for m.

The adhered volume for both models at 5MPa are very similar which is as expected, because the model has been calibrated at 5MPa. However for the higher pressures a difference between CFI and WFI is observed, which is attributed to the amount of asperities initiated for galling. Another difference can be seen in the adhered volume at 1MPa. Both models show a decrease in adhered volume, but the value for the WFI model is higher compared to the CFI model. This again is attributed to the amount of initiated asperities, because WFI has more initiated asperities at 1MPa compared to CFI.

6.3 Multi asperity growth - update separation height

In section 3.5 the growth of a single asperity has been described. Here, the interaction of multiple asperities growing according to the 'update separation height' multi asperity growth situation will be visualized. Also, the interaction of the asperities will be evaluated based on the overlap between asperities. Finally, the amount asperities initiated for galling over sliding length are evaluated.

6.3.1 Visualize growth layers

The multiple asperity growth is shown in figure 6.6 for a zoomed top view of the surface, since the complete surface would make the figures unclear. The figure uses 600°C , 5MPa and 0 strain and shows at most 5 layers indicating a sliding length of 1 meter. The figures only show the initiated asperities according to their own criteria, where CFI shows more initiated asperities compared to WFI. The growth is shown for a pressure of 5MPa and 0 strain, which is also used in the experimental strip draw tests for the calibration. Therefore, at this condition set the adhered volume is very similar between the CFI and WFI model. This translates to the growth in the fact that the adhered layers are bigger for WFI compared to CFI, because the added volume should be divided over less asperities when WFI is applied. Some of the asperities show fewer growth layers. This is due to the tool asperity not being in contact with the sheet plateau anymore for the updated separation height.

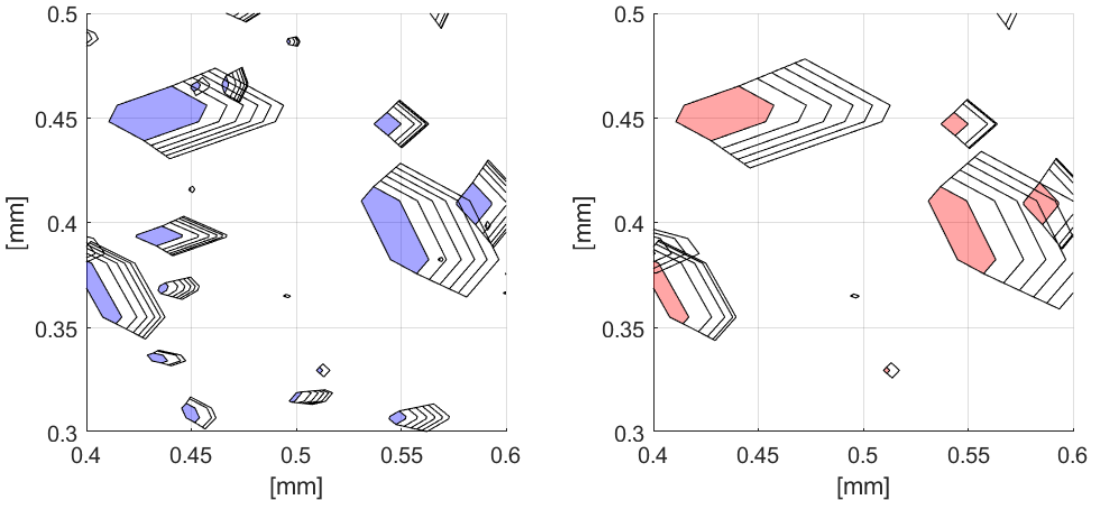

(a) CFI. (b) WFI.

Figure 6.6: Zoomed top view of the growth of asperities for 5 steps (1m) for 600°C , 5MPa and 0 strain.

6.3.2 Evaluate asperity overlap

The overlap between asperities will be evaluated, because in reality the merging of asperities over sliding due to galling is observed [3]. Therefore, it is investigated if and how much the model shows potential merging of asperities, because the model does not account for asperity interaction at this point. The interaction between growing asperities is looked into based on the percentage of initiated asperities which have at least one overlap with another asperity. The percentage of overlapping asperities over sliding length can be seen in figure 6.7 for one parameter set (600°C , 5MPa and 0 strain). A similar figure for 500°C and 700°C can be found in appendix C.2. Note that

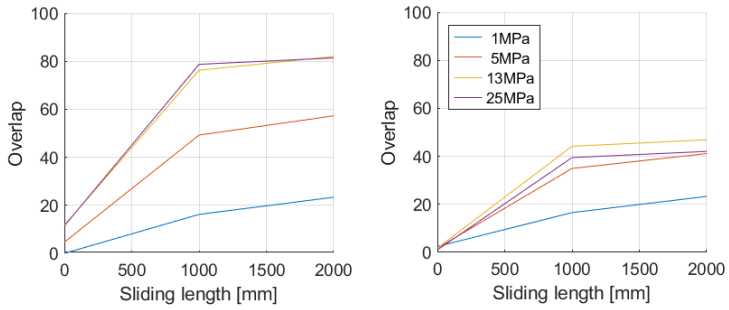

(a) CFI. (b) WFI.

Figure 6.7: The percentage of asperities which have at least one overlap with another asperity at 600°C and 0 strain for different pressures with the calibrated value for m.

only the overlap has been checked for the original asperity shapes, the shape after 5 (1m) adhered layers and the shape after 10 adhered layers (2m) due to the long run time when the overlap check was included.

From the percentage figure it can be seen that the overlap is less for lower pressures. For the CFI model this is observed for 1MPa and 5MPa, while only 1MPa shows a significant difference compared to the other pressures for the WFI model. On the other hand the overlap percentage for $\geq$5MPa for the WFI model is lower compared to the CFI model. This is explained by the different amount of initiated asperities. The CFI model has a higher overlap percentage because more asperities are initiated and therefore the asperities are in general closer to each other. This can also be seen in the slope from the initial asperity to the shape after 5 additional layers. Since the asperities are closer to each other it is also more easy to overlap for a lower sliding length.

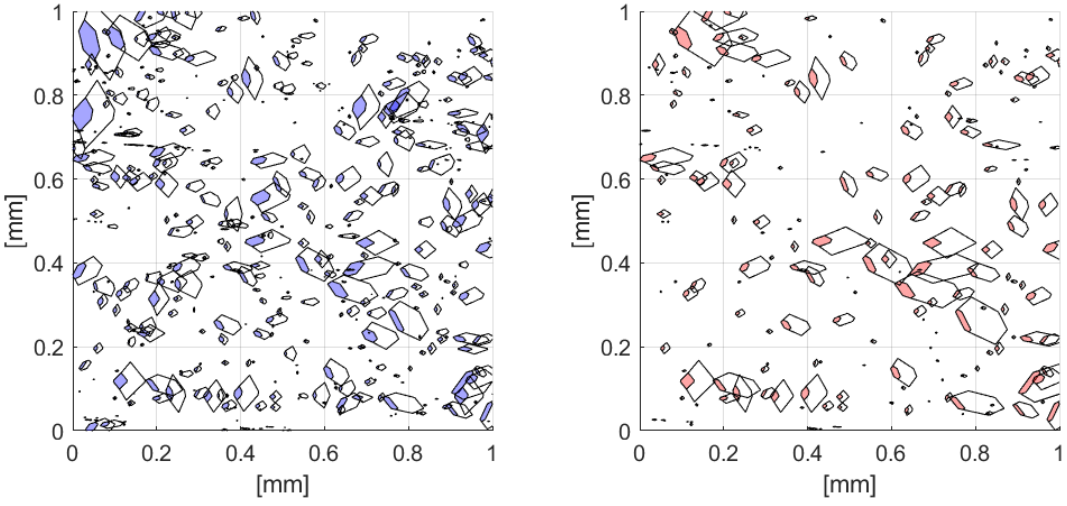

(a) CFI. (b) WFI.

Figure 6.8: Top view of the growth of asperities after 2m (10 steps) for 600°C , 5MPa and 0 strain.

The reasoning for the difference in overlap percentage is supported with a top view of the tool asperities for 600°C , 0 strain with 5MPa (figure 6.8 and 25MPa (figure 6.9). The initiated asperities

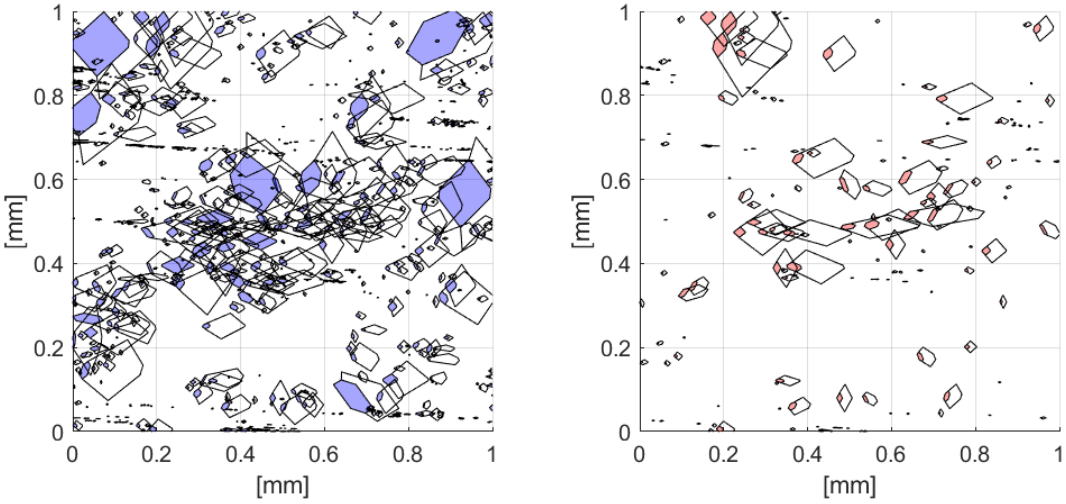

(a) CFI. (b) WFI.

Figure 6.9: Top view of the growth of asperities after 2m (10 steps) for 600°C , 25MPa and 0 strain.

with respect to all asperities in contact is added in the appendix in figure C.7. In the figures for 5MPa and 25MPa with 600°C and 0 strain the shape of the initiated asperity (colored part) is shown and the growth after 10 growth steps. The overlap for the initiated asperities (colored parts) with 5MPa is low. After the 10 adhered layers the overlap does not seem extreme even though the overlap percentage is $\approx 50\%$ and $\approx 40\%$ for CFI and WFI respectively. When taking a look at the situation with 25MPa the CFI model shows a very full and chaotic top view (figure 6.9a) and the WFI model (figure 6.9b) is more similar to the growth situation at 5MPa (figure 6.8b). This is also represented by the overlap percentage, where the CFI model has an overlap of $\approx 80\%$ and the WFI model an overlap of $\approx 40\%$.

The overlap percentage and the supporting figures for both galling initiation models indicate that the asperity interaction based on asperities merging is quite significant. This interaction should be included to approach reality more closely. This asperity merge then would impact the adhered volume for the next growth layer, since the calibration factor (m) is applied for each individual asperity. Therefore, the next growth layer would have less adhered material.

6.3.3 Asperities over sliding length

The evolution of the amount of asperities, using the growth case based on the separation height, in contact over sliding length is visualized in figure 6.10 for different pressures, temperatures and both galling initiation models. Note, the model can only show the growth of an asperity and does not include a break-off criterion for the lump. Therefore, the amount of asperities can only decrease over sliding length. Also, the amount of asperities for the CFI model start higher than shown in the figure to show the lower amount of asperities more clearly.

In general the relation of CFI and WFI over sliding length is attributed to the amount of asperities initiated for the models, see figure 6.2. 1) At 1MPa the amount of asperities over sliding length is similar for both galling initiation models. 2) At the higher pressures the CFI model shows more remaining asperities compared to WFI. 3) A higher temperature for CFI provides less remaining asperities after the presented sliding length (13MPa and 25MPa). 4) The WFI model does not show a large difference between the temperatures for a given pressure, while the CFI model does show a

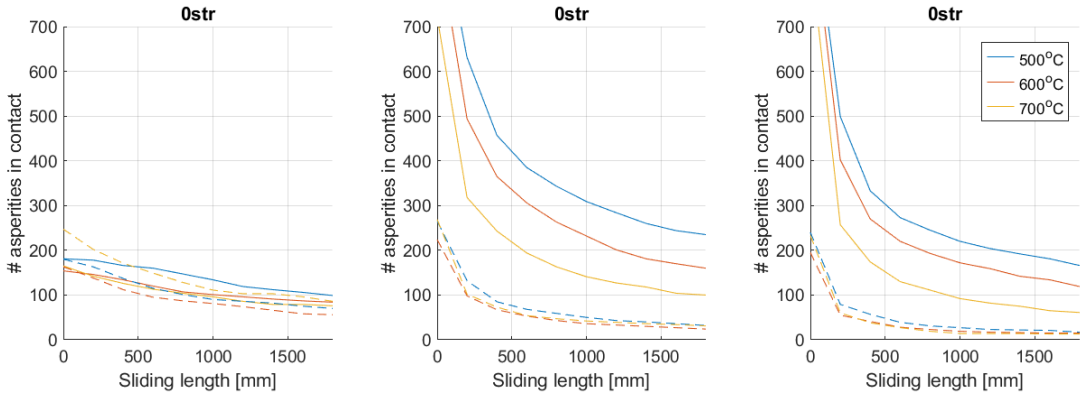

(a) 1MPa. (b) 13MPa. (c) 25MPa.

Figure 6.10: Amount of asperities in contact over sliding with a step size of 200mm using the calibrated value of *m*. *Solid line*: CFI, *Dashed line*: WFI.

difference (except at 1MPa).

A low pressure for the models shows a more steady decrease in the amount of asperities in contact compared to a higher pressure. At the high pressures (13MPa and 25MPa) for both models it can be seen that the first steps show a larger decrease after which a (more) steady decrease follows. This is attributed to the elimination of the (very) small asperities, which are barely in contact. This decrease in the first steps is more severe for 25MPa compared to 13MPa and especially compared to 1MPa. In addition, the decrease in these first steps (at 13MPa and 25MPa) is more severe for a higher temperature. These differences in the decreasing slopes is related to the (very) small asperities identified by the contact model and the adhered volume at high pressure and temperature. At higher temperature the contact model identifies more small asperities, which will fall out of contact more quickly. Also, the adhered volume at higher temperature and pressure is higher. Therefore, the separation height decreases faster compared to a lower temperature and/or pressure, which makes it easier for the small asperities to fall out of contact. Another observation is that a lower temperature (for 13MPa and 25MPa) reaches the steady decrease later compared to high temperature, which is especially clear for the CFI model. This is attributed to the small asperities, which will fall out of contact during these first steps. This takes longer for a lower temperature. The amount of asperities remaining after the presented sliding length for the same temperature decrease over pressure. This is not valid for the CFI model with 1MPa, because significantly less asperities are initiated compared to the asperity development at 13MPa and 25MPa. The fewer remaining asperities for the models is caused by the more adhered volume due to the higher pressure, which results in larger steps in the separation height.

6.4 Multi asperity growth - update tool topography

6.4.1 Friction over sliding length

To evaluate friction over sliding length the multi asperity case which updates the tool topography is used. Updating the tool topography allows for the inclusion of the contact model, which calculates the friction, for every sliding step, see figure 3.20 for an overview. Therefore, the effect of adhered material on the surface is evaluated, which will be done by evaluating the COF over sliding length. In addition, the fractional real area of contact (figure 6.12) at the start of each sliding step will be

visualized to better understand the relation of COF of the surface over sliding length.

Here, smaller steps are used compared to the l_{slide} from table 6.1. This has also resulted in a smaller sliding distance compared to the previous results. The sliding step size has been reduced, because the reevaluation over the contact model is sensitive to large steps. A large step can cause the initiated amount of asperities to go down more quickly and even reach zero initiated asperities, which causes problems in the model. The total sliding length has also been reduced, to keep the run time to a manageable size.

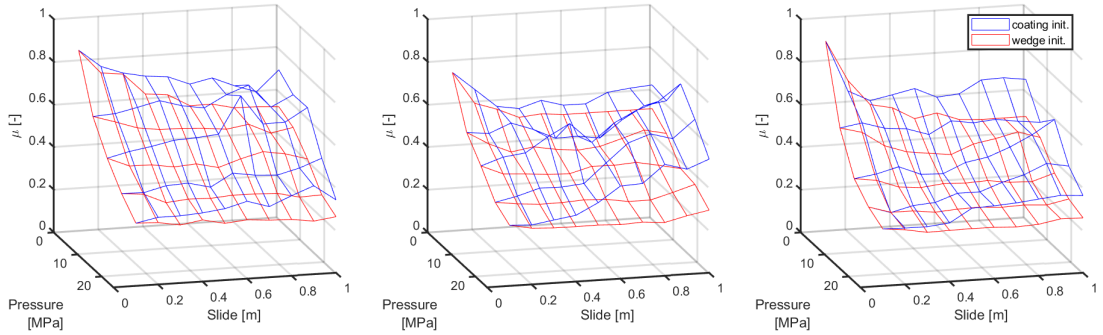

(a) 500°C . (b) 600°C . (c) 700°C .

Figure 6.11: Development of coefficient of friction over sliding length for 0 strain with the calibrated value for m.

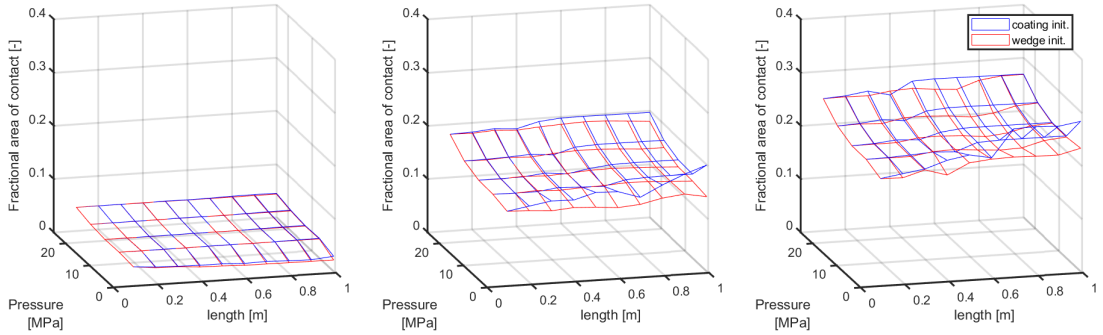

(a) 500°C . (b) 600°C . (c) 700°C .

Figure 6.12: Fractional real area of contact over sliding length using the multi asperity topography update for 0 strain with the calibrated value for m.

In general, the CFI model shows an increase of COF over sliding length when the fractional real area of contact increases over sliding length. This is attributed to a transition to another wear mode of the asperities, which causes a larger contribution to the COF. A few exceptions on the general relation of CFI over sliding length can be seen at low pressures (1MPa). At 500°C the complete trend over sliding length shows a decrease of COF over sliding length and for 600°C and 700°C only the first few sliding steps show a decrease after which a stable increase in COF is observed. The COF shows an increase in COF from 600°C to 700°C for the lower pressures (<10MPa). This increase is not observed from 500°C to 600°C because the initial decrease over sliding length is less severe for 500°C compared to the higher temperatures. At 600°C for higher pressures (>15MPa) the increase of COF is higher compared to 700°C . This is caused by the calibration for CFI, which

shows a slight dip in adhered volume from about 650°C to 700°C .

The WFI model shows a decrease in COF over sliding length for every situation. Also, the fractional real area of contact using the WFI model shows an increase over sliding length. Less asperities are changing during lump growth when the WFI model is applied, which provides less asperities to transition to another wear mode compared to the CFI model. The decrease at low pressure for the first sliding steps is more severe compared to the higher pressures. Also, the WFI model shows a decrease in COF after the total sliding length over temperature.

The CFI model has a higher COF over sliding length compared to the WFI model. This difference is caused by the amount of asperities initiated for each model, because the fractional real contact area for both cases shows an increase over sliding length. The increase of fractional real contact area for CFI is higher compared to WFI. However, the relation for the coefficient of friction for CFI is increasing, while the relation of WFI is decreasing. Therefore, the difference is attributed to the amount of contributing asperities, which is the other parameter influencing the COF (equation 2.4). The correct relation regarding COF over sliding length is not investigated in this research. A literature review and additional research over sliding length should be done to verify the correct relation.

6.5 Summary

- The CFI model has more galling initiated asperities compared to the WFI model. The CFI model shows an increase in amount over pressure, a decrease in amount over temperature and a decrease in amount over strain. The WFI model is barely affected by a change in pressure, temperature or strain. This is attributed to the proposed criterion for each model.

- The sensitivity of the fracture toughness applied in the CFI model has been looked into. A change from 0.25 MPa$\sqrt{m}$ to 0.50 MPa$\sqrt{m}$ causes an average deviation of 34.5% of initiated asperities over pressure. The percentage is the difference between the changed fracture toughness and the original fracture toughness with respect to the total amount of asperities in contact. This difference is quite significant. Therefore, the fracture toughness should be verified for the conditions in hot forming.

- The CFI model shows more adhered volume for higher pressures ($>$10MPa) compared to the WFI model. Also, the CFI model shows an increase in adhered volume over pressure, while the WFI model only shows an increase from 1MPa to 15MPa and shows a more or less constant relation from 15MPa to 30MPa. This is mainly related to the initiated amount of asperities for each model.

- The growth of multiple asperities using the separation height multi asperity growth model is visualized using a top view. In addition, the overlap between asperities is investigated. The asperity growth for 600°C and 5MPa after 2m (and also after 1m meter) provides an overlap percentage of $\approx$ 50% and $\approx$ 40% for CFI and WFI respectively. This percentage indicates the amount of asperities that at least have one overlap with another asperity. This percentage becomes even higher for higher pressures. Therefore, the model should include the merging of asperities when overlap is registered.

- The amount of initiated asperities over sliding length using the separation height multi asperity growth model is evaluated. From this it can be concluded that the (very) small initiated asperities only contribute briefly to the total adhered volume.

- The tool topography multi asperity growth model is used to evaluate friction over sliding length. In general, the relation for COF increases over sliding length for CFI and decreases

over sliding length for WFI, which is attributed to the amount of asperities involved with lump growth. The tool topography multi asperity model is not applied in the validation section.

7 Validation

In this chapter the galling model will be applied to predict galling amount on a production part. First, the workflow and assumptions in the galling projection onto the tooling of a production part will be discussed. This galling projection will then be applied on multiple cases. Experiments are performed at Tata Steel on a B-pillar for a qualitative comparison of the galling prediction. Then two different industrial parts from Volvo Cars (the A-pillar and the Side Member) are analyzed to verify if the correct locations can be identified with the galling model. The two proposed galling initiation models (coating fracture initiation and wedge formation initiation) will be compared for these three validation cases to check which initiation model is more favorable.

7.1 Workflow visualization galling

The workflow to get the visualization of galling on a part uses the steps shown in figure 7.1. The TriboForm Software is used to create a TriboForm library, which also contains the galling output information. The friction library created in this step will be applied in the AutoForm simulation of the production part of interest. A TriboForm plug-in is used to extract the nodal sheet parameters (pressure, strain, temperature, velocity and relative displacement) per time step needed into a special output file to visualize the galling in the TriboForm Analyzer (internal development version). The galling will be projected onto the tooling and therefore the meshes of the tooling are needed. Also, the displacement profile of the tooling is exported to be able to connect the sheet nodes to the correct location of the tooling.

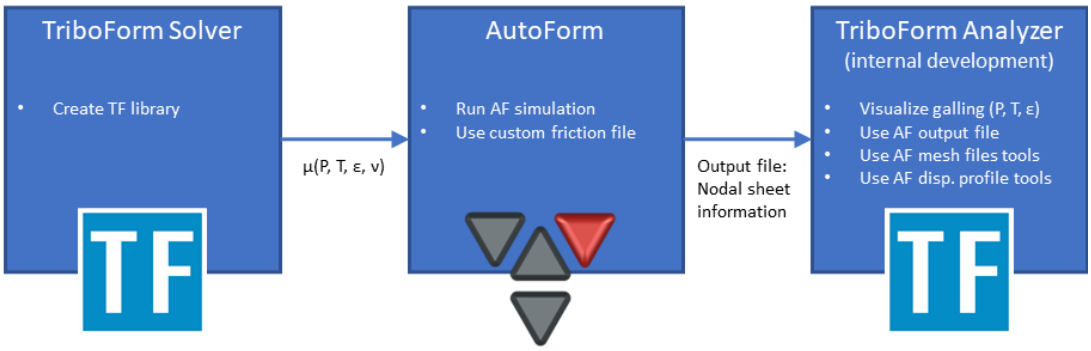

Figure 7.1: Workflow for the visualization of galling on a production part.

Additional information on how the galling output, which is included into the TriboForm library, is applied in the TriboForm Analyzer (internal development version) will be stated below:

- The projected galling output is galling amount ([g/mm^2]). The severity for galling amount is not known, which makes the value of galling amount useful for a comparison.
- The galling projection is a post processing step based on the temperature, pressure and strain of the sheet and based on the sliding length, which is the relative contact of the tool with the sheet.
- The galling amount output from the TriboForm Solver is fitted with a radial basis function.
- The galling projection on the tooling will be that after one forming process.
- The input for temperature is the sheet temperature.
- When the temperature is outside of the valid temperature range (500°C - 700°C) for the galling projection, the closest temperature output value is used.

- When the pressure is above of the pressure range (1MPa - 30MPa) for the galling projection, the closest pressure value is used.
- When the pressure is below of the pressure range (1MPa - 30MPa) for the galling projection, a linear relation from 0MPa (no galling) to 1MPa is used.
- The strain range of 0 - 0.2 is applied as a range of 0 - 0.4 in the galling projection. This assumption is used for the friction model, because in experience the strain relation is overestimated. Therefore, the extended range will also be applied within the galling model.
- In the galling amount prediction only one roughness can be applied over the whole surface of the tooling. If different roughnesses are expected for the tooling the workflow should be repeated for this roughness.
- The relation for galling over sliding length is taken linearly between the first and last sliding step during the library creation (l_{fst} = 0.2m, l_{lst} = 2m).
- The relative displacement (sliding length) is calculated using the nodal velocity of the sheet and the time between the iterations.

7.2 B-pillar Tata Steel

7.2.1 Experimental setup

The experiments are concerned with only the T-part of the B-pillar performed at Tata Steel [63]. In figure 7.2 the setup for the experimental B-pillar forming process is depicted. In this setup the punch is made up out of two separate parts.

Figure 7.2: Experimental setup for the B-pillar forming process.

A surface measurement of the sheet and the tool has been done to verify the applicability of the calibrated model. When comparing the topography of the B-pillar tooling and B-pillar sheet to the ones used in the model similarities are spotted. The topography of the sheet looks very similar with a small difference in roughness, with 1.92μm of the model versus 2.18μm of the new measurement. The topography of the model will be used in the B-pillar validation, because the topography looks very similar and because in that way the results from the previous section can be used to support the predicted galling amount. A measurement on the punch radius and of the die radius have been provided. The roughness of the punch radius is close to the roughness of the tooling used in the model (Sa = 0.62μm and Sa = 0.60μm respectively). However, the roughness of the die radius is smoother compared to the applied tool topography (Sa = 0.13μm and Sa = 0.60μm respectively), which is quite different. Therefore, the model with the calibrated tool roughness (Sa = 0.6μm) as well as the model with a more matched tool roughness (Sa = 0.2μm) will be used for the die

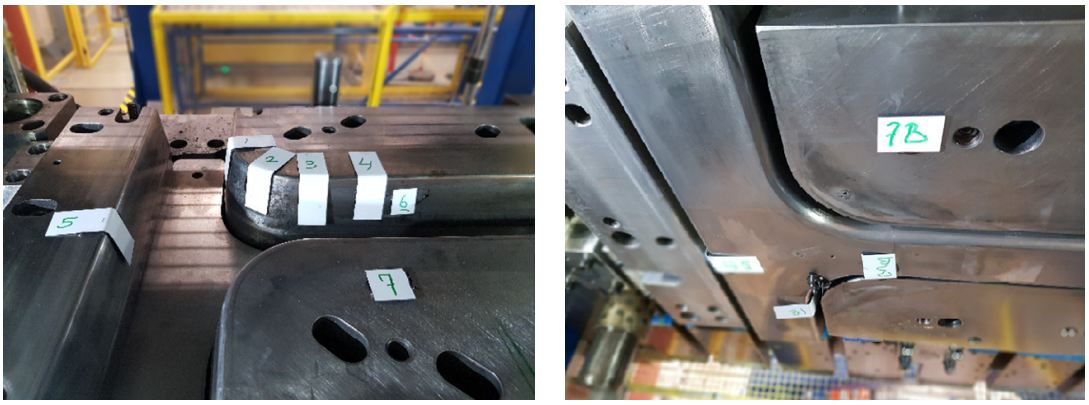

(a) Die. (b) Punch (1B, 3B, 5B and 7B).

Figure 7.3: Measurement location on the B-pillar tooling.

of the B-pillar. The tool roughness for both cases will be used in the visualization to show the difference in galling amount when a different roughness is applied. The topography and surface height distribution for the applied tool and sheet material are found in appendix D.1. Confocal measurements have been performed on the tool radius after 5, 15, 24, 50 draws and before the first draw. These tool measurement have been made at the locations on the tooling as indicated in figure 7.3.

7.2.2 Confocal measurements

The confocal images for location 1, 2 and 5 on the die will be shown in figure 7.4. The topography evolution of the other locations on the can be found in appendix D.2, because the evolution of location 3 and 4 is similar to location 1 and location 6 and 7 do not show galling behavior. The measured topography of the punch does not show galling behavior and is therefore only shown in the appendix in figure D.4. No confocal measurements have been performed on the blank holder. The presented confocal images are the only information since the raw data is not available. In addition, the sliding direction per confocal image is not known. The measured location on the radius is not verified, which can lead to differences in the local confocal measurement. The die radius at location 5 shows more galling over 50 draws compared to location 1 (and location 3 and 4, see figure D.5). This difference is not quantified like the volumes in section 4, because there are no roughness line measurements over the radius, which serves as a reference to calculate an adhered volume. The difference in location 1 and 5 seems to be a difference in galling mechanism, where location 1 shows more adhered galling and location 5 shows a compaction galling front. Here, location 2 is also shown, because it shows less spots with adhesive galling compared to location 1.

7.2.3 Results projection galling

Introduction to the forming setup

The B-pillar tools, as they are used in the AutoForm simulation, are shown in figure 7.5. The blank is added to this figure to show where contact between the sheet and tool can be expected. The final product shape with this tooling is shown in figure 7.6.

The parameters applied for the galling projection onto the B-pillar are shown in table 7.1. The AutoForm simulation and galling prediction uses the material topographies applied in the calibration, which are similar to that of the B-pillar experiments. This is an initial galling projection

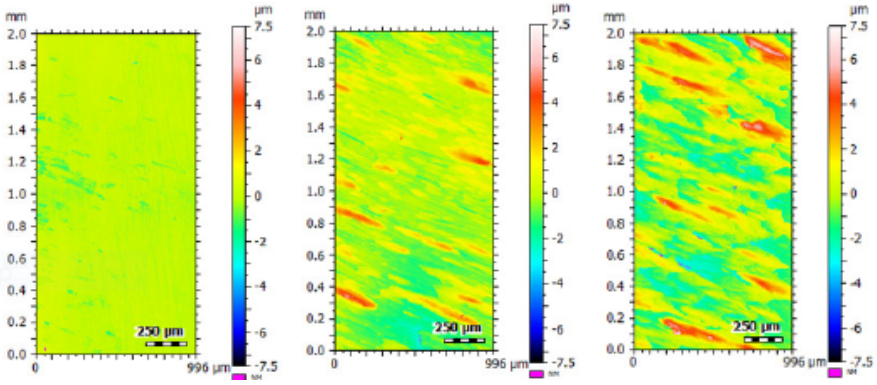

(a) location 1.

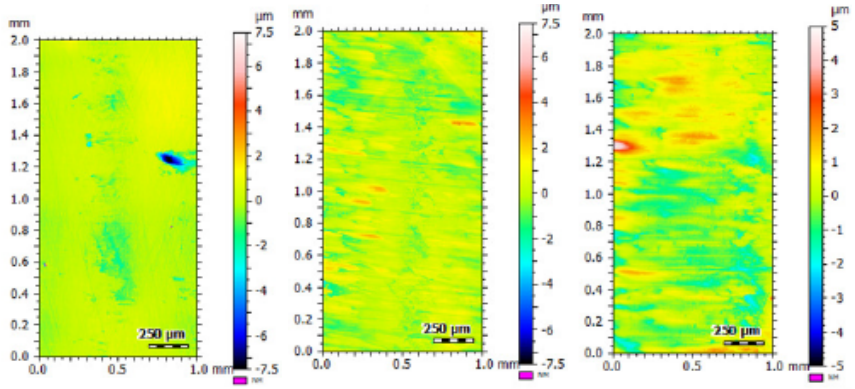

(b) location 2.

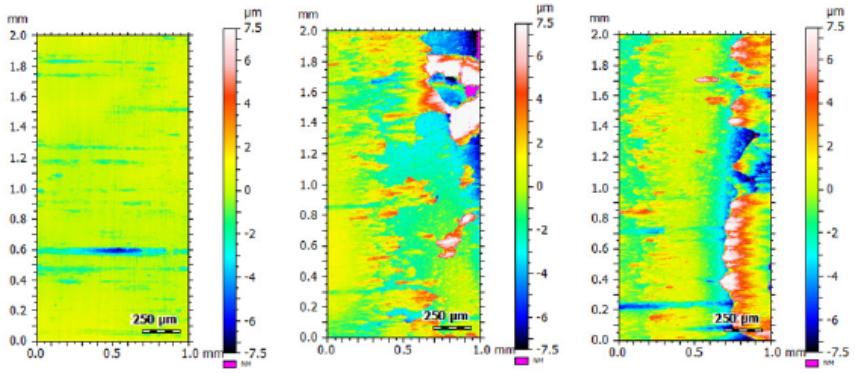

(c) location 5.

Figure 7.4: Topography evolution of the die radius [63]. *Fltr: Reference, after 24 draws and after 50 draws.*

to see how well the galling model performs when it is applied on a real product. Note, that the roughness for the die will be overestimated with the current model. The Temp_{start} for the sheet and the tool are the temperature at which the forming process is initiated. The temperature of the sheet surfaces will change due to the contact during forming, while the tool temperature will remain constant during the AutoForm simulation. In reality, the tool temperature will change during a forming process and also over multiple forming processes.

The cumulative sliding length is the relative displacement between the tool and the sheet in contact after one draw. This is shown in figure 7.7 for the die, the punch and the blank holder.

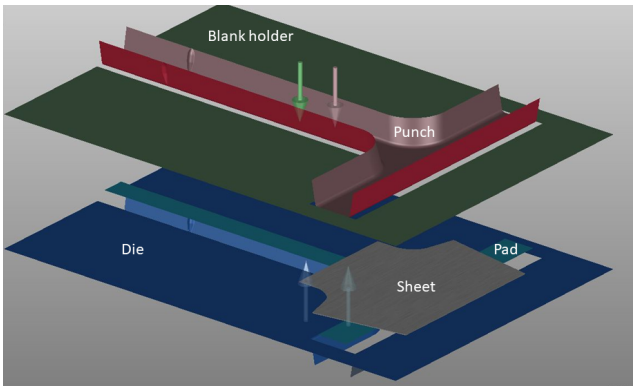

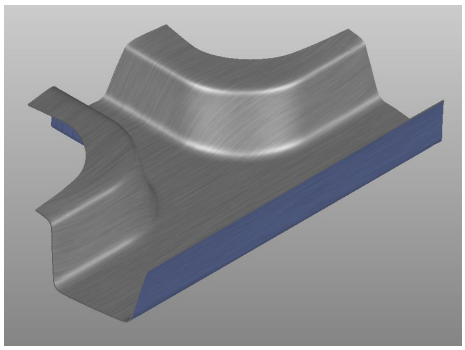

Figure 7.5: B-pillar overview of the tooling and sheet. Figure 7.6: B-pillar final product shape.

Furnace		**Sheet**		**Tool**	
Temp	930°C	Substrate	22MnB5	Material	Tool steel
Time	330 sec.	Coating	Al-Si	Finish	Polished
		S_a	1.92 μm	S_a	0.60 μm
		$Temp_{start}$	750°C	$Temp_{start}$	70°C

Table 7.1: Parameters for the B-pillar forming process used in the galling prediction.

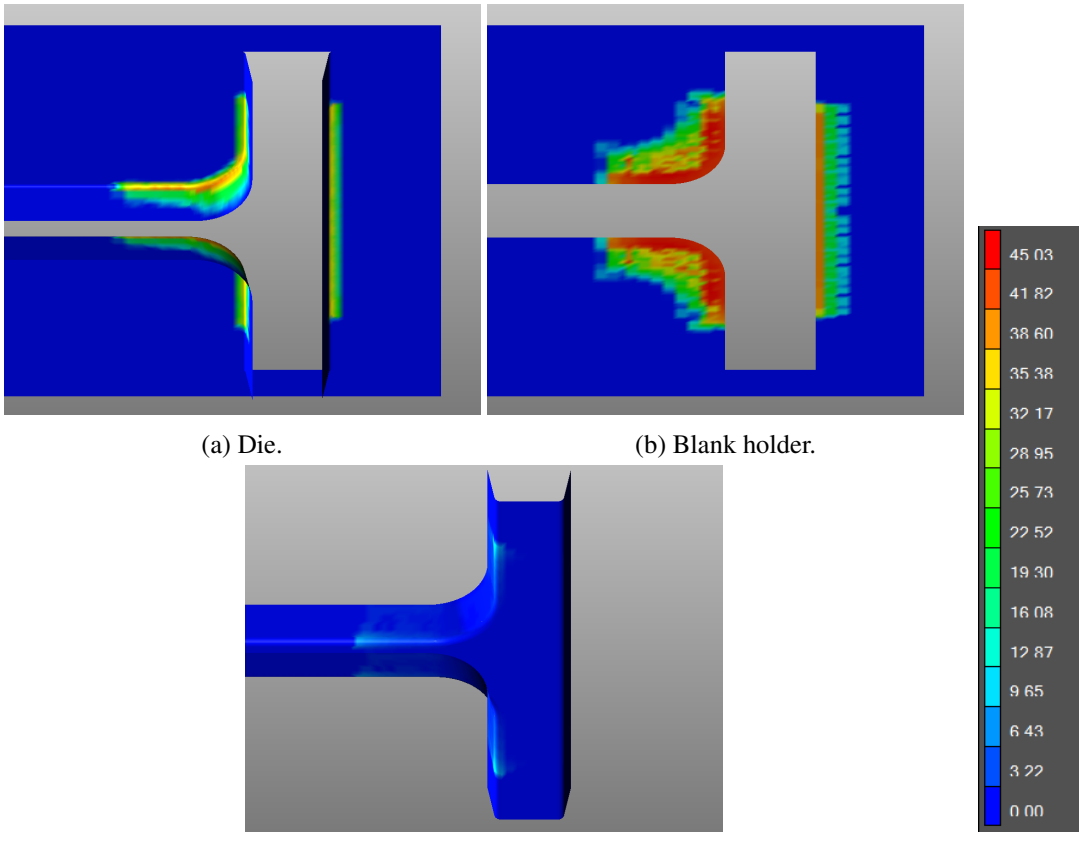

(a) Die. (b) Blank holder.

(c) Punch. All

Figure 7.7: Cumulative sliding distance after one draw [mm].

Galling is expected in these locations on the tooling, because material transfers when two surfaces are in relative motion to each other. The galling amount projected on the tool depends on the temperature, pressure and strain of the sheet during forming and on the relative sliding length between the sheet and the tool. The projection of galling amount is shown in figure 7.8 for the die, in figure 7.10 for the blank holder and the punch. Below, the difference between the galling initiation models will be discussed first and then a comparison will be made to the experiments.

Results galling amount projection

The galling is mostly predicted on the radius of the die, which is in agreement with the visual inspection of the tooling [63]. It should be noted that the scale of CFI and WFI in the projection of galling amount on the die are different (figure 7.8 and figure 7.9 for Sa = 0.6μm and Sa = 0.2μm respectively). The scale is not matched, because details on the galling projection for WFI would have disappeared. This difference in range is attributed to the different relation of adhered volume over pressure. When the higher tool roughness is applied the CFI model increases over pressure, while the WFI model is more or less constant from 15MPa to 30MPa (figure 6.4 and figure 6.5 for CFI and WFI respectively). The relation between CFI and WFI for the lower tool roughness is different. Both show an increase over pressure, but the increase for WFI is significantly lower (figure D.6 and figure D.7 for CFI and WFI respectively). Also, the difference between the scale of the galling initiation models is larger for a lower tool roughness.

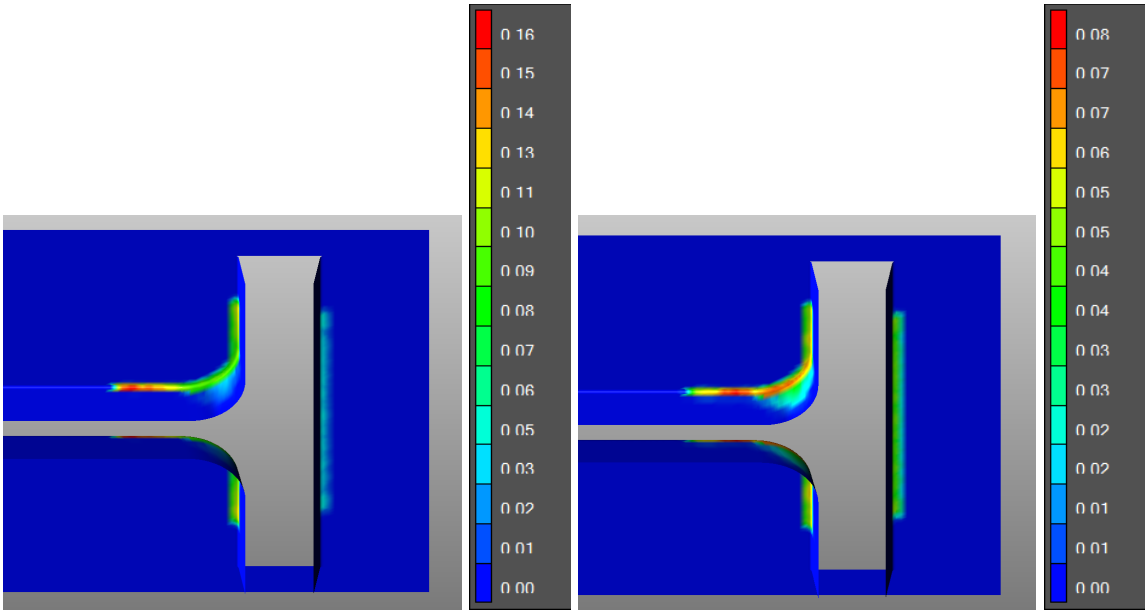

(a) Die CFI. CFI (b) Die WFI. WFI

Figure 7.8: Galling Amount ([g/mm^2]) after one draw (Sa = 0.6μm).

The highest galling amount on the die, when a tool roughness of 0.6μm is applied, is for both initiation models on the same straight edge on the long T-part, but in a slightly different location. This is traced back to the pressure and strain difference along this edge. The pressure over this straight edge shows pressures from at least 15MPa, where the edge of the product shows the highest pressure during forming. Since the pressures are 15MPa or higher the CFI model will show more adhered volume compared to the WFI model, which causes the highest galling amount locations to be slightly different. Also, the relation for adhered volume over strain enhances the observed

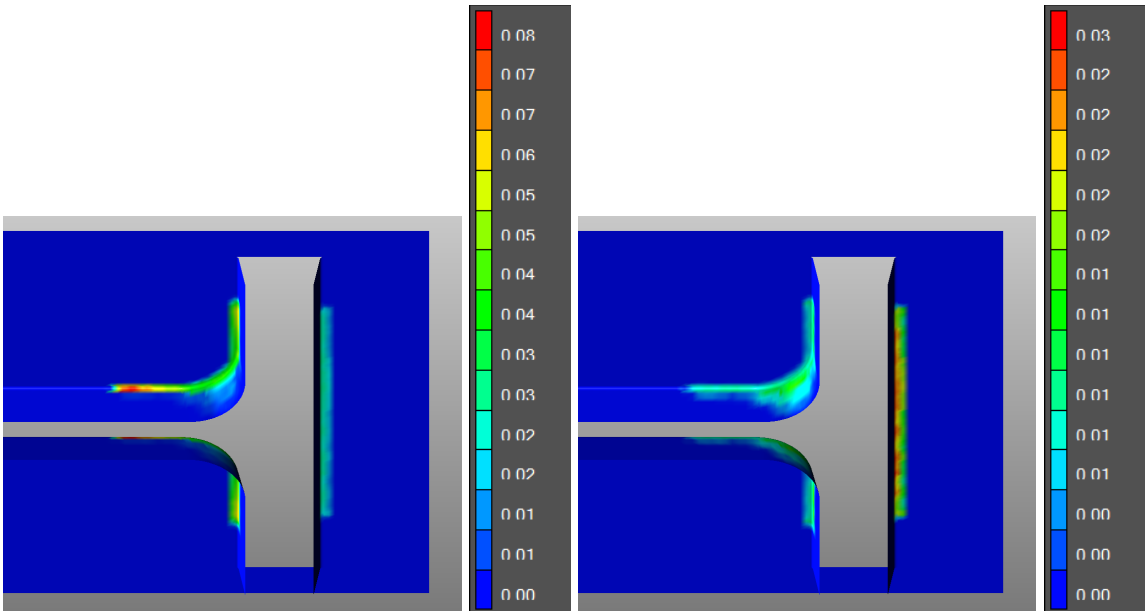

(a) Die CFI. (b) Die WFI.

Figure 7.9: Galling Amount ([g/mm^2]) after one draw (Sa = 0.2μm).

difference. The further away from the T-radius the lower the strain during deformation, where the relation for adhered volume over strain causes a decrease in volume for in increase in strain (for >5MPa). This relation is more severe for the CFI model compared to the WFI model. The highest predicted galling location for CFI is similar for both the tool roughnesses, but the highest predicted galling amount for WFI for using Sa = 0.2μm is different compared to the higher tool roughness. The CFI prediction is similar because the relation over pressure, temperature and strain is similar but less in amount. The adhered volume for WFI on the other hand does not scale down in the same manner, but scales down more compared to the CFI model. Also, the WFI model for a higher strain shows a decrease in adhered volume over pressure from 10MPa to 25MPa, where the value for adhered volume of 25MPa goes towards that of 1MPa. This combination for WFI with the lower tool roughness causes less galling amount on the T-radius compared to the straight T-top edge. The difference in predicted galling amount between the high and low roughness is attributed to the greater scale difference, which causes a smaller slope for adhered volume over pressure, and the different relation over pressure for the lower tool roughness.

According to the galling projection using WFI with Sa = 0.6μm a second highest location is observed in the T-radius (orange). The values projected by WFI ($\approx$ 0.07 g/mm^2) are actually smaller than the value of CFI ($\approx$ 0.10 g/mm^2) for Sa = 0.6μm at this position. The scale between the two models is different, which causes the orange area for the WFI model to be green for the CFI model. The galling amount in this location can be explained by the pressure range (5MPa - 15MPa) and the increasing strain, which goes up to 0.3 during deformation. At the pressure range from 1MPa to 10MPa both the CFI and WFI model are similar for the adhered volume. However, at 15MPa the CFI model will predict more galling. The difference has been minimized by the increasing strain, because the adhered volume decreases more for CFI compared to WFI when the strain increases.

The straight T-top edge on the B-pillar die show a similar amount of galling for both galling initiation models (for both roughnesses). The galling behavior is similar, because the pressure is below 10MPa during the forming process. The relation for adhered volume over pressure with a

tool roughness of 0.6μm is similar for both the galling initiation models in this range. However, the relation for adhered volume with the tool roughness of Sa = 0.2μm is only similar for <5MPa. Still, the value is similar between the two model, because the pressure values are mostly below 5MPa.

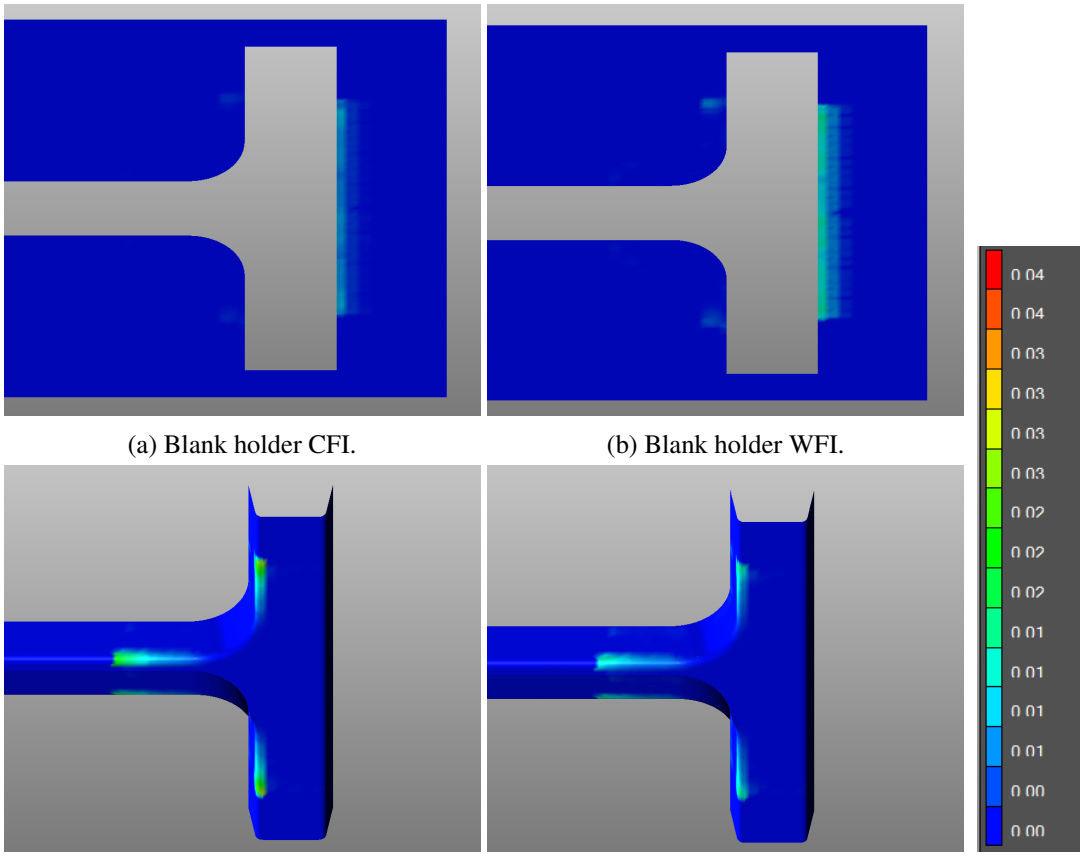

(a) Blank holder CFI. (b) Blank holder WFI.

(c) Punch CFI. (d) Punch WFI. All

Figure 7.10: Galling Amount ([g/mm^2]) after one draw (Sa = 0.6μm).

In figure 7.10 the projected galling amount for the blank holder and the punch can be seen. The scale for the galling amount has been adjusted, since less galling amount is projected on these parts compared to the die (figure 7.8). This is in agreement with the observations during the experiments [63]. On the punch galling amount has been projected on the product edges in the radius. This projection is caused by the pressure over the observed sliding length (figure 7.7c). The pressure increases during the forming process up to 35MPa. Also, the difference between CFI and WFI is attributed to the increased pressure during forming, because the adhered volume over pressure for CFI increases while the adhered volume over pressure for CFI is constant between 15MPa to 30MPa. The blank holder shows barely any galling amount, which is in line with the visual inspection [63]. On the other hand, the cumulative sliding length is very high (figure 7.7b. The predicted galling amount is low, because the pressures during deformation are very low (<1MPa). The galling amount for WFI is slightly higher because the value for adhered volume at 1MPa is higher compared to CFI (figure 6.4 and figure 6.5 for CFI and WFI respectively) and therefore the linear relation from 0MPa to 1MPa provides a higher value for the same applied pressure.

7.2.4 Comparison prediction to measurements

Comparing the predicted galling amount to the experimental confocal measurements provides some differences. According to the measurements the most severe galling location should be observed on the straight T-top edge of the B-pillar, which shows the lowest galling amount compared to the other edges on the die for CFI and WFI with Sa = 0.6μm and CFI with Sa = 0.2μm. In the galling projection the lower predicted galling amount is due to the low pressures ($<$10MPa) during formation. The exact cause for the difference between the experiment and prediction is not known. This could indicate 1) that the geometry is different in reality compared to the simulation, 2) that the measurement location on the radius is different compared to the other measurement locations or that 3) the location is an outlier, since only one location on the straight T-top edge has been included in the measurements. The situation for WFI with Sa = 0.2μm does predict more galling amount on the straight T-top edge, which is in line with the experimental confocal measurements. This is not a distinct difference, because the scale is reduced to show the details. Still, a single location at the straight T-top radius has been used for the experimental confocal measurements, which could be a different location on the radius or an outlier.

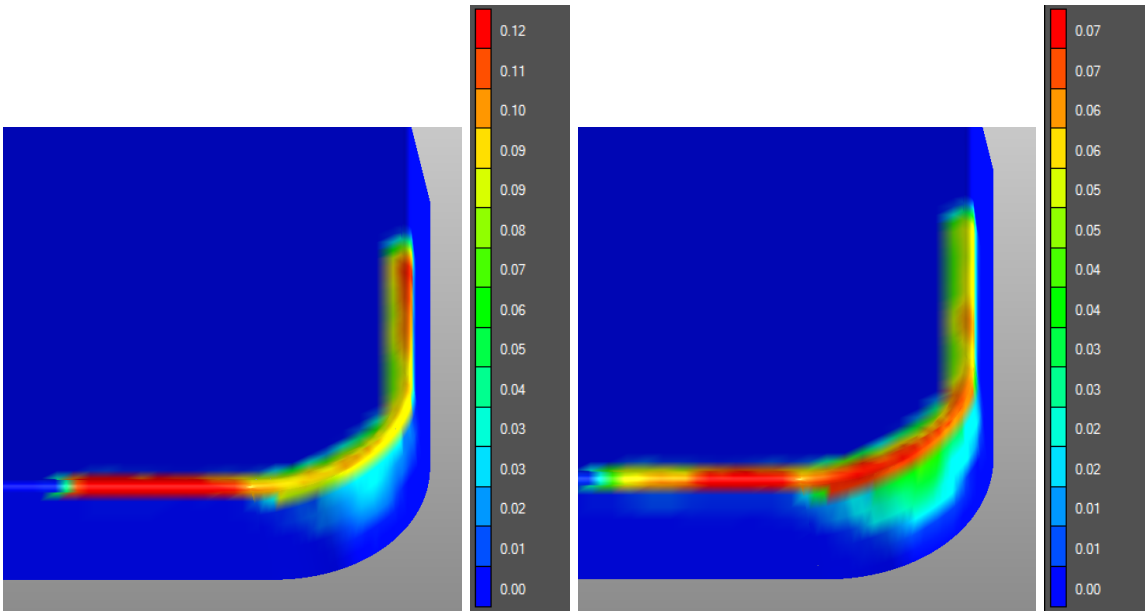

(a) Die CFI. CFI (b) Die WFI. WFI

Figure 7.11: Galling Amount ([g/mm^2]) after one draw zoomed in on the T-radius of the die (Sa = 0.6μm).

Multiple confocal measurements have been performed on the T-radius, where location 1 and 3 have a similar build up over 50 draws and location 2 shows less galling build up compared to location 1 and 3. Looking at the galling amount projection using CFI, the location 1 and 3 show a similar prediction, while location 2 has a little bit less galling amount compared to location 1 and 3 on the die (figure 7.11a and figure 7.12 for Sa = 0.6μm and Sa = 0.2μm respectively). Since, the projected galling amount is after one draw the difference over 50 draws would increase, which makes that the galling projection using CFI is in agreement with experimental observations based on these three points. However, the measurement on location 4 should have the same amount of galling to location 1 and 3 according to the experimental confocal measurement, which is not the case. The CFI model predicts more galling amount for a location further away from the T-radius.

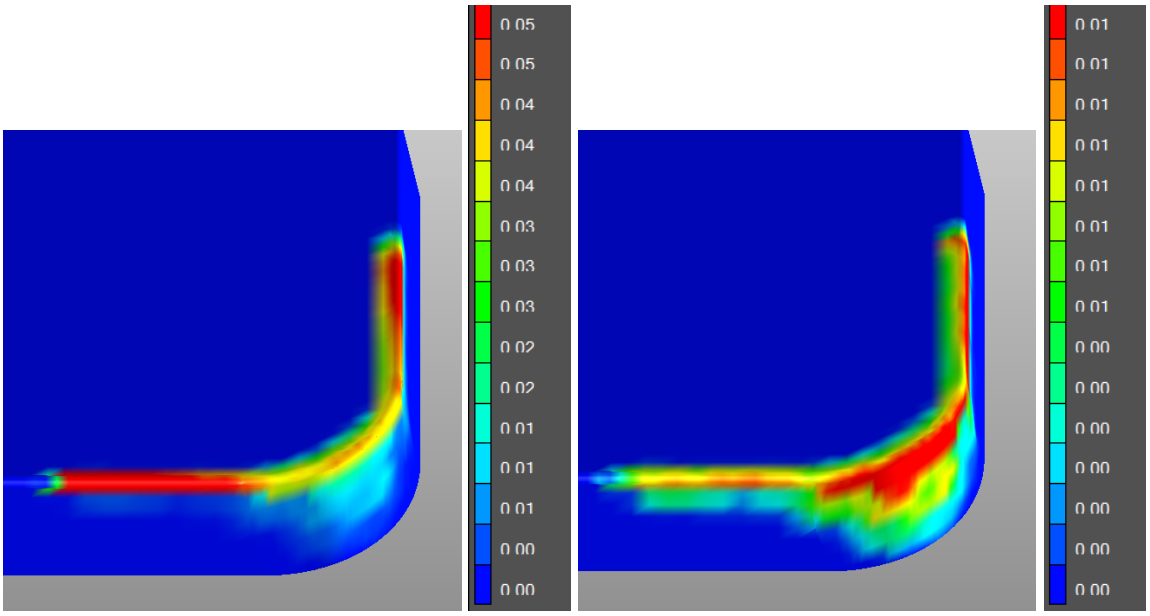

(a) Die CFI. CFI (b) Die WFI. WFI

Figure 7.12: Galling Amount ([g/mm^2]) after one draw zoomed in on the T-radius of the die (Sa = 0.2μm).

The WFI model (both roughnesses) does show similar results as the (barely) yellow areas on the die radius, which could indicate location 1, 3 and 4. The location for the confocal measurements could have skipped over the more severe area according to the WFI model and cause similar results for the confocal images, since a confocal image is a very local measurement. However, the exact location is not known. The WFI model does show more galling amount on location 2 compared to location 1 and 3 (figure 7.11b and figure 7.12b for Sa = 0.6 μm and Sa = 0.2 μm respectively), which contradicts the experimental observation.

According to the confocal measurements of the punch no galling is observed. Also, on these location on the punch no galling is predicted. However, some galling amount is projected on the punch at the edges of the product. This location was not included in the experimental measurement and can therefore not be verified. Still, the predicted values for galling amount are significantly smaller compared to the die and therefore might not stand out as galling build up in a measurement.

7.3 Industrial parts Volvo Cars

7.3.1 A-pillar

Introduction to the forming setup

This validation case does not include experiments, but relies on the feedback concerning the location of galling based on expertise and experience at Volvo Cars [64]. The A-pillar is a more complex part than the B-pillar in the previous section. The final product shape is shown in figure 7.14 and the tooling for the A-pillar, as it will be applied in the AutoForm simulation, is shown in figure 7.13.

The tribological system from the calibration will be used to project galling onto the A-pillar part. This is an initial galling projection to see how well the galling model performs when it is applied to an industrial part. For future reference, the system should be improved with the

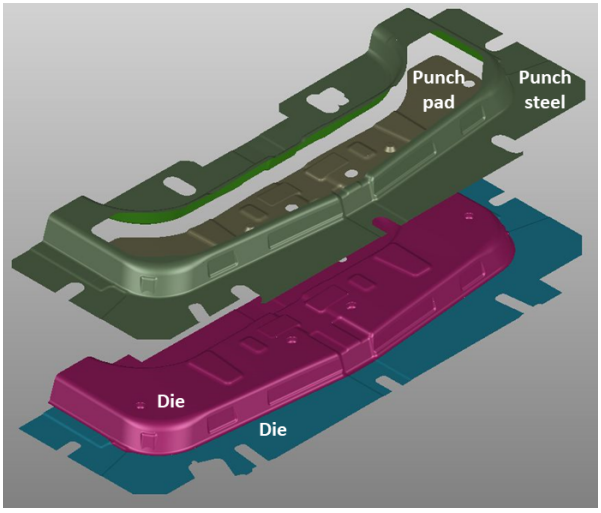

Figure 7.13: A-pillar overview of the tooling.

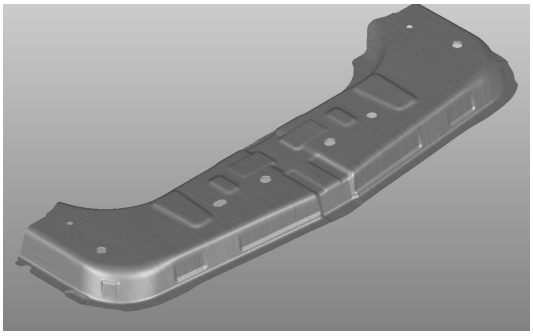

Figure 7.14: A-pillar final product shape.

use of the real 3D surface measurements of the tool to get a more accurate approximation. The parameters applied for the galling projection onto the A-pillar are shown in table 7.2. Here, the transport time from heating to the start of forming is indicated instead of the starting temperature, because this is in line with the flow of the industrial production part. The $\text{Temp}_{\text{start}}$ for the tooling is the tool temperature at the start of the production batch and will remain constant in the AutoForm simulation. In reality, the temperature of the tooling changes over multiple forming processes.

Furnace		**Sheet**		**Tool**	
Temp	930°C	Substrate	22MnB5	Material	Tool steel
		Coating	Al-Si	Finish	Polished
		S_a	1.92 μm	S_a	0.60 μm
		$\text{Time}_{\text{transport}}$	8 sec	$\text{Temp}_{\text{start}}$	80°C

Table 7.2: Parameters for the A-pillar forming process used in the galling prediction.

The cumulative sliding length is the relative displacement between the tool and the sheet after one draw while in contact. This sliding length is projected on the tools in figure 7.15 for the punch steel (two views), the die and the punch pad. Galling can be expected in these contact locations on the tooling. The sliding length on the light blue part of the die (figure 7.13) is not correct, because a gap controlled binder is applied (not shown). This part moves during the forming process and cannot be simulated correctly at this point. The contact of the tooling with the sheet is mainly on the radii, which is especially clear for the punch. The prediction of galling amount projected on the tool depends on the temperature, pressure and strain of the sheet during forming and on the relative sliding distance in contact between the tool and the sheet. The projection of galling amount on the A-pillar tooling is shown in figure 7.16 for two views of the punch steel and figure 7.17 for the die and the punch pad.

Results galling amount projection

The locations in reality where galling is observed, are the outer radii on punch steel of the A-pillar tooling, which are correctly predicted with the galling model. The galling amount projection can be seen in figure 7.16, where the galling location is indicated with a white box. In the projection of

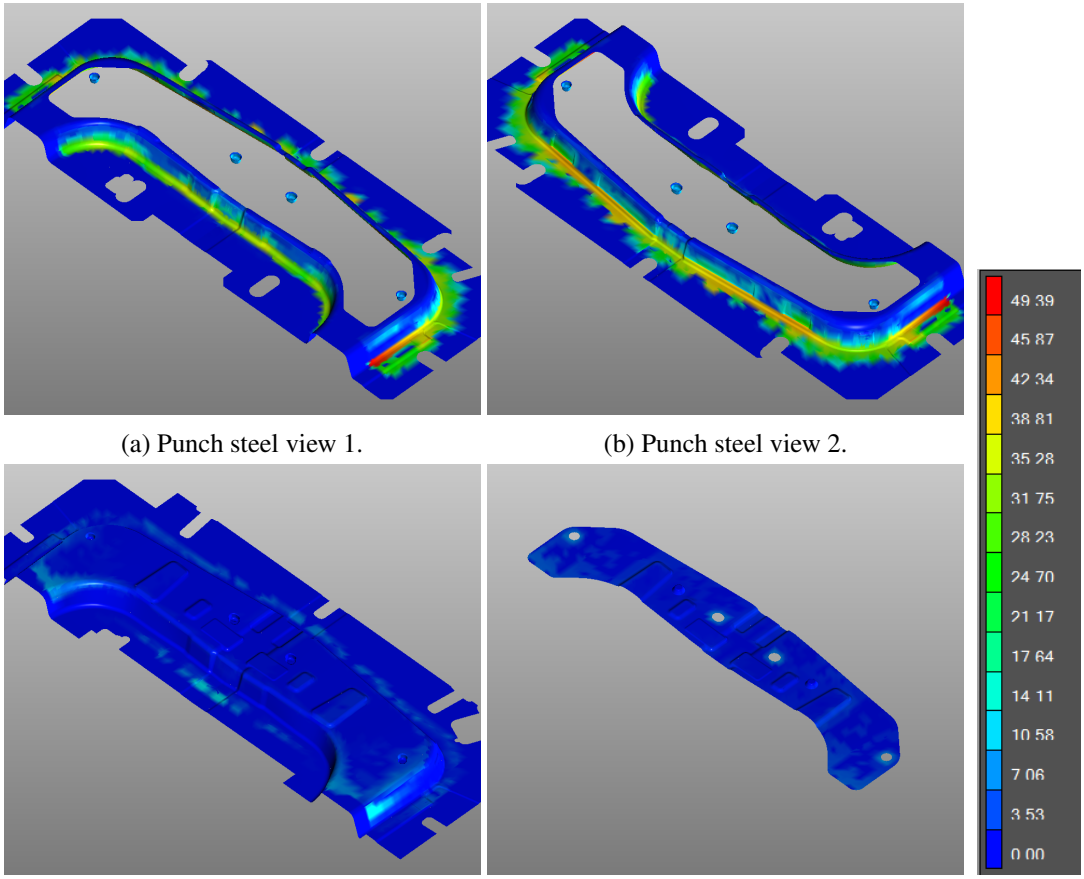

(a) Punch steel view 1. (b) Punch steel view 2.

(c) Die. (d) Punch pad. All

Figure 7.15: Cumulative sliding distance for one draw [mm].

galling amount on the punch steel there is a difference in the scale for galling amount. The range in the scale has not been matched, because the details on the A-pillar using the WFI model would have disappeared. The range difference is due to the difference in adhered volume over pressure, figure 6.4 and figure 6.5 for CFI and WFI respectively. The highest predicted value for galling amount after one production cycle (the red spots) for both galling initiation models is seen on the punch steel at the edge of the part on the inner radius, see figure 7.16a and figure 7.16c for CFI and WFI respectively. On these locations no significant difference in sliding length can be seen compared to the neighboring edges. Also, no differences with the neighboring edges based on pressure, strain and temperature are observed. Therefore, these locations are attributed to a numerical error during the projection on the tooling. In the case of the CFI model another red spot can be seen on the outer radius of the punch steel, figure 7.16b. This outer radius is the correct location regarding galling, but in the engineers at Volvo Cars no specific spot on the outer radius has been observed to exhibit more galling. This red spot on the outer radius is therefore also attributed to a numerical error during the projection on the tooling, which is most likely to do with the pressure. Since the galling behavior shows more build up on the outer radius of the A-pillar a difference with the inner radius should be expected. For the A-pillar projection using CFI this difference is more clear compared to the use of the WFI model. This difference is due to the difference in predicted galling amount for higher pressures (15-30MPa). In the WFI model the pressure barely influences the galling amount whereas the CFI shows an increase of galling amount for higher pressures. When comparing the

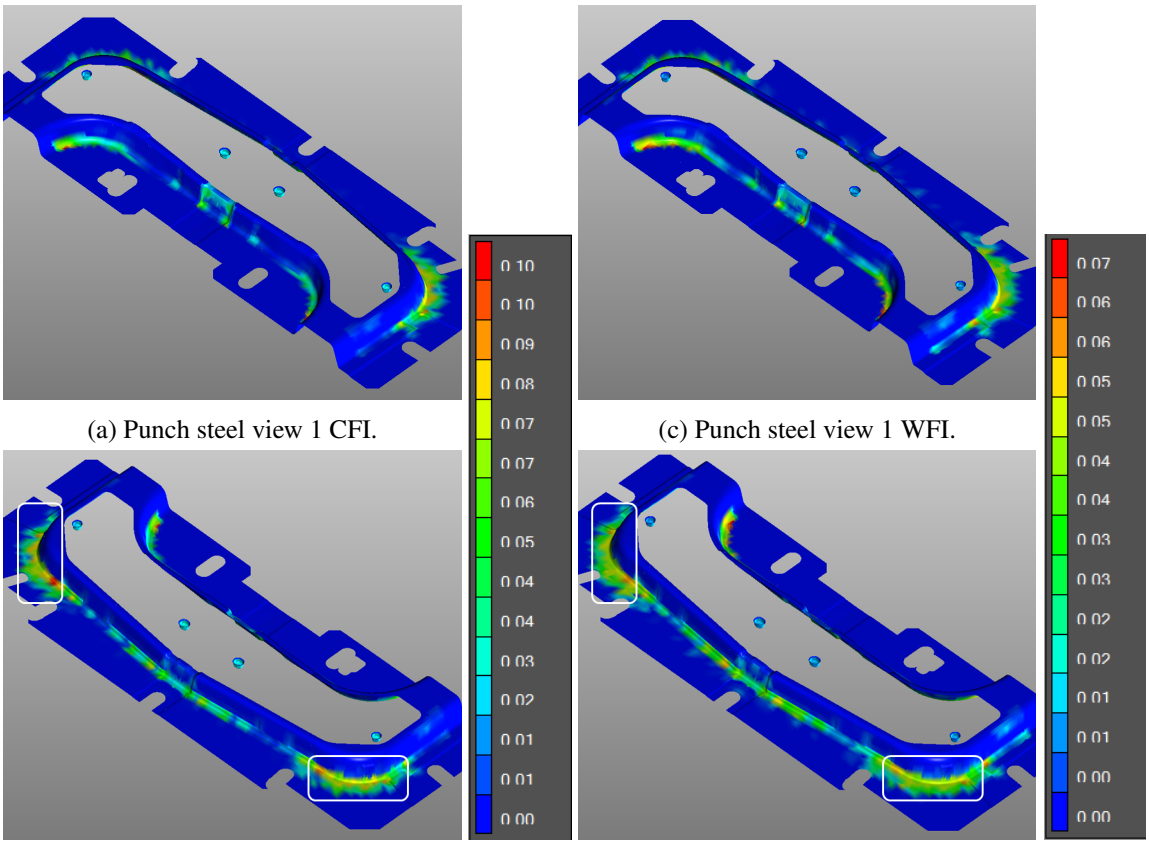

(a) Punch steel view 1 CFI.

(c) Punch steel view 1 WFI.

(b) Punch steel view 2 CFI.

CFI

(d) Punch steel view 2 WFI.

WFI

Figure 7.16: Galling Amount ([g/mm^2]) after one draw.

predicted galling amount to the figure showing the cumulative relative sliding distance it is noted that the highest sliding length value barely shows any galling amount. This is due to the low pressures (<5MPa) during the forming process.

It can be seen that on the punch pad and on the die the galling amount, figure 7.17, is less compared to the punch steel, figure 7.16. This is in accordance with the information from the engineers at Volvo Cars [64]. The difference between these tooling parts it attributed to the difference in cumulative sliding distance, because the sliding length for the die and the punch pad is significantly less than the sliding length of the punch steel. The projection on the light blue part of the die (figure 7.13) is not correct, because a gap controlled binder is used, of which the movement during forming cannot be correctly simulated at this point. The CFI model shows more galling on the punch pad compared to the WFI model. Again, this is due to the difference in galling amount over pressure. The CFI model provides more adhered volume when a higher pressure is applied, while the WFI model shows similar galling amounts compared to the lower pressures (figure 6.4 and figure 6.5 for CFI and WFI respectively). On the die the predicted galling amount is more similar, because the pressure ranges from 0MPa to 10MPa which shows a comparable relation of galling amount for pressure over temperature.

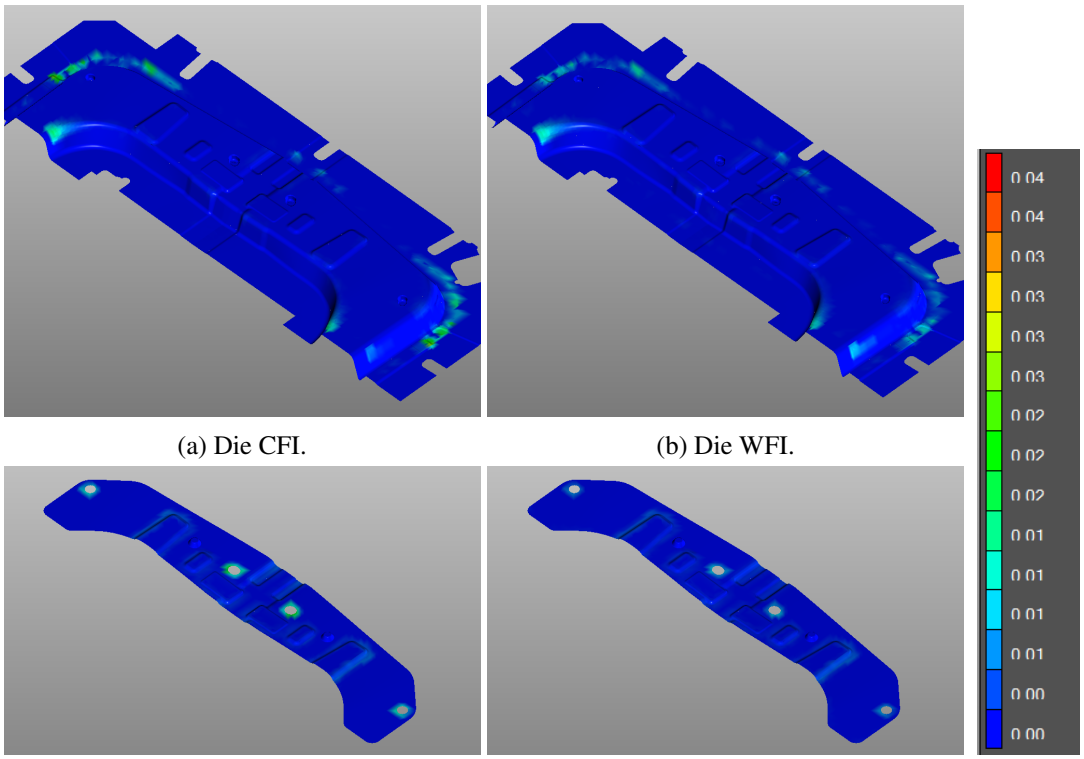

(a) Die CFI. (b) Die WFI.

(c) Punch pad CFI. (d) Punch pad WFI. All

Figure 7.17: Galling Amount ([g/mm^2]) after one draw.

7.3.2 Side Member

Introduction to the forming setup

This validation case does also not include experiments, but relies on the feedback concerning the location of galling based on expertise and experience at Volvo Cars [64]. The Side Member is a complex part, which uses different tool temperatures during forming. The product shape before cutting is shown in figure 7.19 and the tooling, as it will be applied in the AutoForm simulation, is shown in figure 7.18.

Again, this is an initial galling projection to see how well the galling model performs when it is applied to an industrial part. For future reference, to improve upon the galling projection for this specific case, the sheet and tool topographies should be accounted for. The parameters for galling projection onto the Side Member are shown in table 7.2. Here, the transport time from heating to the start of forming is indicated instead of the starting temperature, because this is in line with the flow of the industrial production part. The $\text{Temp}_{\text{start}}$ for the tool is the temperature at the start of the production batch and will remain constant in the AutoForm simulation, while in reality the temperature changes over multiple forming processes. Also, multiple $\text{Temp}_{\text{start}}$ for the tooling is applied, which are allocated to the correct tool part in table 7.4.

The cumulative sliding length is shown in figure 7.20 for the punch steel, the punch pad and the die. Galling can be expected in these contact locations on the tooling. The sliding length on the die pad (the light blue tooling part in figure 7.13) is not correct, because this die part moves during the forming process, which cannot be simulated correctly at this point. The relative sliding distance of the tooling with the sheet is mainly on the radii, which is especially clear for the punch steel and for some locations on the die. This is as expected, because the sheet will get folded around the die,

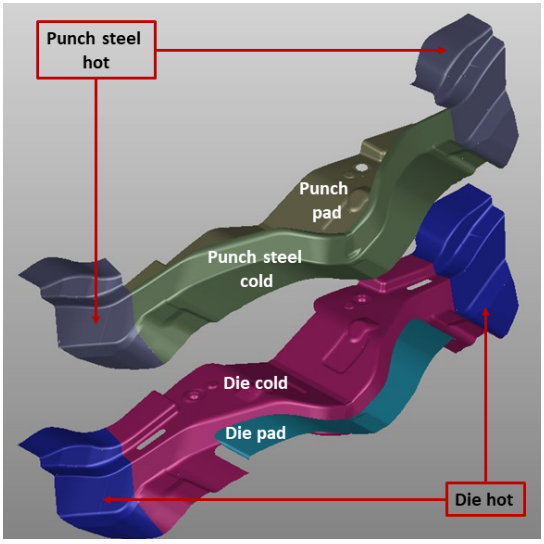

Figure 7.18: Side member overview of the tooling.

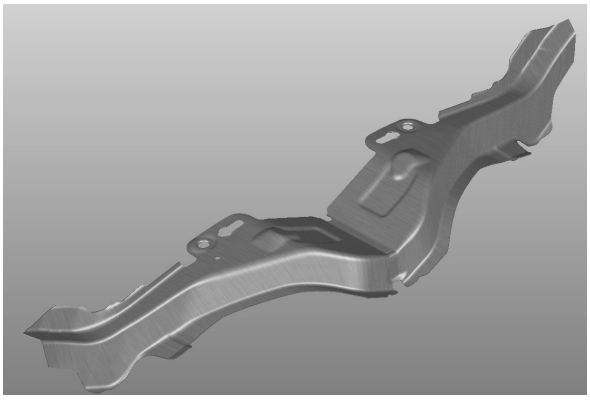

Figure 7.19: Side member product shape before cutting.

Furnace		**Sheet**		**Tool**	
Temp	930°C	Substrate	22MnB5	Material	Tool steel
		Coating	Al-Si	Finish	Polished
		S_a	1.92 μm	S_a	0.60 μm
		$Time_{transport}$	8 sec	$Temp_{start}$	20°C , 80°C and 525°C

Table 7.3: Parameters for the Side Member forming process used in the galling prediction.

Tooling	**Temperature**
Punch steel hot, Die hot	525°C
Die pad	80°C
Punch steel cold, Die cold, Punch pad	20°C

Table 7.4: Tooling temperatures.

while the punch steel slides the sheet into the product geometry. The galling projected on the Side Member tooling can be seen in figure 7.21 for the punch steel and in figure 7.23 for the die and the punch pad.

Results galling amount projection

According to the engineers at Volvo Cars, the side member part suffers from severe galling [64]. This has been correctly allocated on the punch steel by both the galling initiation models, which is indicated with a white box in figure 7.21 and can be seen on the tooling in figure 7.22. The severe galling location is where the tooling is heated to 525°C . This high tool temperature is not directly applied within the galling model, but the tooling temperature does influence the sheet temperature, which is used to predict the galling amount per time increment. This position suffers from galling due to the long sliding distance compared to its neighboring edges, because the combination of pressure, temperature and strain does not indicate severe galling. The pressure in this location is mostly kept below 15MPa. The temperature is high, but not significantly different compared to

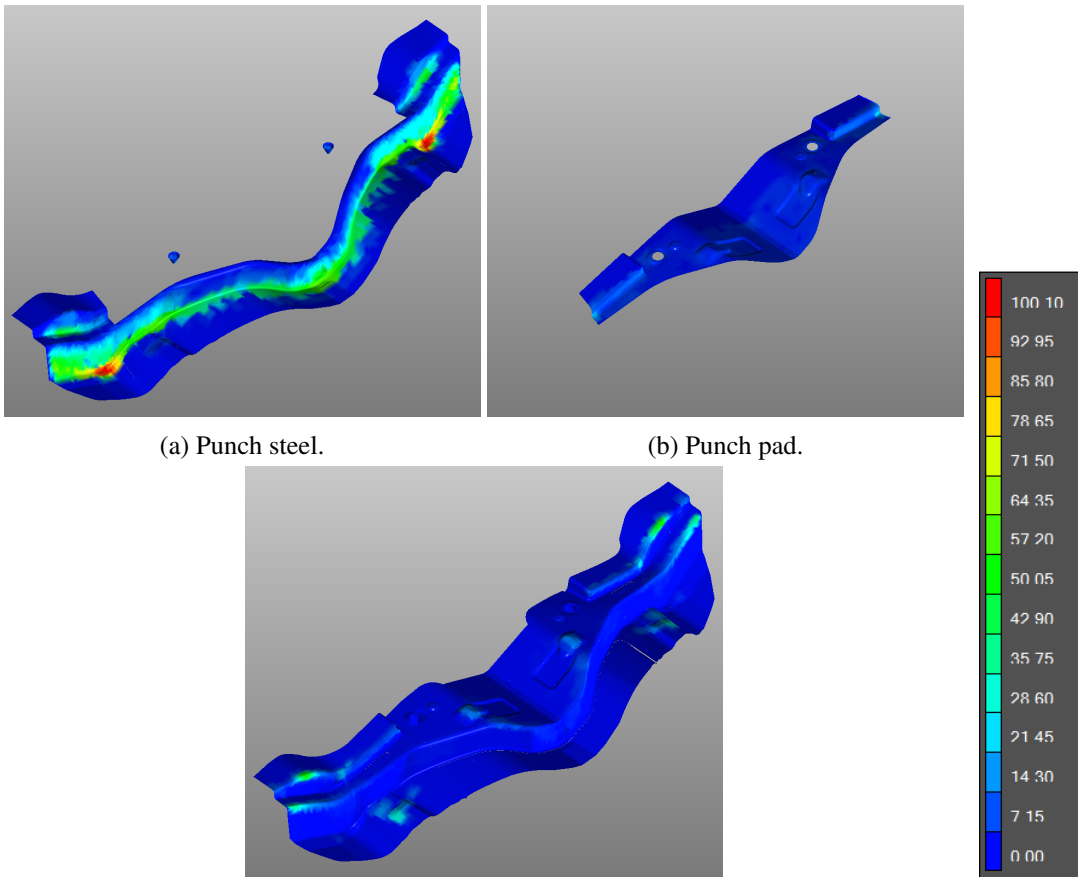

(a) Punch steel. (b) Punch pad.

(c) Die. All

Figure 7.20: Cumulative sliding distance after one draw [mm].

the other surrounding points. The strain during deformation is in between 0 and 0.5, which is higher compared to surrounding points. According to the relation for adhered volume over strain the volume decreases for higher values of strain (for $>$ 5MPa). Therefore, the strain does not suggest a higher galling amount. A second highest predicted galling amount can be observed on the punch steel, indicated with a red box. At this location the relative cumulative sliding length is similar to the neighboring point. Also, the pressure and temperature is comparable to the rest of the edge of the 'Die cold steel'. However, the strain of the side edge of the 'Die cold steel' is lower compared to the center edge of the 'Die cold steel'. A lower strain for the same pressure and temperature provides a higher galling amount. Hence, the center is just colored green, while the indicated position also hints towards yellow. This is not confirmed with reality, since the severe galling position (white box) is more dominant and a higher concern. Even though, the same galling locations have been established using either CFI or WFI, a significant difference for the highest galling amount is observed. This is attributed to the different relation for galling amount over pressure (figure 6.4 and figure 6.5 for CFI and WFI respectively), where CFI shows an increase over pressure from 10MPa to 30MPa, while WFI shows more or less a constant relation for galling amount over pressure from 15MPa to 30MPa.

The punch pad and the die do not suffer from galling according to figure 7.23, which is in line with the experience from the engineers at Volvo Cars. The predicted galling locations are similar for both applied galling initiation models, where CFI predicts more galling amount at the punch

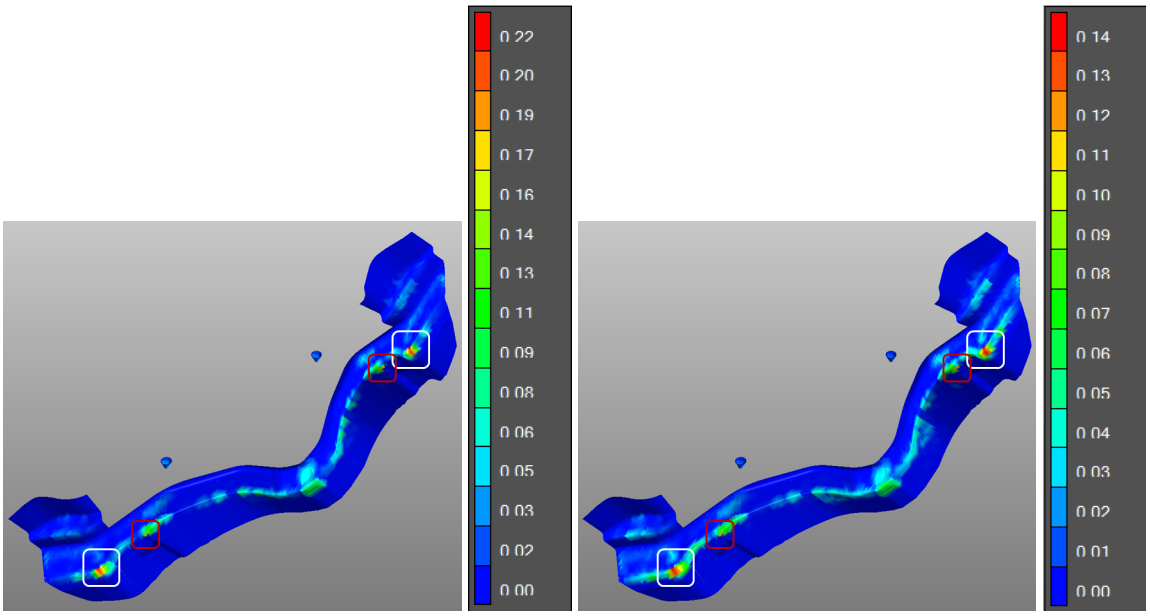

(a) Die CFI. CFI (b) Die WFI. WFI

Figure 7.21: Galling Amount ([g/mm^2]) after one draw.

Figure 7.22: Severe galling on Side Member (white box) [64].

pad compared to WFI and where WFI shows more galling amount at some locations on the die. The galling projection onto the die pad (light blue tooling part in figure 7.18) is not correct, because the movement of this tooling part cannot be correctly simulated at this point. The higher values for galling amount on the punch pad are attributed to the higher pressures ($>$10MPa) during the forming process. The relation for adhered volume using WFI over pressure is more or less constant, while the adhered volume using CFI increases over pressure. The spot with more galling amount using WFI on the die is due to the low pressures ($<$5MPa) during forming. The adhered volume for these low pressures is more dominant in WFI compared to CFI, which causes more build up of galling amount using WFI.

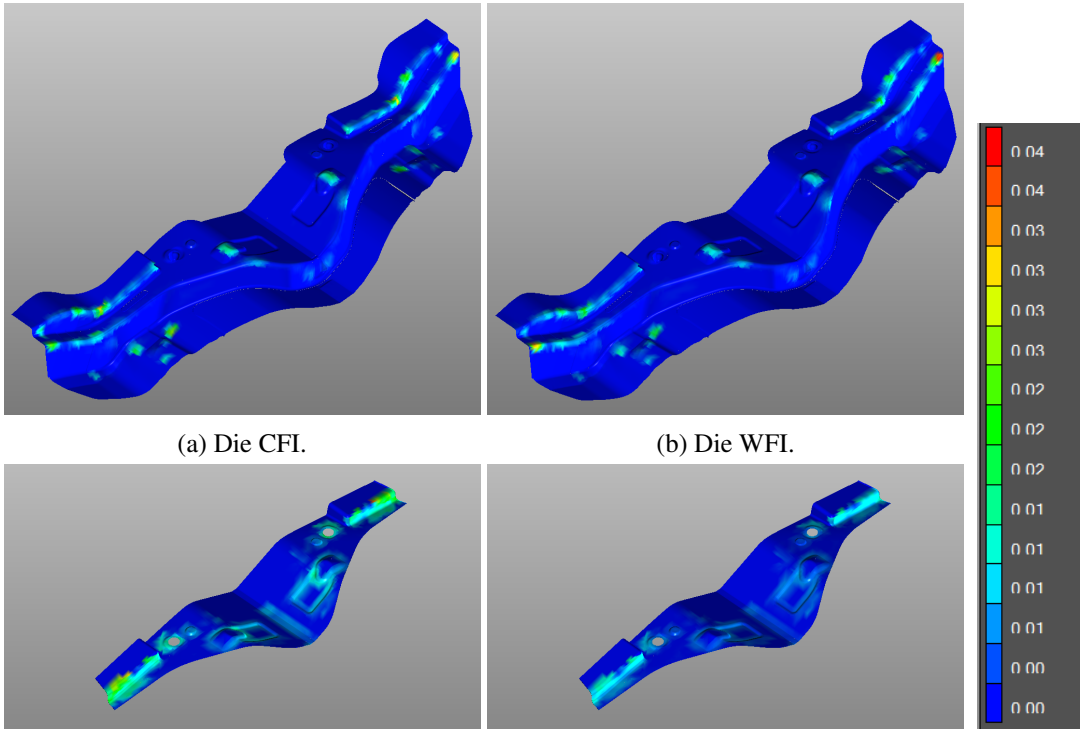

(a) Die CFI. (b) Die WFI.

(c) Punch pad CFI. (d) Punch pad WFI. All

Figure 7.23: Galling Amount ([g/mm^2]) after one draw.

7.3.3 Comparison industrial parts

The Side Member has a higher predicted galling amount compared to the A-pillar. This is in accordance with the experience from Volvo Cars, since the A-pillar does not show severe galling, but the Side Member does. On the A-pillar some galling build up can be observed on the tooling after a production batch (1500 parts), but does not cause major problems during the forming process [64]. However, the tooling is regularly cleaned during maintenance operations to prevent galling behavior over multiple batches. On the other hand, the Side Member has a smaller production batch ($\approx$ 300 parts), because galling is so severe that the products will be damaged if the process continues [64].

The galling amount predictions do show more galling on the Side Member, which is in accordance with the experience at Volvo Cars, but the ratio between the A-pillar and Side Member is not significant enough. The ratio is calculated using the equation below and comes down to a ratio of R_{CFI} = 0.22/0.10 = 2.2 and R_{WFI} = 0.14/0.07 = 2.0. The exact ratio in reality is not known, but should be higher based on the amount of parts in a production batch. This indicates that the galling behavior for the A-pillar might be overestimated or that the galling behavior for the Side Member might be underestimated.

$$\text{Ratio} = \frac{\text{Highest galling amount Side Member}}{\text{Highest galling amount A-pillar}} \tag{7.1}$$

The ratio between the industrial parts using the CFI model and WFI model, calculated according to equation 7.1, is different, where the CFI shows a bigger difference. This higher ratio is attributed to the fact that CFI shows an increasing relation for adhered volume over pressure, while WFI shows about a constant relation of adhered volume over pressure for 15MPa till 30MPa. The

galling model using CFI seems to be more favorable based on the information from the industry and the higher predicted galling amounts according to the CFI model.

7.4 Summary

- The galling prediction for the experimental B-pillar is in line with visual observations from Tata Steel. Galling is observed on the die radii and no significant galling is found on the punch or blank holder. However, a difference for the galling on the die between the straight T-top edge and the T-radius has been observed. The prediction shows less galling amount on the straight T-top edge, while the experiments show more galling on the straight T-top edge (location 5). The origin of this difference is not exactly known. Using the CFI model when comparing the multiple measurements of the T-radius (location 1, 2 and 3) provides a better approximation to the experiments than the WFI model.

- The first iteration of the galling model has predicted the correct location for galling on the A-pillar as well as the Side Member. However, the severity of the predicted galling amount is not exactly known, because the ratio between the A-pillar and Side Member does not seem sufficient enough. The CFI model is more favorable compared to the WFI model based on the information the industry on the severity of galling and the ratio of the highest galling amount between the Side Member and the A-pillar.

- The galling amount is not verified. Therefore, the B-pillar and the industrial parts can not be compared, because the severity of galling between the B-pillar and the industrial parts is not known. This should be verified in more detail. A combination of confocal and line measurements over a test radii, to determine an adhered volume like in section 4, should improve upon the location comparison. Also, this provides a link between the observed galling to the predicted galling amount.

- The CFI model is more favorable compared to the WFI model based on the comparison of the two industrial parts and based on the comparison of the B-pillar prediction to the confocal measurements. In addition, the CFI model shows an increase of adhered volume over pressure, which is more in line to findings in literature, while the WFI model is more or less constant from 15MPa to 30MPa.

8 Conclusion

Galling model & Results

A model has been implemented to predict galling behavior in hot sheet metal forming. This includes a galling initiation model, a lump growth model and a multi asperity model. Two criteria have been proposed to initiate asperities for galling, the wedge formation initiation (WFI) and the coating fracture initiation (CFI). The WFI model is based on wear mode diagram developed by Challen and Oxley, which is developed based on 2D slip-line field assuming plane strain deformation and ideal plastic behavior. The CFI model uses the plane strain fracture toughness of the coating as a threshold for galling initiation of an asperity. From these two, the CFI model is more favorable, because the WFI model only relies on the wear modes, which undergo multiple assumptions to go from a cold 2D situation to a hot 3D situation.

The amount of identified contact asperities depends on pressure, temperature and strain. These parameters change the amount, shape and size of asperities in contact. The WFI criterion is independent of pressure, temperature and strain, while the CFI criterion depends on the pressure and strain. This is reflected in the amount of asperities initiated for galling and in the adhered volume due to the initiation criterion. An asperity initiated in the WFI model grows more quickly compared to an asperity initiated according to CFI (at 5MPa), because the similar amount of material needs to be divided over less asperities. The interaction has been identified based on the overlap between asperities during growth. A significant overlap has been identified (40% for WFI and 80% for CFI). The effect of galling on friction is included in a separate multi asperity model, which updates the tool topography and then recalculates the coefficient of friction. In general this shows an increase in COF for CFI and a decrease in COF for WFI. The correct relation for COF over sliding length is not verified in this research.

Experiments & Calibration

The experimental data from Tata Steel is processed by using the average of the unworn part of the line measurement as a reference in the confocal measurement to get the adhered volume. The experimental data that does not provide a suitable correlation between the line measurement and confocal measurement is excluded from the calibration. The abrasive wear influences the perceived adhered volume, but the exact amount is not known. The measurements at 750°C are excluded from the calibration, because it provides a relation that contradicts findings in literature. The galling model is calibrated for the adhered volume by the fraction m as a function of only temperature at 5MPa and 0 strain. The galling model is valid for 500°C to 700°C .

Validation

The model has been extended over pressure (0MPa - 30MPa) and strain (0.0 - 0.4) compared to the values used in the calibration to see how well it performs. The galling amount projection only shows galling amount after one draw. The galling locations on the B-pillar have been identified on the die radius. The comparison between radius location on the B-pillar for CFI is more favorable compared to WFI. The galling locations on the A-pillar and Side Member have been accurately allocated. The CFI model is more favorable based on the galling amount ratio between the two industrial parts.

9 Recommendations

Galling model & Results

- The lump growth model within the galling model is developed for cold forming purposes. The assumptions used in the model are not necessarily valid for hot forming. Therefore, to ensure the validity of the lump growth model for hot forming the assumptions need to be checked (for example the COF based on the wear modes from Challen and Oxley, the use of Archards wear equation for worn volume and the adhesion energy for metal at elevated temperature).

- The coating fracture initiation model assumes a fixed fracture toughness based on the plane strain fracture toughness of a coarse grained Fe_2Al_5 compound layer at room temperature. The compound layer can vary based on the austenitization process before deformation, which can cause a different fracture toughness. The galling model is applied for high temperatures. Therefore, the fracture toughness, applied in the coating fracture initiation (CFI) model, might very well be different for the elevated temperatures. In addition, the plane strain fracture toughness relation holds for brittle fractures, which is less valid for high temperatures. The fracture toughness should be verified, because a variation in the fracture toughness influences the amount of initiated asperities and therefore the adhered volume.

- In addition, the coating fracture initiation model is based on the coating surface cracking according to mode I *opening mode*, because it is the most common. However, the *sliding mode* (mode II) and the *tearing mode* (mode III) or a combination of the three modes can also happen during relative sliding contact. It should be investigated if the galling initiation for CFI based on mode I cracking is a sufficient criterion.

- The initiated asperities in the galling model do not interact in the multi asperity situation. In section 6.3.2 it is shown that the asperities in the model will significantly overlap during growth. This should provide merging of asperities. This effect should be included to predict a more accurate surface change and to improve the growth model. Also, this would be a natural way of reducing the amount of adhered material over sliding length, because adhered material is determined per galling initiated asperity.

- Other aspects of multi asperity interaction are not included in the galling model like the direction dependent asperity contact and the fracture of asperities during growth. The direction dependent asperity contact, which causes less available material for asperities that come in contact later, is a more direct phenomenon compared to the fracture of a growing asperity, which needs time to build up to the point that the forces are too great. Of these two the direction dependent asperity contact should be included first and then the asperity fracture can be considered.

- In literature a distinction has been made between adhesive galling and compaction galling, while the model only describes adhesive galling and calibrates for both, since the experimental data cannot make a distinction. For future reference more research on the occurrence of the two types of galling is needed. From that it should be evaluated if a distinction between the adhesive galling and compaction galling is a useful addition and expansion to the galling model.

- The galling model has been implemented to check the effect of galling onto the COF. The relation of COF over sliding length for CFI and WFI is different compared to each other.

However, this relation has not been studied in this report. Additional research should be done to validate the correct relation. Also, for large sliding steps and a long total sliding length issues occur in the current implementation, because asperities cannot be identified as an initiated asperity anymore (using WFI) or the fractional real contact area becomes too large (using CFI). The model should be improved to include the effect of galling on the COF for extended sliding lengths without errors.

Experiments & Calibration

- The adhered volume from the model is determined by taking a fraction of the worn volume. However, the worn volume is not verified. Thus, the adhered volume is calibrated based on an assumed worn volume. The worn volume should also be verified to have less uncertainties in the model. In section 2.5 it is shown that the wear rate (k_w), which is used to calculate the worn volume, should be varied when applied for hot forming processes [47, 49].

- The experiments used for the calibration suffered from an alignment error, which caused a higher applied force on line b compared to line a. Also, only a single strip draw test per parameter set has been performed. The experiment set should be redone to supplement and verify the used measurements.

- The galling model developed in this report is valid from 500°C to 700°C . Additional experiments should be performed to extend the temperature range of the galling model for higher and lower temperatures.

- The pressure dependent relation of adhered volume (galling) could not be included because the measurements for 2.5MPa do not provide a suitable correlation between the line measurement and confocal measurement, Strip draw experiments should be performed using another pressure than 5MPa to include a pressure dependent relation.

- The strain dependent behavior for adhered volume implemented in the model is due to the inclusion of strain at the contact model. The galling model itself deals with the contact change due to strain, but does not include a strain effect directly in its initiation criterion. The effect of strain on galling initiation should be verified with further research.

- According to findings in literature, the adhesive wear also depends on the relative velocity. Here, the effect of relative velocity is not included. Experiments should be done to incorporate the velocity effect.

- In the B-pillar validation case a different tool roughness, compared to the tool roughness of the calibration, is applied. However, the applicability of this different tool roughness is not verified. Additional experiments with a different tool roughness should be performed to validate for a different tool roughness.

- The effect of abrasive wear on adhesive wear (galling) is not known. The strip draw experiments showed a large difference between the adhered and abraded volume. It should be investigated what the relation between adhesive and abrasive wear is regarding galling at elevated temperatures to gain a better understanding of these wear mechanisms.

- Getting the adhered volume from the experimental data as is done in section 4 is an extensive process. It would be more convenient if it is possible for only line measurements to provide suitable information for calibration. Also, line measurements provide a wider

range of information on the surface compared to a local confocal measurement. The use of line measurements to derive a suitable data should be investigated if the model needs to be extended for multiple sheet and tool systems.

Validation

- The projected galling amount on the production parts is not verified as a quantitative result. Therefore, the predicted amounts can only be used in a relative comparison. Experiments should be performed to match the observed severity to the galling amount.
- In the validation for the B-pillar only a single confocal measurement per draw and per location has been performed. For future reference it would be beneficial to perform at least two measurements for the same location to verify the results from that measurement. In addition, an additional measurement location for the straight T-top edge would we beneficial to verify the single measurement location.
- The tool material is not exactly the same as that used in the experiments. The system can be improved by using the real 3D surface measurements of the tool to get a more accurate approximation.
- Effect of tool temperature on galling is not directly applied in the galling model. The tool temperature only affects the model, because the heat transfer affects the sheet temperature. The tool temperature can go up to 525°C as shown in the industrial part (Side Member) of Volvo Cars. In literature the elevated tool temperature shows a decrease in adhered volume (figure 2.11). In this case the tool temperature goes up to 375°C . The effect of higher tool temperatures on galling behavior is not exactly known and should be investigated.

References

[1] L. Pelcastre, *Hot Forming Tribology: Galling of Tools and Associated Problems*. PhD thesis, Luleå University of Technology, 2011.

[2] E. van der Heide, *Lubricant failure in sheet metal forming processes*. PhD thesis, University of Twente, Apr. 2002.

[3] J. Venema, *Tribological interactions and modelling of friction in hot stamping*. PhD thesis, University of Twente, Sept. 2019.

[4] G. van der Linde, *Predicting galling behaviour in deep drawing processes*. PhD thesis, University of Twente, Nov. 2011.

[5] M. de Rooij, *Tribology aspects of unlubricated deepdrawing processes*. PhD thesis, University of Twente, Nov. 1998.

[6] J. Tungtrongpairoj, V. Uthaisangsuk, and W. Bleck, "Determination of yield behaviour of boron alloy steel at high temperature," *Journal of Metals, Materials and Minerals*, vol. 19, no. 1, pp. 29–38, 2009.

[7] A. Ghiotti, S. Bruschi, and F. Borsetto, "Tribological characteristics of high strength steel sheets under holding conditions," *Journal of Material Processing Technology*, vol. 211, pp. 1694–1700, 2011.

[8] M. Windmann, A. Röttger, and W. Theisen, "Formation of intermetallic phases in al-coated hot-stamped 22mnb5 sheets in terms of coating thickness and si content," *Surface & Coatings Technology*, vol. 246, pp. 17–25, 2014.

[9] M. Windmann, A. Röttger, I. Hahn, and W. Theisen, "Mechanical properties of al_xfe_y intermetallic in al-base coatings on steel 22mnb5 and resulting wear mechanisms at press-hardening tool steel surfaces," *Surface & Coatings Technology*, vol. 321, pp. 321–327, 2017.

[10] N. Kyokuta, M. Koba, T. Araki, S. Nambu, J. Inoue, and T. Koseki, "Fracture toughness evaluation of thin fe-al intermetallic compound layer at reactive interface between dissimilar metals," *Materials Transactions*, vol. 54, no. 6, pp. 994–1000, 2013.

[11] L. Percastre, J. Hardell, A. Rolland, and B. Prakash, "Influence of microstructural evolution of al-si coated uhss on its tribological behaviour against tool steel at elevated temperatures," *Journal of Materials Processing Technology*, vol. 228, pp. 117–124, 2016.

[12] M. W. M Merklein, "Investigations on austenitization parameters influencing wear behavior within hot stamping," *Procedia Engineering*, vol. 81, pp. 1695–1700, 2014.

[13] P. Schwingenschlögl and M. Merklein, "Characterization of tribological conditions within direct hot stamping," *Journal of Materials Processing Tech.*, vol. 278, 2020.

[14] J. Hardell, S. Hernandez, S. Mozgovoy, L. Percastre, C. Courbon, and B. Prakash, "Effect of oxide layers and near surface transformations on friction and wear during tool steel and boron steel interaction at high temperatures," *Wear*, vol. 330-331, pp. 223–229, 2015.

[15] J. Hardell, *Tribology of Hot Forming Tool and High Strength Steels*. PhD thesis, Lulea University of Technogoly, Sept. 2009.

[16] S. Mozgovoy, J. Hardell, and B. Prakash, "High temperature friction and wear performance of pvd coatings under press hardening contact conditions," *Advances in Tribology*, vol. 2019, p. 15 pages, 2019. Article ID 4981246.

[17] A. W. Nesselaar, "Prediction of galling in hot stamping processes," Master's thesis, University of Twente, Sept. 2004.

[18] L. Pelcastre, J. Hardell, and B. Prakash, "Investigations into the occurrence of galling during hot forming of al–si-coated high-strength steel," in *Proceedings of the Institution of Mechanical Engineers*, vol. 225 of *J*, pp. 487–498, Journal of Engineering Tribology, 2011.

[19] M. Vilasec, J. Pujante, G. Ramírez, and D. casellas, "Investigation into adhesive wear of pvd coated and uncoated hot stamping production tools," *Wear*, vol. 308, pp. 148–154, 2013.

[20] L. Percastre, J. Hardell, and B. Prakash, "Galling mechanisms during interaction of tool steel and al–si coated ultra-high strength steel at elevated temperature," *Tribology International*, vol. 67, pp. 263–271, 2013.

[21] C. Boher, S. L. Roux, L. Penazzi, and C. Dessain, "Experimental inversitgation of the tribological behaviour and wear mechanisms of tool steel grades in hot stamping of a high-strength boron steel," *Wear*, vol. 294-295, pp. 286–295, 2012.

[22] J. Hardell and B. Prakash, "High-temperature friction and wear behaviour of different tool steels during sliding against al–si-coated high-strength steel," *Tribology international*, vol. 41, pp. 663–671, 2007.

[23] P. Schwingenschlögl, P. Niederhofer, and M. Merklein, "Investigation on basic friction and wear mechanisms with in hot stamping considering the influence of tool steel and hardness," *Wear*, vol. 426, pp. 378–389, 2019.

[24] J. Hol, *Multi-Scale friction modeling for sheet metal forming*. PhD thesis, University of Twente, Dec. 2013.

[25] W. W. F. Chong and M. D. la Cruz, "Elastoplastic contact of rough surfaces: a line contact model for boundary regime of lubrication," *Meccanica*, vol. 49, pp. 1177–1191, 2014.

[26] A. Ghiotti, S. Bruschi, F. Sgarabotto, and P. F. Bariani, "Tribological performances of zn-based coating in direct hot stamping," *Tribology international*, vol. 78, pp. 142–151, 2014.

[27] F. Medea, G. Venturato, A. Ghiotti, and S. Bruschi, "Tribological performances of new steel grades for hot stamping tools," *Journal of Physics: Conference Series*, vol. 896, 2017.

[28] F. H. Stott, "High-temperature sliding wear of metals," *Tribology international*, vol. 35, pp. 489–495, 2002.

[29] M. Geiger, M. Merklein, and J. Lechler, "Determination of tribological conditions within hot stamping," *Production Engineering - Research and Development*, vol. 2, pp. 269–276, 2008.

[30] X. Tian, Y. Zhang, and J. Li, "Investigation on tribological behavior of advanced high strength steels: Influence of hot stamping process parameters," *Tribology Letters*, vol. 45, pp. 489–495, 2012.

[31] S. Mozgovoy, *High Temperature Friction and Wear in Press Hardening*. PhD thesis, Luleå University of Technology, 2014.

[32] L. Wang, *Modelling of friction for high temperature extrusion of aluminium alloys*. PhD thesis, Technische Universiteit Delft, febr. 2012.

[33] DIN-50320, "Wear, terms, systematic analysis of wear processes, classification of wear phenomena," standard, German Institute for Standardisation (Deutsches Institut für Normung), 1979.

[34] M. A. Masen, *Abrasive tool wear in metal forming processes*. PhD thesis, University of Twente, Jun. 2019.

[35] E. Rabinowicz, *Friction and wear of materials*. John Wiley & Sons, 1995.

[36] J. M. Challen and P. L. B. Oxley, "An expiation of the different regimes of friction and wear using asperity deformation models," *Wear*, vol. 53, pp. 229–243, 1979.

[37] K. Hokkirigawa and K. Kato, "An experimental and theoretical investigation of ploughing, cutting and wedge formation during abrasive wear," *Tribology international*, vol. 21, no. 1, pp. 51–57, 1988.

[38] A. Gåård, P. Krakhmalev, and J. bergstorm, "Wear mechanisms in deep drawing of carbon steel – correlation to laboratory testing," *Tribotest*, vol. 14, pp. 1–9, 2008.

[39] H. Dickhof, "Prediction of galling in industrial sheet metal forming processes," Master's thesis, University of Twente, Jan. 2017.

[40] E. Schedin and B. Lehtinen, "Galling mechanisms in lubricated systems: a study of sheet metal forming," *Wear*, vol. 170, pp. 119–130, 1993.

[41] P. Schwingenschlögl, M. Weldi, and M. Merklein, "Investigation of the influence of process parameters on adhesive wear under hot stamping conditions," *36th IDDRG Conference – Materials Modelling and Testing for Sheet Metal Forming*, 2017.

[42] A. Ghiotti, S. Bruschi, and F. Medea, "Comparison of tribological and wear performances of alsi and zn coatings in hot stamping of boron steel sheets," *Wear*, vol. 332-333, pp. 810–821, 2015.

[43] A. ghiotti, F. Sgarabotto, and S. Bruschi, "A novel approach to wear testing in hot stamping of high strength boron steel sheets," *Wear*, vol. 302, pp. 1319–1326, 2013.

[44] J. F. Archard and W. Hirst, "The wear of metals under unlubricated conditions," in *Proceedings of the Royal Society of London - Mathematical and Physical Science*, vol. 236 of *A*, pp. 397–410, Royal Society, 1956.

[45] S. Schönecker, X. Li, B. Johansson, S. K. Kwon, and L. Vitos, "Thermal surface free energy and stress of iron," *Scientific reports*, vol. 5, 2015.

[46] R. S. Lee and J. L. Jou, "Application of numerical simulation for wear analysis of warm forging die," *Journal of Materials Processing Technology*, vol. 140, pp. 43–48, 2003.

[47] L. Deng, S. Mozgovoy, J. Hardell, B. Prakash, and M. Oldenburg, "Numerical study of contact conditions in press hardening for tool wear simulation," *International journal of material forming*, vol. 10, pp. 85–96, 2017.

[48] L. Deng, *Modelling of Wear and Galling in Press Hardening Simulations*. PhD thesis, Lulea University of Technogoly, Nov. 2017.

[49] L. Deng, L. Pelcastre, J. Hardell, B. Prakash, and M. Oldenburg, "Numerical investigation of galling in a press hardening experiment with alsi-coated workpiece," *Engineering Failure Analysis*, vol. 99, pp. 85–96, 2019.

[50] J. Y. Lee, M. P. J. Punkkinen, S. Schönecker, Z. Nabi, K. Kádas, V. Zólyomi, Y. M. Koo, Q. M. Hu, R. Ahuja, B. Johansson, J. Kollár, L. Vitos, and S. K. Kwon, "The surface energy and stress of metals," *Surface science*, vol. 674, pp. 51–68, 2018.

[51] M. Abspoel, B. M. Neelis, and P. van Liempt, "Constitutive behaviour under hot stamping conditions," *Journal of Material Processing Technology*, vol. 228, pp. 34–42, 2016.

[52] Y. Wang, "Tribology and friction in industrial hot stamping processes," Master's thesis, University of Twente, Sept. 2019.

[53] D. Tabor, "Junction growth in metallic friction: The role of combined stresses and surface contamination," in *Proceedings of the Royal Society of London - Mathematical and Physical Science*, vol. 251 of *A*, pp. 378–393, Royal Society, 1959.

[54] J. D. Westeneng, *MODELLING OF CONTACT AND FRICTION IN DEEP DRAWING PROCESSES*. PhD thesis, University of Twente, Mar. 2001.

[55] X. Ma, M. de Rooij, and D. Schipper, "A load dependent friction model for fully plastic contact conditions," *Wear*, vol. 269, pp. 790–796, 2010.

[56] E. van der Heide and D. J. Schipper, "Galling initiation due to frictional heating," *Wear*, vol. 254, pp. 1127–1133, 2003.

[57] J. Venema, D. T. A. Matthews, J. Hazrati, J. Wörmann, and A. H. van den Boogaard, "Friction and wear mechanisms during hot stamping of alsi coated press hardening steel," *Wear*, vol. 380-381, pp. 137–145, 2017.

[58] W. D. Callister and D. G. Rethwisch, *Material Science and Engineering*. John Wiley & Sons, eighth ed., 2011. ISBN: 978-0-470-50586-1.

[59] L. Ruiz-Pérez, G. J. Royston, J. Patrick, A. Fairclough, and A. J. Ryan, "Toughening by nanostructure," *Polymer*, vol. 49, pp. 4475–4488, 2008.

[60] M. B. de Rooij, G. van der Linde, and D. J. Schipper, "Modelling material transfer on a single asperity scale," *Wear*, vol. 307, pp. 198–208, 2013.

[61] P. Diss and M. Brendlé, "A general approach to discontinuous transfer films: influence of sliding speed and stick-slip phenomena," *Wear*, vol. 203-204, pp. 564–572, 1997.

[62] J. N. Israelachvili, *Intermolecular and surface forces*. Academic Press, third ed., 2011. ISBN: 978-0-12-375182-9.

[63] Personal communication with J. Venema from Tata Steel. 8th Januari 2021.

[64] Personal communication with stamping engineers from Volvo Cars. 10th Februari 2021.

A Appendix: Galling model

A.1 Mathematical approach friction coefficient

This section shows the mathematical approach for the friction coefficient for cutting, ploughing and wedging according to the wear mode diagram shown in figure 2.9.

The mathematical approach for cutting:

$$\mu_{\text{cutting}} = \tan\left(\theta - \frac{1}{4}\pi + \frac{1}{2}\arccos\left(f_{\text{C}}\right)\right) \tag{A.1}$$

The mathematical approach for ploughing:

$$\mu_{\text{ploughing}} = \frac{A_1 \sin\theta + \cos\left(\arccos\left(f_{\text{C}} - \theta\right)\right)}{A_1 \sin\theta + \sin\left(\arccos\left(f_{\text{C}} - \theta\right)\right)} \tag{A.2}$$

with

$$A_1 = 1 + \frac{1}{2}\pi + \arccos\left(f_{\text{C}}\right) - 2\theta - 2\arcsin\left(\frac{\sin\theta}{\left(1 - f_{\text{C}}\right)^{1/2}}\right) \tag{A.3}$$

The mathematical approach for wedge formation:

$$\mu_{\text{wear}} = \frac{\left\{1 - 2\sin A_2 + \left(1 - f_{\text{C}}^2\right)^{1/2}\right\}\sin\theta + f_{\text{C}}\cos\theta}{\left\{1 - 2\sin A_2 + \left(1 - f_{\text{C}}^2\right)^{1/2}\right\}\cos\theta - f_{\text{C}}\sin\theta} \tag{A.4}$$

with

$$A_2 = 1 - \frac{1}{4}\pi - \frac{1}{2}\arccos f_{\text{C}} + \arcsin\left(\frac{\sin\theta}{\left(1 - f_{\text{C}}\right)^{1/2}}\right) \tag{A.5}$$

A.2 Conversion to hexagon based polyhedron

First, the elliptical base, which can be described in parametric form by equation A.6, of the asperity is transformed to a hexagon. The hexagon is defined within the ellipse at that point, but it needs to be scaled to have the same surface area as the original contact surface (ellipse). Finally, the height of the hexagon based polyhedron will be determined using volume equilibrium.

$$\begin{aligned} x &= a\cos\phi\cos t - b\sin\phi\sin t \\ y &= a\sin\phi\cos t - b\cos\phi\sin t \end{aligned} \tag{A.6}$$

The vertices of a hexagon within the ellipse, like in figure 3.12, are determined using the parametric form of the ellipse. First, the points within $0 < \phi < 0.5\pi$ are derived (point A, B and F). Point A is defined by the location on the ellipse with a maximum y-coordinate, point F by the location on the ellipse with a maximum x-coordinate and point B has the same y-coordinate as point F, but on the other side of the major axis of the ellipse. This provides the following relations for t_A, t_F and t_B:

$$\begin{aligned} t_A &= \operatorname{atan}\left(\frac{b}{a}\cot\phi\right) \\ t_F &= -\operatorname{atan}\left(\frac{b}{a}\tan\phi\right) \\ t_B &= 2t_A - t_F \end{aligned} \tag{A.7}$$

The coordinates for these points can now be found. The coordinates for the other vertices (C,D and E) can now be defined as in equation A.8.

$$\begin{aligned}(x_C, y_C) &= -(x_F, y_F)\\ (x_D, y_D) &= -(x_A, y_A)\\ (x_E, y_B) &= -(x_B, y_B)\end{aligned} \tag{A.8}$$

Now, for the points within $-0.5\pi < \phi < 0$ are determined. Here, point D adopts the property of point A, point E that of point F and point C that of point B. This provides the following relations for t_D, t_E and t_C:

$$\begin{aligned}t_D &= \operatorname{atan}\left(\frac{b}{a}\cot\phi\right)\\ t_E &= -\operatorname{atan}\left(\frac{b}{a}\tan\phi\right)\\ t_C &= 2t_D - t_E\end{aligned} \tag{A.9}$$

At this stage the coordinates of hexagon within the ellipse are defined. The hexagon dimensions are geometrically characterized by the relations below:

$$\begin{aligned}w_{\mathrm{I}} = w_{\mathrm{III}} &= y_A - y_F\\ w_{\mathrm{II}} &= y_F - y_E = 2y_F\\ l = l_b &= 0.5\,(x_F - x_B)\\ \alpha &= -a\tan\left(\frac{x_A}{y_A}\right)\end{aligned} \tag{A.10}$$

The surface area of the hexagon should be equal to the surface area of the original contact spot. Therefore, the hexagon will be scaled proportionally in x and y-direction. Note, that only w_{I}, w_{III}, l and l_b will be scaled, which causes the triangles ABF and CDE to scale proportionally and the parallelogram BCEF to scale only in x-direction. The scaling factor to increase the surface area of the hexagon, to equal that of the ellipse, is given in equation A.11.

$$c_{\text{scale}} = \frac{-lw_{\mathrm{II}} + \sqrt{l^2 w_{\mathrm{II}}^2 + \pi abl\,(w_{\mathrm{I}} + w_{\mathrm{III}})}}{l\,(w_{\mathrm{I}} + w_{\mathrm{III}})} \tag{A.11}$$

The final step is determining the height for the hexagon polyhedron asperity. The volume of the elliptical paraboloid should be equal to the volume of the hexagon based polyhedron, which provides the relation below:

$$h = \frac{6V}{(w_{\mathrm{I}} + 3w_{\mathrm{II}} + w_{\mathrm{III}})\,(l + l_b)} \tag{A.12}$$

A.3 Forces hexagon based asperity

The following assumptions are made to be able to determine the forces in x- and y-direction [4].

- The asperity is not symmetric.
- The origin is at the intersection of AD with a line parallel to BF which goes through the middle of BC.
- The faces AGF, FGHE and HDE, see figure 3.13, are the contact planes on which normal pressure and shear stresses act.
- The contact pressure has a constant value on the whole contact area.

- The tangential shear stress is calculated using Coulomb friction law $\tau = \mu p_{pl}$.
- The asperity is rigid.
- The base of the hexagon asperity requires lines parallel to the ploughing/sliding direction.

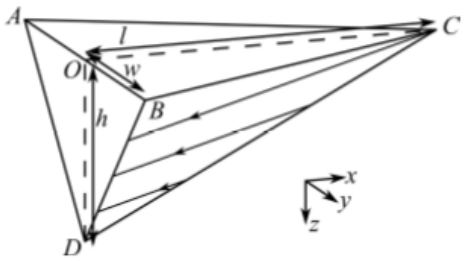

Figure A.1: Tip geometry with its dimension and flow lines on BDC of plastic deforming material.

The dimensions in a simple pyramid shaped asperity as shown in figure A.1 are given by l, w and h. The majority of the asperity shapes will have a hexagon base and therefore w needs to be replaced with:

$$\text{Sec I: } w \to \frac{w_I l}{l + w_I \cos\alpha} \qquad \text{Sec II: } w \to l\cot\alpha \qquad \text{Sec III: } w \to \frac{w_{III} l}{l - w_{III}\cos\alpha} \tag{A.13}$$

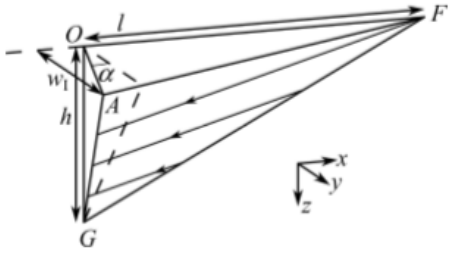

Figure A.2: Frontal part of section I of the asperity.

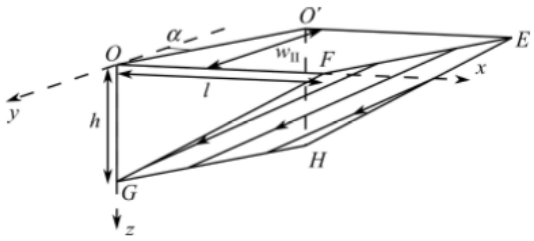

Figure A.3: Frontal part of section II, an oblique prism, of the asperity.

The forces in x- and y-direction for section I can be derived using figure A.2. The forces for section III are more or less a mirrored version of section I. The forces for section II can be derived using figure A.3. The total forces in x- and y-direction are shown in equation A.14 and A.15. The complete derivation can be found in the appendix of the thesis of van der Linde [4].

$$\begin{aligned} F_x = &- p_{pl} h \left(\frac{1}{2} w_I + w_{II} + \frac{1}{2} w_{III} \right) \\ &- \tau_{pl} \left(\frac{1}{2} \sqrt{(w_I l)^2 + h^2 \left(l + w_I \tan(\alpha)\right)^2} \right. \\ &\left. + w_{II} \sqrt{l^2 + h^2 \tan^2(\alpha)} + \frac{1}{2} \sqrt{(w_{III} l)^2 + h^2 \left(l - w_{III} \tan(\alpha)\right)^2} \right) \end{aligned} \tag{A.14}$$

$$
\begin{aligned}
F_y = &- p_{pl} h \tan(\alpha) \left(\frac{1}{2} w_I + w_{II} + \frac{1}{2} w_{III} \right) \\
&+ \tau_{pl} h^2 \left(\frac{1}{2} \frac{w_I \left(l + w_I \tan(\alpha) \right)}{\sqrt{\left(w_I l \right)^2 + h^2 \left(l + w_I \tan(\alpha) \right)^2}} \right. \\
&\left. + \frac{w_{II} \tan(\alpha)}{\sqrt{l^2 + h^2 \tan^2(\alpha)}} - \frac{1}{2} \frac{w_{III} \left(l - w_{III} \tan(\alpha) \right)}{\sqrt{\left(w_{III} l \right)^2 + h^2 \left(l - w_{III} \tan(\alpha) \right)^2}} \right)
\end{aligned}
\tag{A.15}
$$

A.4 Tables

	Most stable (A)	Least stable (B)	Otherwise (C)
l_b	l_{b0}	$\frac{l_{b0}+l_1}{l_{b0}+l_0} l_{b0}$	ch
l	l_1	$\frac{l_{b0}+l_1}{l_{b0}+l_0} l_0$	$l_1 + l_{b0} - ch$
h	h_0	$\frac{l_{b0}+l_1}{l_{b0}+l_0} h_0$	h
w_{I}	w_{I0}	$\frac{l_{b0}+l_1}{l_{b0}+l_0} w_{\mathrm{I0}}$	$\frac{ch}{l_{b0}} w_{\mathrm{I0}}$
w_{III}	w_{III0}	$\frac{l_{b0}+l_1}{l_{b0}+l_0} w_{\mathrm{III0}}$	$\frac{ch}{l_{b0}} w_{\mathrm{III0}}$

Table A.1: Dimensions of lump (asperity) after stability step [4]. $l_{b0} = ch$ *is used instead of the physical length for the first lump layer, cause lump stability uses just a portion of the backside of the asperity.*

	Parameter	Value
Asperity parameters	a	2.5 μm
	b	0.5 μm
	h	0.3 μm
Material parameters	B	2.8
	H	1.0 GPa
	T	0.27
	$\Delta\gamma$	1.1 Jm^{-2}
Additional parameters	l_{slide}	0.1 m
	c_{fr}	$1 \cdot 10^{-5} \mathrm{m}^2\ \mathrm{J}^{-1}$
	μ_{max}	0.18
	# of cycles n	5

Table A.2: Single asperity parameters for lump growth model

B Appendix: Hot strip draw experiments

B.1 Comparison confocal measurement to line measurement

Getting the adhered volume from the confocal measurement uses a lot of steps and the confocal measurement shown only the 3D surface roughness of a small area. A line measurement on the other hand is an easier measurement to perform, describes the surface height over a wider piece of area and takes less steps in data processing. If a similar trend is found it could be possible to only use line measurements in future project. The line measurement only provide a 2D representation of the adhered material and therefore the unit in this comparison is different. So, only a comparison based on a similar trend can be done.

The results of adhered material for the line measurement series over temperature uses all the line measurements, which results in figure B.1. This figure shows the average value of both line measurements and the bars represent the extreme values. The extreme values are the value of line a and line b, because only two line measurements are done per set. Also, a figure is made for the line measurement series over sliding length, see figure B.2. As before only the line b measurements can be used and therefore this figure does not show any bars.

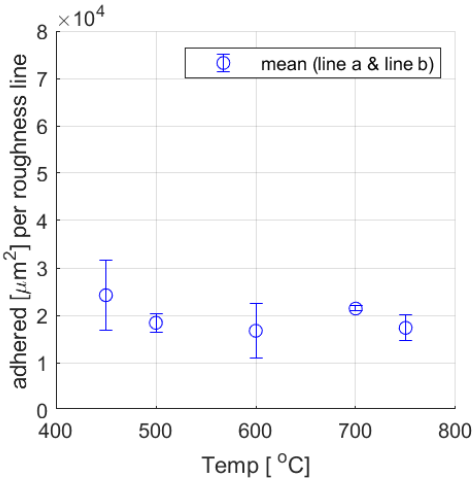

Figure B.1: Adhered material over temperature after 10 draws (2m in total).

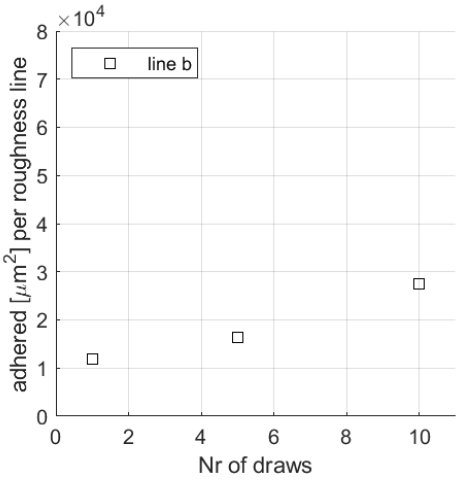

Figure B.2: Adhered material over number of draws (200 mm per draw).

First, the trend of the adhered material over temperature is analyzed (figure B.1). The range at 600°C is quite large. Taking only the top value at 600°C it shows an increase from 500°C to 600°C and a comparable value when going from 600°C to 700°C . This is not quite the dip that is seen in the figure on the confocal data, but is an indication that the trend will start to decrease. From 700°C to 750°C the decrease in adhered material is present. Then, the adhered material over sliding length (number of draws) is also plotted. These data points show that the adhered material increases over sliding length, which is also the relation found in the confocal measurements. However, this uses only one measurement per temperature, because only one line measurement (*Line b*) is usable.

It is concluded that just these two line measurements, although some comparisons can be made, are not sufficient to describe the same relation. The line measurements show potential and therefore further research on just using these 2D roughness measurements might yield to an easier way of data processing.

B.2 Experimental data

This section shows figures for all the measured parameter sets. These figures include the 2D line roughness with the best match (y-location) of the 3D confocal measurement. Also, the corresponding correlation over the x-position is given per each set. Subsections are used to split the measurements into groups with comparable parameters sets: *Pressure series on 2.5MPa*, *Pressure series on 5MPa* and *Sliding Length series*. The correlation plot over the x-position is valid for only one y-location of the confocal measurement. An indication on the second best correlation at that y-location is given, but a better match might be found on another y-location. Also, the correlation is based on both measurements starting at zero. Therefore, the right side of a correlation plot is zero, because the confocal image can not shift as far to the left as to the right.

B.2.1 Pressure series on 2.5MPa

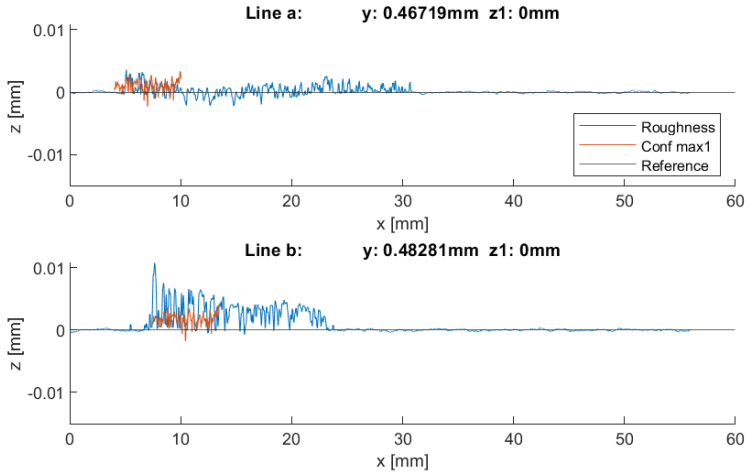

(a) Match confocal measurement with line measurement.

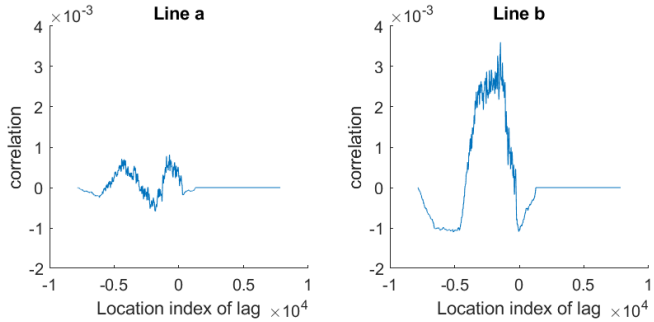

(b) Correlation for x-position.

Figure B.3: Experiment at 500°C with 2.5MPa

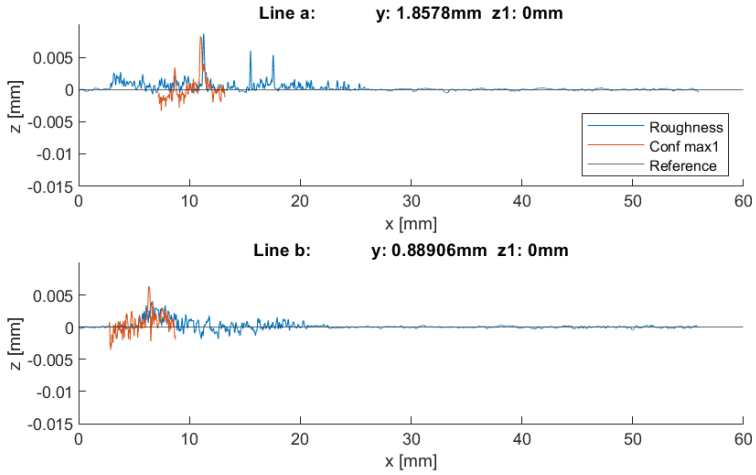

(a) Match confocal measurement with line measurement.

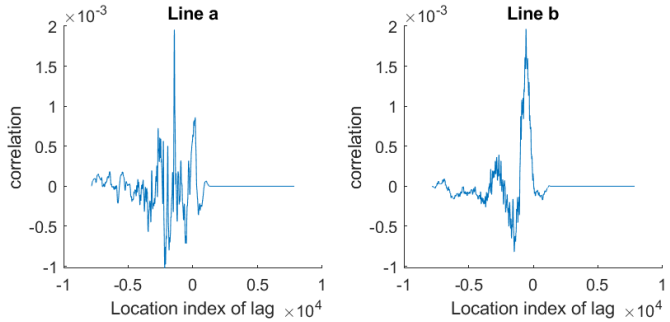

(b) Correlation for x-position.

Figure B.4: Experiment at 700°C with 2.5MPa

B.2.2 Pressure series on 5Mpa

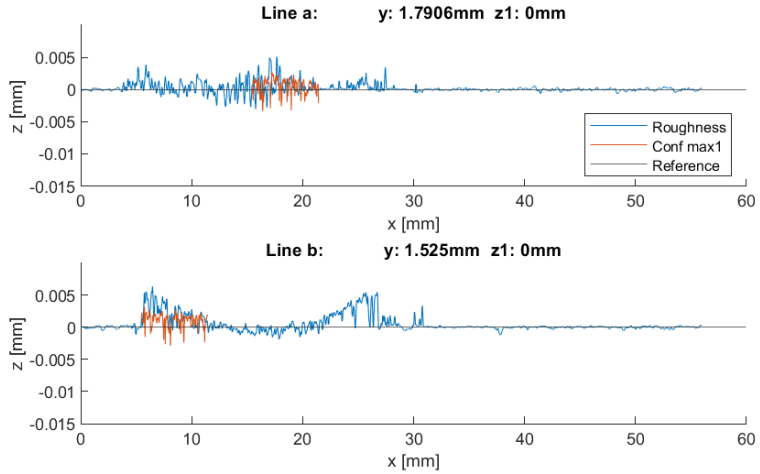

(a) Match confocal measurement with line measurement.

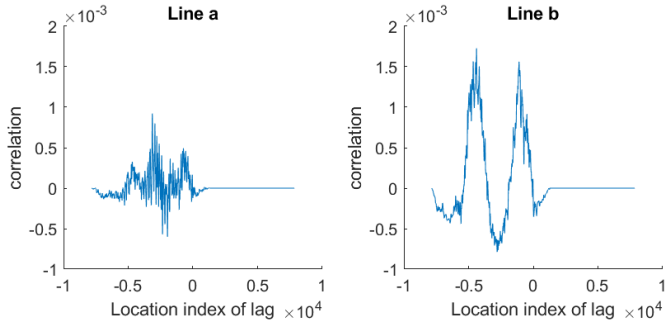

(b) Correlation for x-position.

Figure B.5: Experiment at 450°C with 5MPa

]

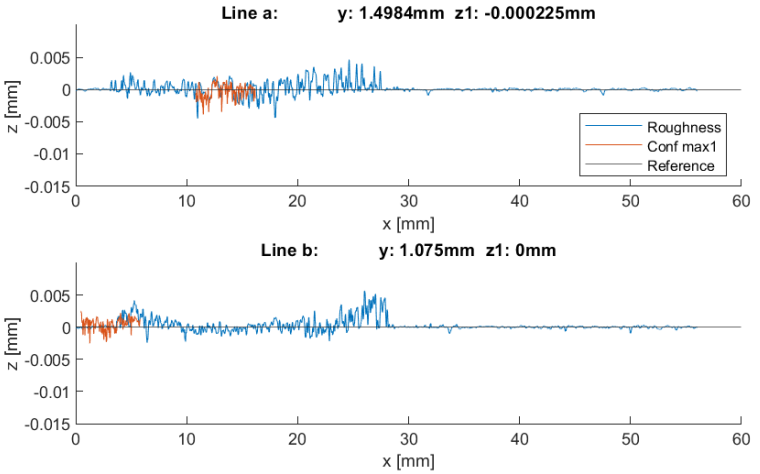

(a) Match confocal measurement with line measurement.

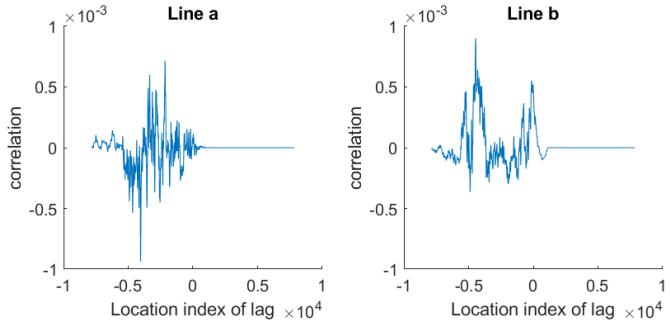

(b) Correlation for x-position.

Figure B.6: Experiment at 500°C with 5MPa

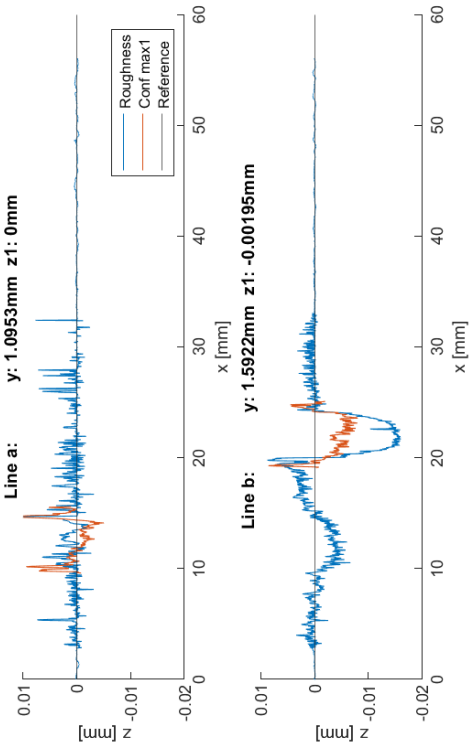

(a) Match confocal measurement with line measurement.

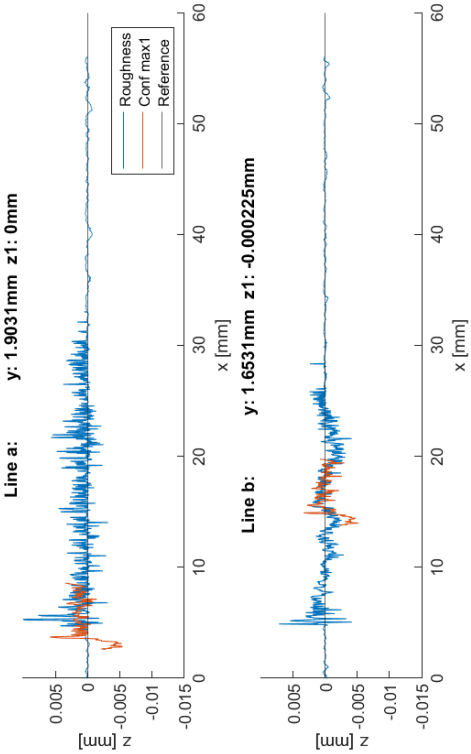

(b) Correlation for x-position.

Figure B.8: Experiment at 700°C with 5MPa

(a) Match confocal measurement with line measurement.

(b) Correlation for x-position.

Figure B.7: Experiment at 600°C with 5MPa

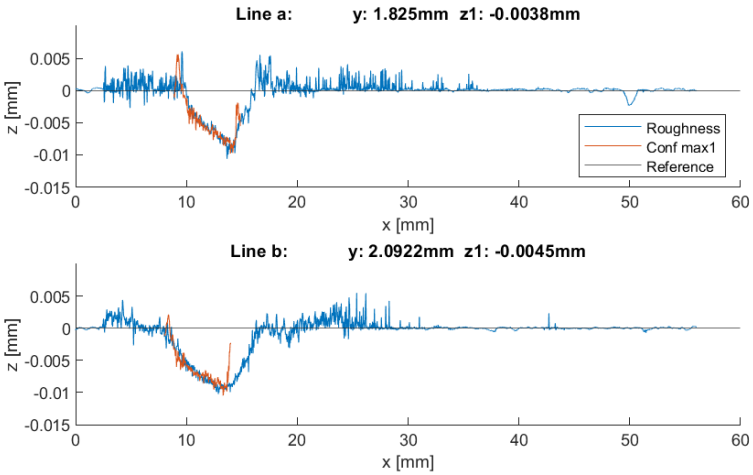

(a) Match confocal measurement with line measurement.

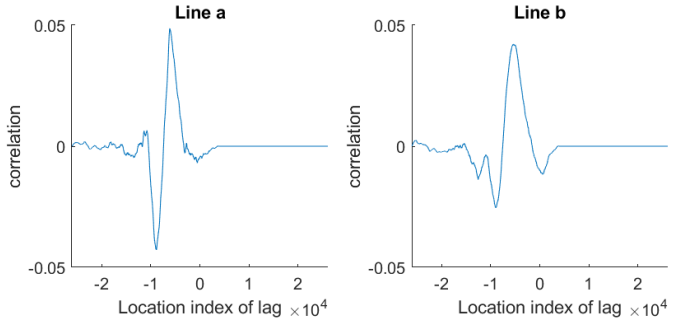

(b) Correlation for x-position.

Figure B.9: Experiment at 750°C with 5MPa

B.2.3 Sliding length series

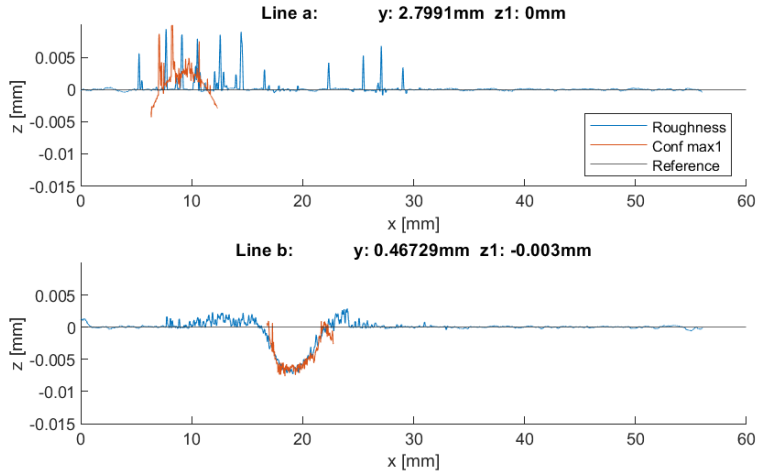

(a) Match confocal measurement with line measurement.

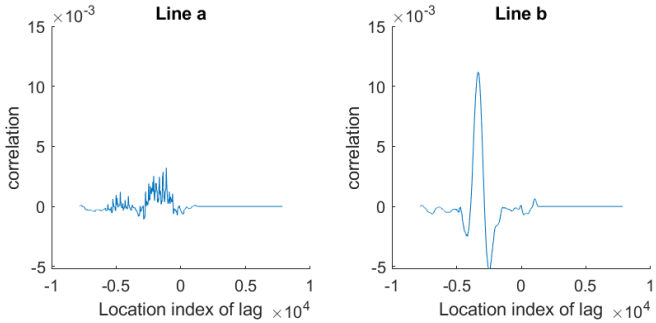

(b) Correlation for x-position.

Figure B.10: Experiment at 700°C with 5MPa for 1 draw of 200mm.

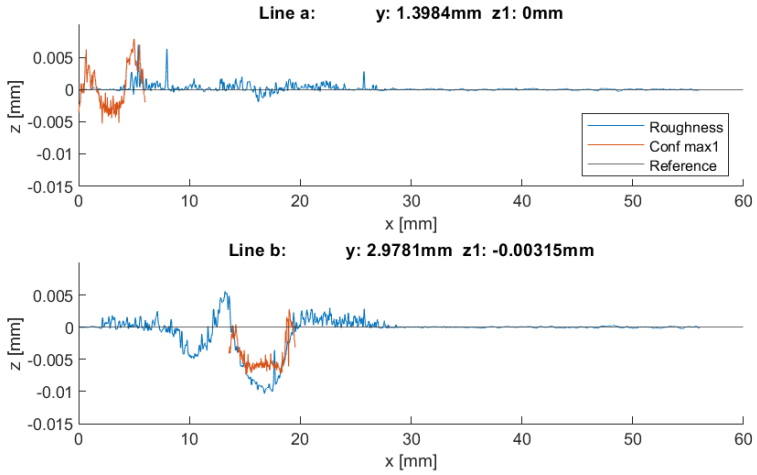

(a) Match confocal measurement with line measurement.

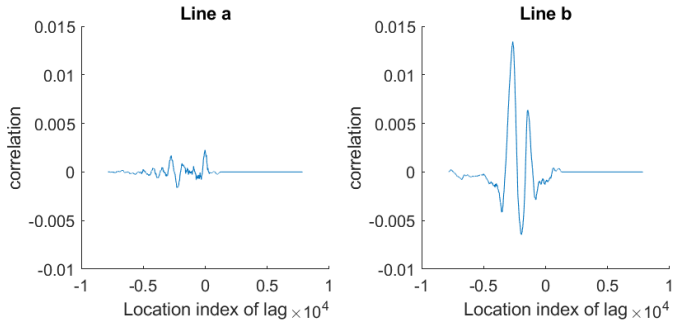

(b) Correlation for x-position.

Figure B.11: Experiment at 700°C with 5MPa for 5 draws of 200mm.

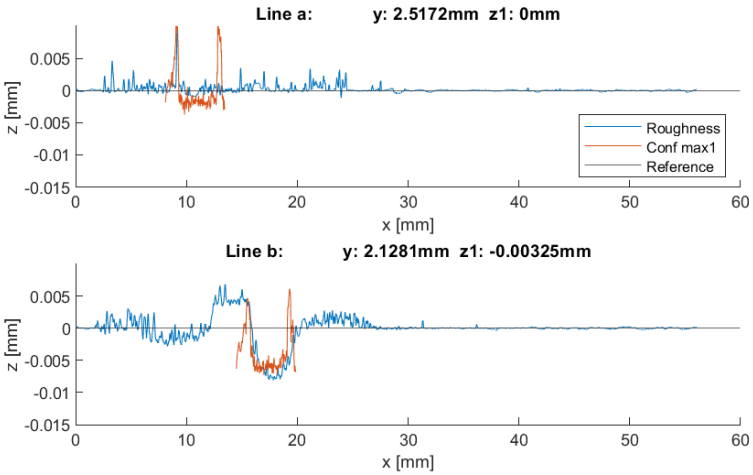

(a) Match confocal measurement with line measurement.

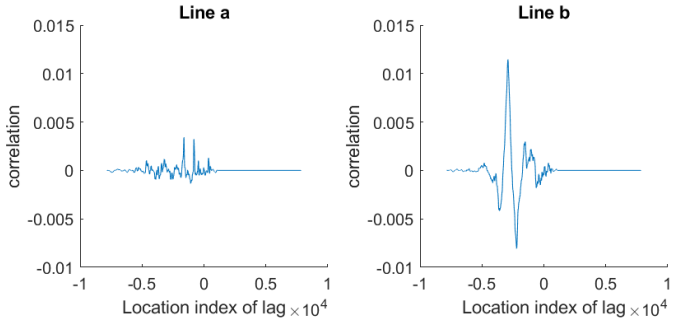

(b) Correlation for x-position.

Figure B.12: Experiment at 700°C with 5MPa for 10 draws of 200mm.

C Appendix: Results

C.1 Top view of initiated asperities

Here, multiple top view images are shown, which are used to support the explanation on the amount of asperities in contact and the amount of initiated asperities for CFI and WFI.

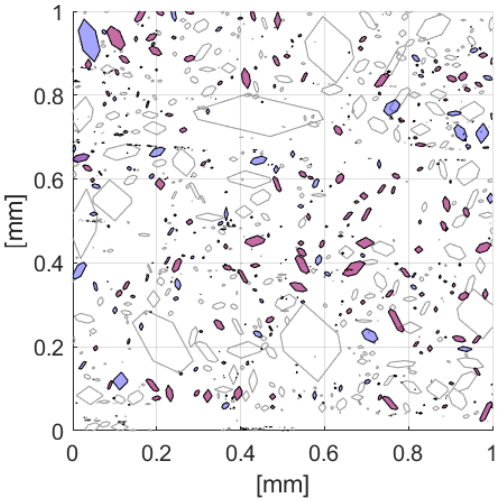

Figure C.1: The reference from the main text; 650°C , 5MPa and 0 strain.

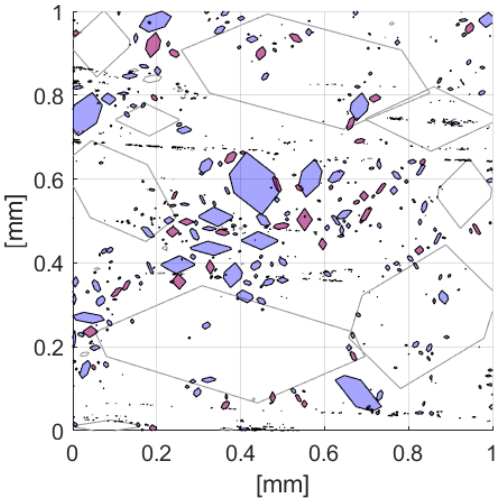

Figure C.2: Pressure change; 650°C , 25MPa and 0.0 strain.

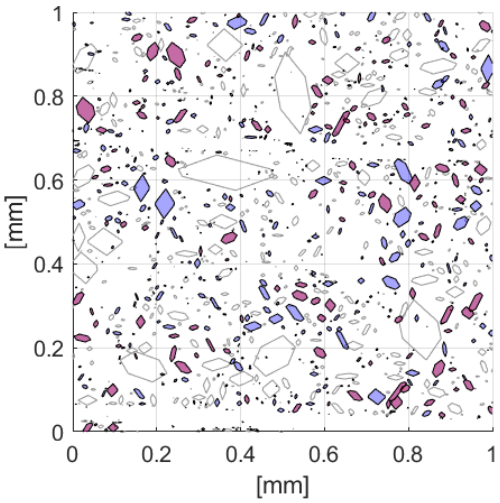

(a) Temp. change; 450°C , 5MPa and 0.0 strain.

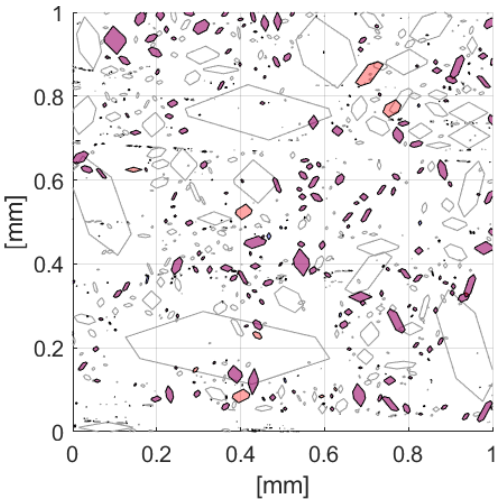

(b) Temp. change; 750°C , 5MPa and 0.0 strain.

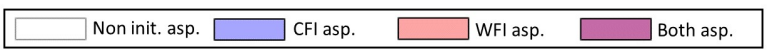

Figure C.3: Top view of all the identified asperity patches with temperature change compared to the reference in the main text (650°C , 5MPa and 0 strain). *Reference is repeated in figure C.1.*

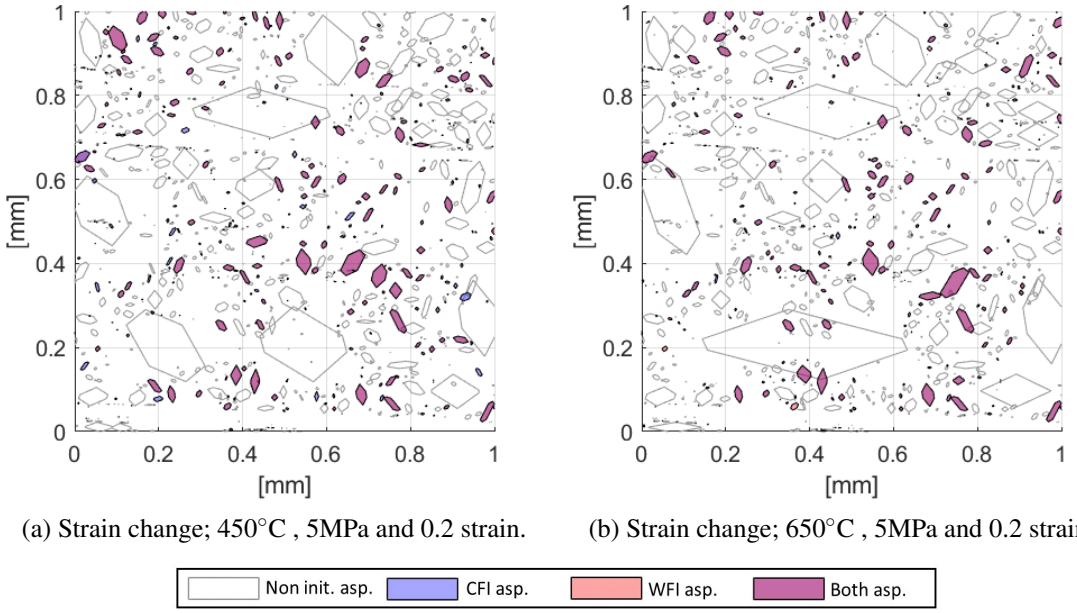

(a) Strain change; 450°C , 5MPa and 0.2 strain. (b) Strain change; 650°C , 5MPa and 0.2 strain.

Figure C.4: Top view of all the identified asperity patches for two different temperature and 0.2 strain. *The strain is different compared to the reference*.

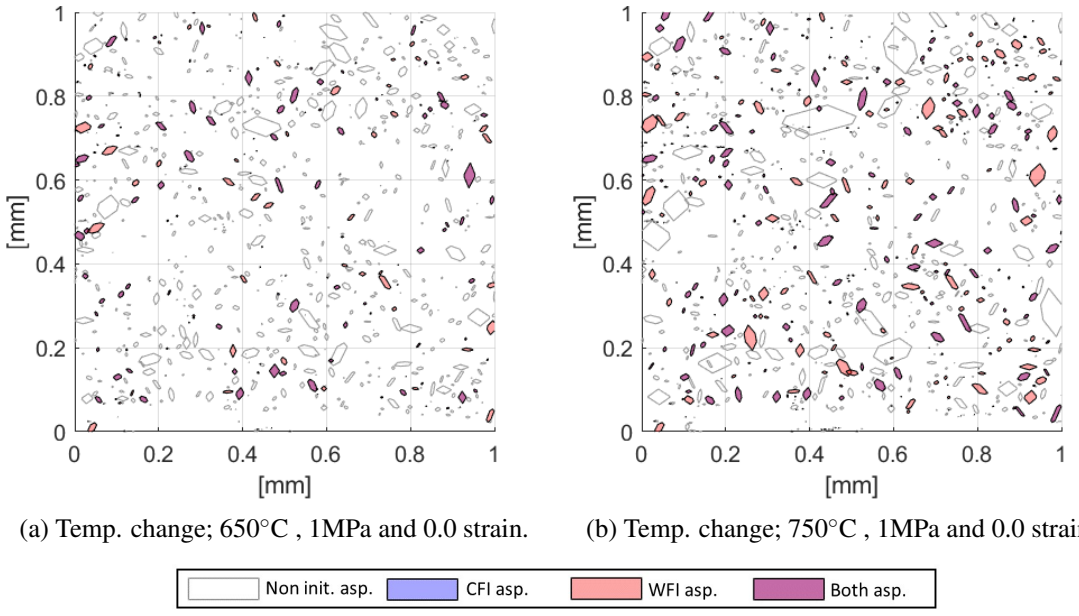

(a) Temp. change; 650°C , 1MPa and 0.0 strain. (b) Temp. change; 750°C , 1MPa and 0.0 strain.

Figure C.5: Top view of all the identified asperity patches with temperature change at 1MPa.

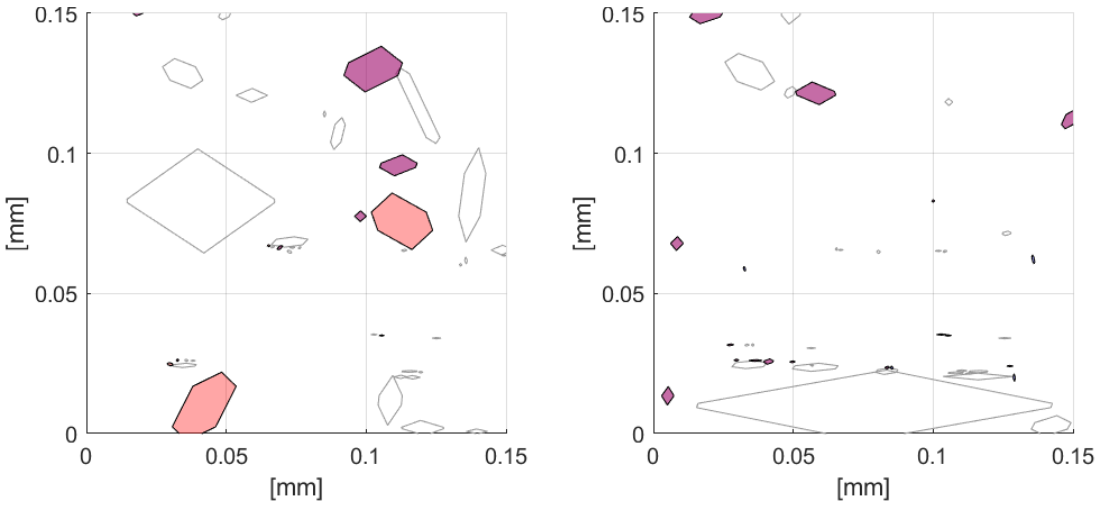

(a) Zoom 750°C , 1MPa and 0.0 strain (figure C.5b). (b) Zoom 750°C , 5MPa and 0.0 strain (figure C.3b).

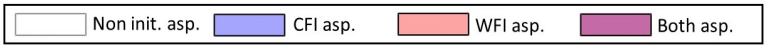

Figure C.6: Top view of all the identified asperity patches with pressure change at 750°C .

C.2 Asperity overlap (update separation height)

Here, the top view of the total asperities and the initiated asperities per model is shown for the used situation in section 6.3.2. Also, additional figures for the overlap percentage are added to see the effect over the temperature range valid for galling.

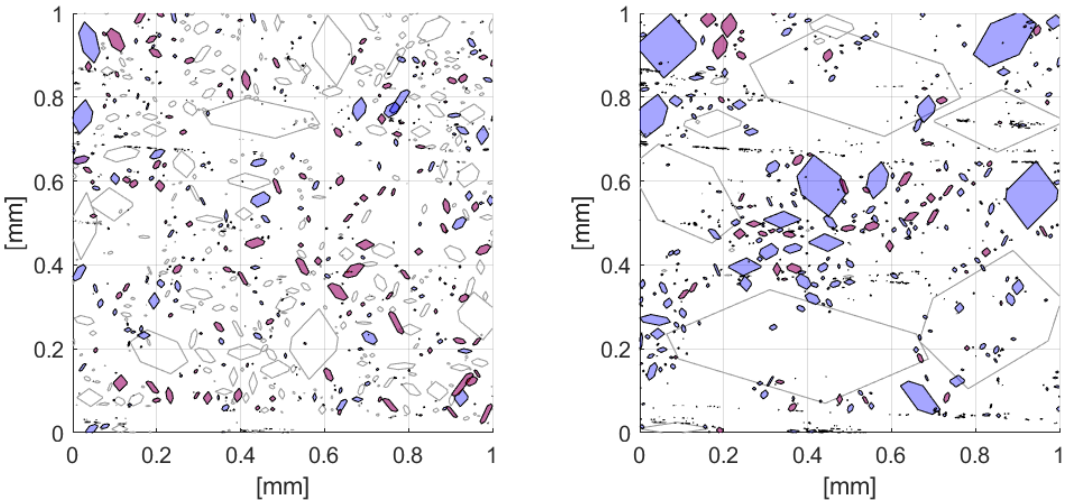

(a) 600°C , 5MPa and 0 strain.

(b) 600°C , 25MPa and 0 strain.

Figure C.7: Top view of all the identified asperity patches.

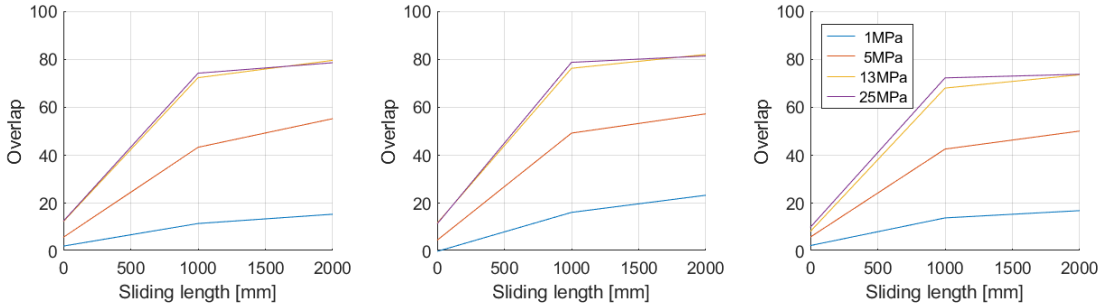

(a) 500°C (b) 600°C (c) 700°C

Figure C.8: The percentage of asperities which have at least one overlap with another asperity for CFI with the calibrated value for m.

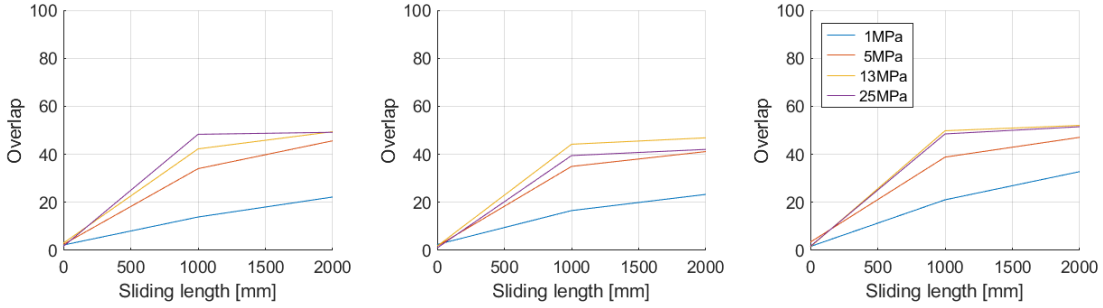

(a) 500°C (b) 600°C (c) 700°C

Figure C.9: The percentage of asperities which have at least one overlap with another asperity for WFI with the calibrated value for m.

D Appendix: Validation

D.1 Material used in B-pillar experiments

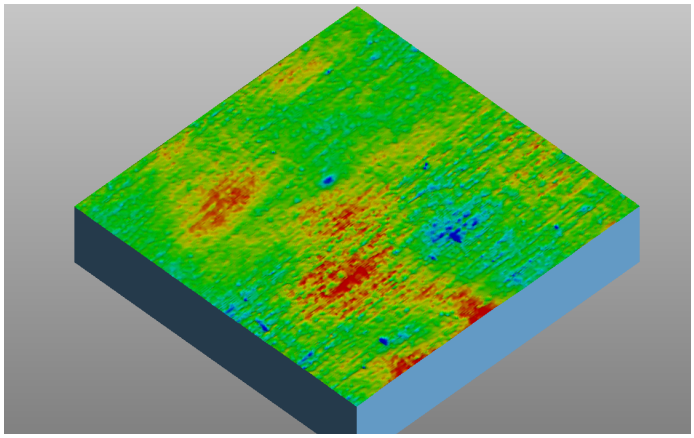

(a) Topography.

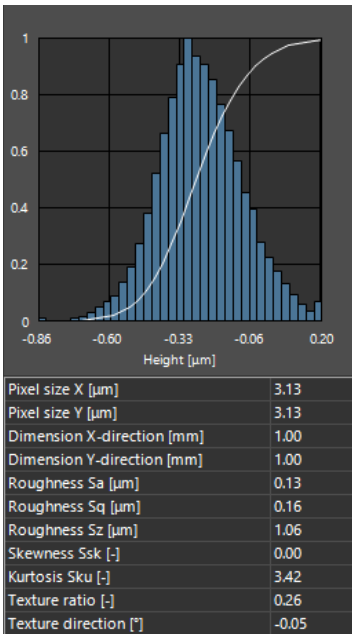

Pixel size X [µm]	3.13
Pixel size Y [µm]	3.13
Dimension X-direction [mm]	1.00
Dimension Y-direction [mm]	1.00
Roughness Sa [µm]	0.13
Roughness Sq [µm]	0.16
Roughness Sz [µm]	1.06
Skewness Ssk [-]	0.00
Kurtosis Sku [-]	3.42
Texture ratio [-]	0.26
Texture direction [°]	-0.05

(b) Surface height distribution.

Figure D.1: Tool surface of die radius. [63].

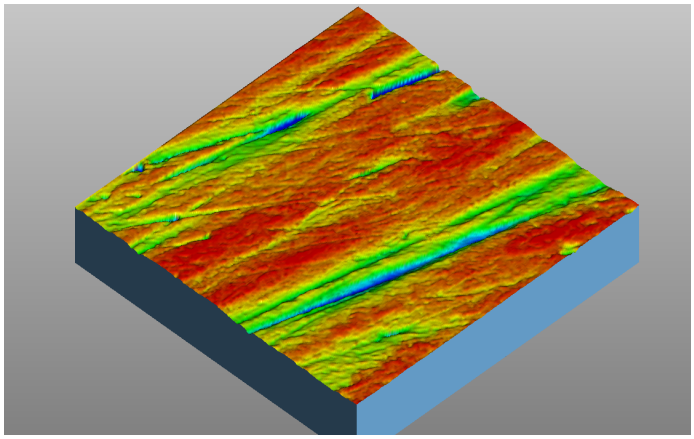

(a) Topography.

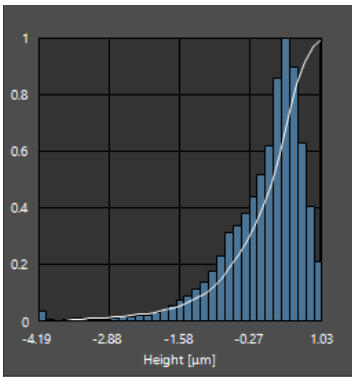

Pixel size X [µm]	3.13
Pixel size Y [µm]	3.13
Dimension X-direction [mm]	1.00
Dimension Y-direction [mm]	1.00
Roughness Sa [µm]	0.62
Roughness Sq [µm]	0.85
Roughness Sz [µm]	5.22
Skewness Ssk [-]	-1.93
Kurtosis Sku [-]	8.11
Texture ratio [-]	0.12
Texture direction [°]	62.36

(b) Surface height distribution.

Figure D.2: Tool surface of punch radius [63].

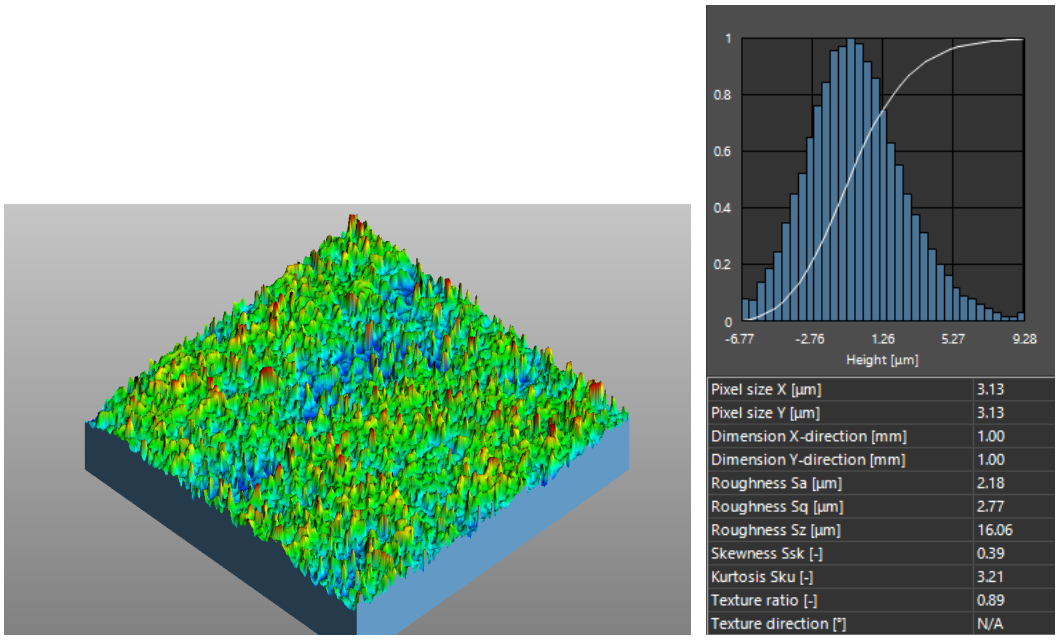

(a) Topography (b) Surface height distribution.

Figure D.3: Sheet surface [63].

D.2 Confocal images of topography evolution

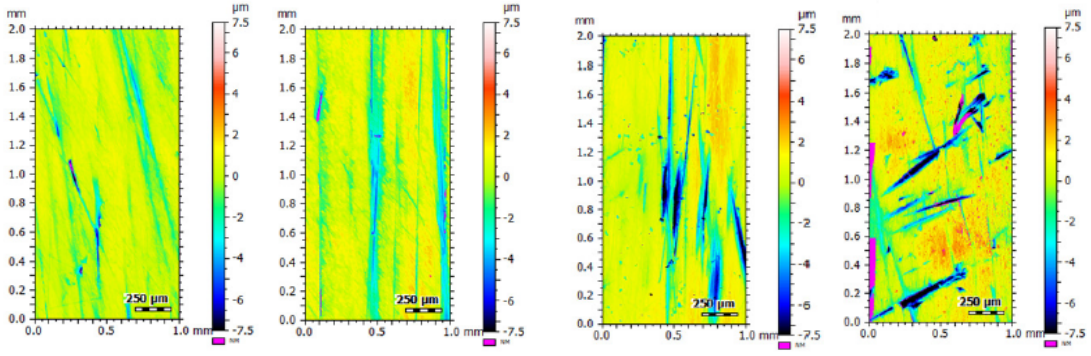

(a) Position 1B. *Fltr: Reference and after 50 draws.* (b) Position 3B. *Fltr: Reference and after 50 draws.*

Figure D.4: Topography evolution of the punch radius [63].

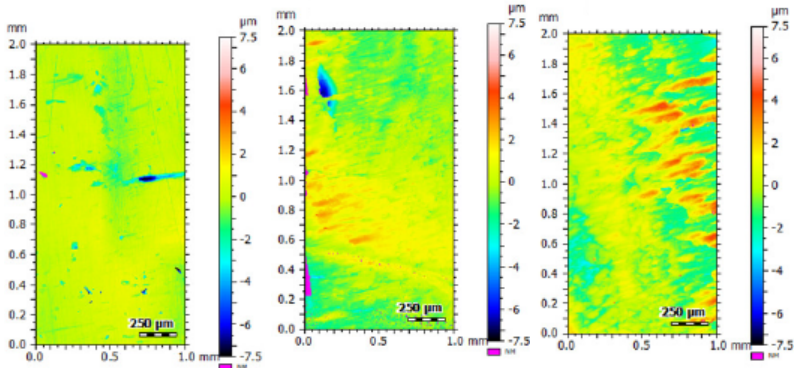

(a) Position 3. *Fltr: Reference, after 24 draws and after 50 draws.*

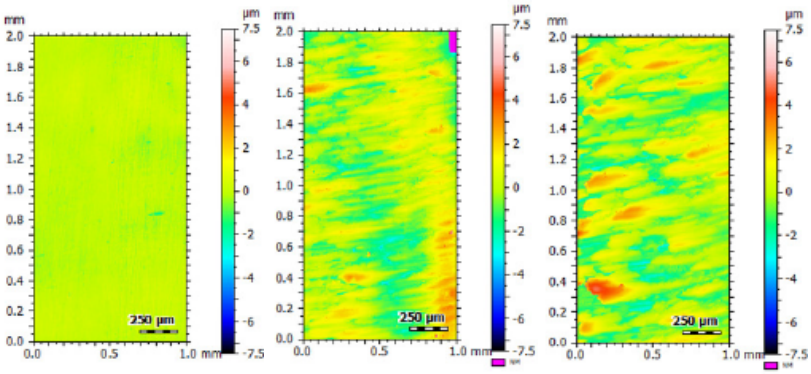

(b) Position 4. *Fltr: Reference, after 24 draws and after 50 draws.*

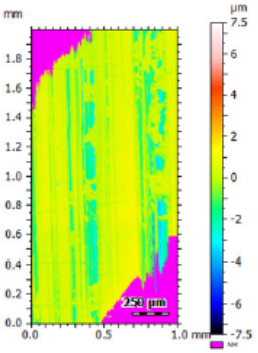

(c) Position 6. *After 50 draws.*

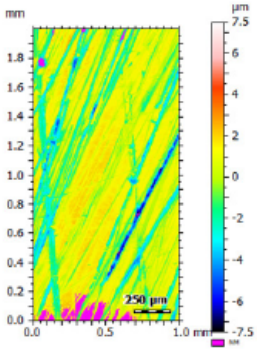

(d) Position 7. *After 50 draws.*

Figure D.5: Topography evolution of the die radius [63].

D.3 Adhered volume decreased tool roughness

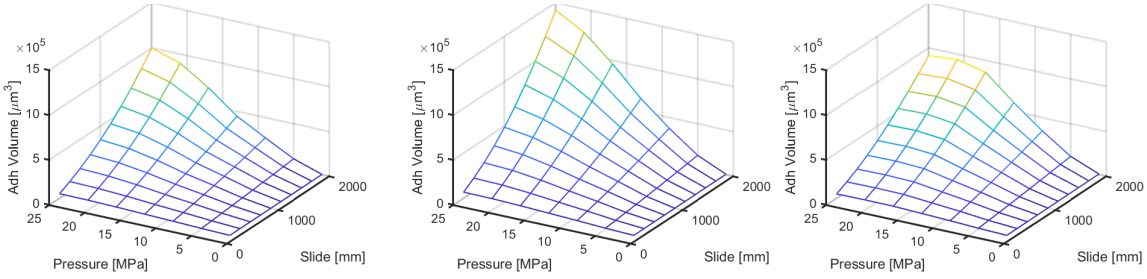

(a) 500°C . (b) 600°C . (c) 700°C .

Figure D.6: Adhered volume using CFI for 0 strain with the calibrated value for m applied to a tool roughness of Sa = 0.2 μm.

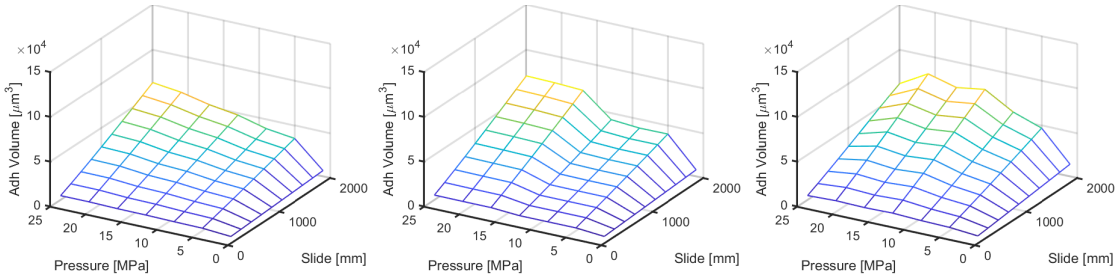

(a) 500°C . (b) 600°C . (c) 700°C .

Figure D.7: Adhered volume using WFI for 0 strain with the calibrated value for m applied to a tool roughness of Sa = 0.2 μm.